Western University
Scholarship@Western

Digitized Theses | Digitized Special Collections

1990

Hall Effect Of Amorphous Silicon Fabricated By A Low-pressure Chemical Vapour Deposition Method

Ning Du

Follow this and additional works at: https://ir.lib.uwo.ca/digitizedtheses

Recommended Citation
Du, Ning, "Hall Effect Of Amorphous Silicon Fabricated By A Low-pressure Chemical Vapour Deposition Method" (1990). *Digitized Theses*. 2009.
https://ir.lib.uwo.ca/digitizedtheses/2009

This Dissertation is brought to you for free and open access by the Digitized Special Collections at Scholarship@Western. It has been accepted for inclusion in Digitized Theses by an authorized administrator of Scholarship@Western. For more information, please contact tadam@uwo.ca, wlswadmin@uwo.ca.

HALL EFFECT OF AMORPHOUS SILICON FABRICATED BY A LOW PRESSURE CHEMICAL VAPOUR DEPOSITION METHOD

by

Ning Du

Department of Physics

Submitted in partial fulfilment
of the requirements for the degree of
Doctor of Philosophy

Faculty of Graduate Studies
The University of Western Ontario
London, Ontario, N6A 3K7, Canada

May 1990

© Ning Du 1990

National Library of Canada | Bibliothèque nationale du Canada

Canadian Theses Service | Service des thèses canadiennes

Ottawa, Canada
K1A 0N4

The author has granted an irrevocable non-exclusive licence allowing the National Library of Canada to reproduce, loan, distribute or sell copies of his/her thesis by any means and in any form or format, making this thesis available to interested persons.

L'auteur a accordé une licence irrévocable et non exclusive permettant à la Bibliothèque nationale du Canada de reproduire, prêter, distribuer ou vendre des copies de sa thèse de quelque manière et sous quelque forme que ce soit pour mettre des exemplaires de cette thèse à la disposition des personnes intéressées.

The author retains ownership of the copyright in his/her thesis. Neither the thesis nor substantial extracts from it may be printed or otherwise reproduced without his/her permission.

L'auteur conserve la propriété du droit d'auteur qui protège sa thèse. Ni la thèse ni des extraits substantiels de celle-ci ne doivent être imprimés ou autrement reproduits sans son autorisation.

ISBN 0-315-59120-X

4.21 Illuminated I-V characteristics of n-a,μc:Si/p-c:Si solar cell devices fabricated from Si films deposited at various gas ratios 90

4.22 Zones of different phosphorus doped LPCVD-Si material: amorphous (AMOR.), and microcrystalline (μc) 92

4.23 Zones of different boron doped LPCVD-Si material: amorphous (AMOR.), amorphous alloy (ALLOY) and microcrystalline (μc) 93

5.1 Hall effect measurement system 99

5.2 Sample holder for Hall measurement 100

5.3 Hall sample pattern diagram 103

5.4(a) The mask for the preparation of Hall samples 105

5.4(b) The mask for the electrodes on Hall samples 105

5.5 A typical Hall signal from measurements 108

5.6 Hall voltage vs. magnetic field for μc-Si samples .. 110

5.7 Hall voltage vs. magnetic field for a-Si samples ... 111

5.8 Hall mobility of P doped a-Si CP-119 (Normal Hall sign, R=1×10^{-3}, T_s=560 °C) and CP-145 (abnormal Hall sign, R=4×10^{-3}, T_s=540 °C) 113

5.9 Hall mobility of B doped a-Si CB-76 (Normal Hall sign, R=1×10^{-3}, T_s=500 °C) 114

5.10 Raman scattering of a-Si CP-119, CP-145 and μc-Si and c-Si 117

5.11 X-ray diffraction of CP-119 118

5.12 Seebeck coefficient of a-Si (CP-119, CP-145) and μc-Si (CP-118) 120

5.13 σ vs. 1/T of normal sample CP-119 and abnormal sample CP-145 121

5.14 The area where normal Hall samples are found (P doped) 125

5.15 The area where normal Hall samples are found (B doped) 126

5.16 Carrier concentration n vs. gas ratio R for P doped μc-Si at T_s = 600 °C 128

5.17 P concentration in film (S), carrier concentration (n) and doping efficiency (n/S) vs. gas ratio R for μc-Si samples at T_s = 600 °C 130

5.18 A band diagram for the electrical compensation model 132

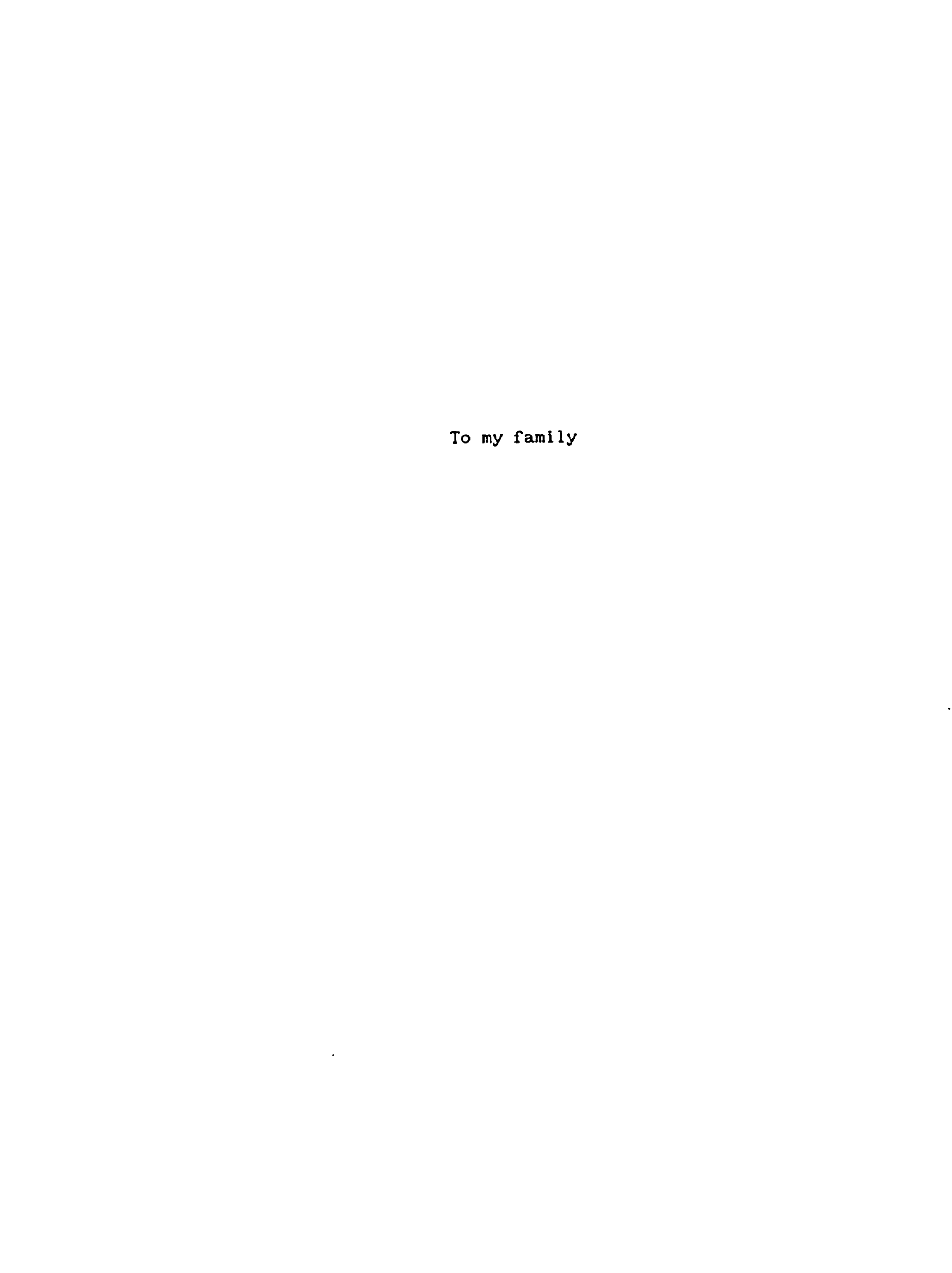

To my family

ACKNOWLEDGEMENTS

I would like to take this opportunity to thank Professors B.Y. Tong, S.K. Wong, P.K. John and Mr. Y.T. Zhu for their help and guidance during my Ph.D. program and the writing of this thesis. I would also like to address my thanks to Professor G.H. Chen of Lanzhou University of P.R.China who was responsible for leading me into this research area; my advisory committee members Professor Z. Kucerovsky, M.R. Singh and my colleague X.W. Wu for their helpful discussions; the Department of Physics at U.W.O. and the amorphous research group at U.W.O. for the financial support during my entire graduate program.

TABLE OF CONTENTS

	page
CERTIFICATE OF EXAMINATION	ii
ABSTRACT	iii
ACKNOWLEDGEMENT	v
TABLE OF CONTENTS	vi
LIST OF PHOTOGRAPHIC PLATES	viii
LIST OF TABLES	ix
LIST OF FIGURES	x
CHAPTER 1 — INTRODUCTION	1
CHAPTER 2 — THEORIES	6
2.1 Classical Model of Electron Transport	7
2.2 Band Models	11
2.3 Transport Mechanisms in a-Si	15
2.4 Small Polarons	21
CHAPTER 3 — SAMPLE FABRICATION AND DOPANT CONCENTRATION	29
3.1 Sample Fabrication	29
3.2 Dopant Concentration Study by SIMS	31

CHAPTER 4 — STRUCTURE CHARACTERIZATION 48

4.1 Direct Structural Analysis 49

4.2 Material Structure and Transport Properties 55

4.3 Material Structure and p-n Heterojunction Performance 67

4.4 Conclusions 91

CHAPTER 5 — HALL EFFECT 94

5.1 Experimental Considerations 95

5.2 Experimental Setups 97

5.3 Results and Discussion 112

CHAPTER 6 — CONCLUSIONS 144

REFERENCES 146

VITA 151

LIST OF PHOTOGRAPHIC PLATES

Plate	Description	Page
1	Photo of an actual Hall sample	104
2	Transmission electron microscopy (TEM) of CP-119	119

LIST OF TABLES

Table	Description	Page
4.1	Fabrication details of a-Si and μc-Si films used for diode I-V measurements	71
4.2	Diode factor for diode CP 116	80
5.1	Deposition parameters of CP145, CP119 and CP118	115
5.2	Solid phase concentration S and carrier concentration *n* of μc-Si at T_s = 600 °C	131

LIST OF FIGURES

Figure	Description	Page
2.1	The Hall effect	8
2.2	(a) CFO model; (b) Davis and Mott model; (c) Mott model; (d) Marshall and Owen model	13
2.3	Illustration of the effect of temperature on the mode of conduction: $T_1 > T_2 > T_3$	19
2.4	Temperature dependence of conductivity expected from the model of Fig. 2.3	19
2.5	Localized small polaron and overlap integral J	23
2.6(a)	Two sites electron transfer with the presence of magnetic field H	25
2.6(b)	Three sites electron transfer with the presence of magnetic field H 25	
3.1	Low pressure chemical vapour deposition system	30
3.2	The ^{11}B profile by SIMS of a typical boron doped film	35
3.3(a)	The ratio of solid phase concentration and gas phase concentration S/R vs. gas phase concentration R for boron doped samples	36
3.3(b)	The ratio of solid phase concentration and gas phase concentration S/R vs. gas phase concentration R for phosphorus doped samples	37
3.4	Boron concentration in film as function of gas ratio R and substrate temperature T_s	40
3.5	Zones of different boron doped LPCVD-Si material:amorphous (AMOR.), amorphous alloy (ALLOY) and microcrystalline (μc)	41
3.6	Dark conductivity of microcrystalline films vs. gas ratio	42
3.7	Photo-conductivity of microcrystalline films vs. gas ratio	43
3.8	Dark-conductivity of microcrystalline films vs. solid	

phase concentration 45
3.9 Photo-conductivity of microcrystalline films vs. solid phase concentration 46

4.1 X-ray diffraction of a-Si and μc-Si 50
4.2 X-ray results of P doped samples as function of gas ratio R and substrate temperature T_s 51
4.3 X-ray results of B doped samples as function of gas ratio R and substrate temperature T_s 52
4.4 Raman scattering results of a-, μc- and c-Si 54
4.5 Transmission electron microscopy (TEM) of a- and μc-Si 56
4.6 Conductivity σ vs. substrate temperature T_s for P doped samples 58
4.7 conductivity σ vs. gas ratio R for P doped samples 60
4.8 conductivity σ vs. gas ratio R for B doped samples 61
4.9 σ vs. 1/T for heavily P doped samples 64
4.10 σ vs. 1/T for B doped samples 65
4.11 Seebeck coefficient S vs. 1/T for typical a- and μc- Si 66
4.12 Forward dark I-V characteristics of n-a,μc:Si/p-c:Si diodes at room temperature 72
4.13 Forward dark I-V characteristics of diode CP 102 measured at different temperatures 74
4.14 Forward dark I-V characteristics of diode CP 116 at different temperatures 75
4.15 Variation of J_{01} as a function of measurement temperature for diode CP 102 76
4.16 Simulated I-V curves using eqn (4) 79
4.17 Variation of J_{02} as a function of 1/kT for diode CP-116 82
4.18 Temperature dependence of conductivity of phosphorus doped amorphous silicon films 84
4.19 Schematic diagram showing current transport mechanisms in n-a:Si/p-c:Si heterojunction 86
4.20 Illuminated I-V characteristics of n-a,μc:Si/p-c:Si solar cell devices fabricated from Si films deposited at various substrate temperatures 89

4.21 Illuminated I-V characteristics of n-a,μc:Si/p-c:Si solar cell devices fabricated from Si films deposited at various gas ratios 90
4.22 Zones of different phosphorus doped LPCVD-Si material: amorphous (AMOR.), and microcrystalline (μc) 92
4.23 Zones of different boron doped LPCVD-Si material: amorphous (AMOR.), amorphous alloy (ALLOY) and microcrystalline (μc) 93

5.1 Hall effect measurement system 99
5.2 Sample holder for Hall measurement 100
5.3 Hall sample pattern diagram 103
5.4(a) The mask for the preparation of Hall samples 105
5.4(b) The mask for the electrodes on Hall samples 105
5.5 A typical Hall signal from measurements 108
5.6 Hall voltage vs. magnetic field for μc-Si samples .. 110
5.7 Hall voltage vs. magnetic field for a-Si samples ... 111
5.8 Hall mobility of P doped a-Si CP-119 (Normal Hall sign, $R=1x10^{-3}$, T_s=560 °C) and CP-145 (abnormal Hall sign, $R=4x10^{-3}$, T_s=540 °C) 113
5.9 Hall mobility of B doped a-Si CB-76 (Normal Hall sign, $R=1x10^{-3}$, T_s=500 °C) 114
5.10 Raman scattering of a-Si CP-119, CP-145 and μc-Si and c-Si 117
5.11 X-ray diffraction of CP-119 118
5.12 Seebeck coefficient of a-Si (CP-119, CP-145) and μc-Si (CP-118) 120
5.13 σ vs. 1/T of normal sample CP-119 and abnormal sample CP-145 121
5.14 The area where normal Hall samples are found (P doped) 125
5.15 The area where normal Hall samples are found (B doped) 126
5.16 Carrier concentration *n* vs. gas ratio R for P doped μc-Si at T_s = 600 °C 128
5.17 P concentration in film (S), carrier concentration (*n*) and doping efficiency (*n*/S) vs. gas ratio R for μc-Si samples at T_s = 600 °C 130
5.18 A band diagram for the electrical compensation model 132

5.19 Carrier concentration n vs. solid phase P concentration S of μc-Si samples fabricated at T_s = 600 °C 134

5.20 Electron spin resonance (ESR) vs. R of samples at T_s = 600 °C 135

5.21 Conductivity σ vs. gas ratio R before and after hydrogenation for μc-Si at T_s = 600 °C 140

5.22 Hall mobility μ_H vs. gas ratio R before and after hydrogenation for μc-Si at T_s = 600 °C 141

5.23 Carrier concentration n vs. gas ratio R before and after hydrogenation for μc-Si at T_s = 600 °C 143

The author of this thesis has granted The University of Western Ontario a non-exclusive license to reproduce and distribute copies of this thesis to users of Western Libraries. Copyright remains with the author.

Electronic theses and dissertations available in The University of Western Ontario's institutional repository (Scholarship@Western) are solely for the purpose of private study and research. They may not be copied or reproduced, except as permitted by copyright laws, without written authority of the copyright owner. Any commercial use or publication is strictly prohibited.

The original copyright license attesting to these terms and signed by the author of this thesis may be found in the original print version of the thesis, held by Western Libraries.

The thesis approval page signed by the examining committee may also be found in the original print version of the thesis held in Western Libraries.

Please contact Western Libraries for further information:
E-mail: libadmin@uwo.ca
Telephone: (519) 661-2111 Ext. 84796
Web site: http://www.lib.uwo.ca/

Chapter 1 Introduction

In the past two decades, we have witnessed a rapid progress in the study of amorphous semiconductors (mainly amorphous silicon or a-Si). It still is one of the most active research areas in condensed matter physics today. Similar to other endeavours, the research is divided into two major directions: i) fundamental research aiming to understand the amorphous system (the structure of the material, the electron transport process, the electrical, optical and other properties); ii) application research (material and device fabrication etc.). The tremendous research efforts currently going on in the world have been incited by the successful application of the material in many areas such as energy production and information processing etc.. For example, solar cells made of amorphous silicon have achieved 13% conversion efficiency (Ovshinsky, 1987). Other amorphous silicon devices commercially available are photoreceptor, photoconductor, image sensor, thin film panel display, anti-reflecting layer, thin film transistor, etc.. Clearly this is a research field in which applications and commercialization of the material and devices provide most of the motivation.

Contrary to the perfect order in crystalline materials, amorphous materials are disordered. Amorphous networks do not have long range order, but its short range order is largely preserved

or is similar to its crystalline counterpart with only minor variations. There are various ways to produce amorphous Si: for example, plasma glow discharge method (GD), sputtering, electron gun evaporation, chemical vapour deposition (CVD) and its variations such as homo-CVD, plasma enhanced CVD, laser enhanced CVD etc.. A number of good review books exist on the fabrication of amorphous materials: for example, "Electronic Processes in Non-Crystalline Materials" (by N.F. Mott and E.A. Davis, 1979) and "Physics of Amorphous Materials" (by S.R. Elliott, 1984). In our laboratory, a low pressure chemical vapour deposition (LPCVD) system is used for material fabrication. Detailed description of the system is in chapter 3.

Among the above mentioned material preparation methods, plasma glow discharge (GD) and chemical vapour deposition (CVD) are by far the most popular ones currently being used in research and industry, because they generally produce better materials in terms of transport properties as compared to other methods such as sputtering and evaporation. The common feature of GD and CVD is that they both use silane (SiH_4) and corresponding dopant gas phosphine (PH_3) or diborane (B_2H_6) gas mixture as "raw" materials. In the case of GD method, the gas mixture is introduced into a plasma environment produced by a radio frequency electrical field in which the gas mixture is dissociated and solid phase film deposited onto substrates. The structure (whether it is amorphous or microcrystalline film), composition, defect concentration and electrical properties of the film are determined by factors such as the substrate temperature T_s , radio frequency power, gas flow

rate and the substrate position in relation to the plasma region, etc. In general, the best GD a-Si is produced under relatively low substrate temperature (T_s from 200 °C to 250 °C) and hence contains as much as 5% - 20% hydrogen. The existence of H in a-Si was recognized as a key contributor to the improved network structure of the material because H can effectively terminate dangling bonds and microvoids. It has also been suggested (J.C. Phillips, 1979 and J.C. Knights, 1980) that H may reduce the "microstrains" in the amorphous network. In 1975, Spear et al. first successfully doped GD a-Si:H (W.E. Spear and P.G. LeComb, 1975) and subsequently a p-n junction was fabricated. This was considered a breakthrough in amorphous semiconductor research.

One of the serious disadvantage of GD a-Si is the so called Staebler-Wronski effect (D.L. Staebler and C.R. Wronski, 1977): the degradation of electrical properties of a-Si:H after intensive light illumination. This effect will certainly jeopardize the reliability and performance of application devices such as solar cells fabricated by GD a-Si:H. We recognized that high H concentration, particularly the formation of $Si-H_2$ bond are probably responsible for the instablity of a-Si:H (see also, S. Nakano, et al., 1987) and designed a two-step material fabrication process, i.e.: i) deposit Si film by low pressure chemical vapour deposition (LPCVD) or by electron gun evaporation; and ii) post-hydrogenate the film by ion gun. Similar attempts have been made to reduce H concentration by CVD process (M. Nishikuni, et al., 1989) and improve the electrical property of the film by post-hydrogenation (Magarino, Kaplan and Friederich, 1982). CVD

a-Si sample generally contains very little H (less than 1%, for instance) due to its high substrate temperatures (typically above 450 ^{o}C). Doped CVD a-Si has good electrical properties. The room temperature conductivity of the amorphous sample can be controlled from $1x10^{-8}$ to $1x10^{-1}(\Omega\text{-cm})^{-1}$ depending on the doping concentrations. The conductivity variation range for microcrystalline Si can be even larger. Photo-conductivity is good with a typical value of $1x10^{-6}$- $1x10^{-5}$ $(\Omega\text{-cm})^{-1}$ for amorphous samples under favorable conditions. No Staebler-Wronski effect has been observed in post-hydrogenated a-Si samples (Tong et al., 1981, Akhtar et al., 1982, Delahoy, 1983, Ellis et al., 1984, Thomas and Flachet, 1985, Wu et al., 1987, Tsou et al., 1987). At U.W.O., heterojunction solar cell has been fabricated by LPCVD (low pressure chemical vapour deposition) method and close to 10% conversion efficiency has been achieved (chapter 4). CVD a-Si is a relatively pure material and its properties may be of intrinsic interest to theoretical models of amorphous solid.

Amorphous Si finds application mostly in electronic transport devices such as solar cells, thin film transistors, etc. It is of fundamental importance to fully understand the electronic transport processes in the material. From experimental point of view, transport property study involves the measurements of conductivity σ, Hall mobility μ_H , Seebeck coefficient S and other related quantities. Because of the structure disorder in amorphous materials, the behavior of the transport properties are quantitatively different from their crystalline counterparts. A good example is the Hall coefficient of a-Si.

Early works of Hall Effect measurements on amorphous materials were concentrated on chalcogenide glasses (See review by M.Rollos, 1978 and Fritzsche, 1974). The measurements on amorphous Si:H thin films fabricated by Glow Discharge method have been made and reported by the Dundee group (P.G. LeComb, et al, 1977), the Marburg group (W. Beyer, et al, 1979 and H. Overhof, et al, 1981), and by Dresner (J. Dresner, 1980). One of the most interesting features of these measurements is the well known sign anomaly of the Hall coefficient, e.g., for a-Si thin films, the so called "double reversal " phenomenon: the sign of Hall coefficient of both phosphorus and boron doped films are opposite to that of their single crystal (c-Si) counterparts (or opposite to that of their thermoelectric power). So far, no systematic measurements on LPCVD a-Si thin films have been reported. At U.W.O., we started an extensive research program to study the transport properties of LPCVD a-Si and observed, for the first time, normal Hall coefficient in some amorphous Si samples.

Chapter 2. Theories

The theory for crystalline solids (conventional solid state physics) has been well developed for many years and numerous standard textbooks are available for easy reference (for example, Kittel, 1968). Successful application of those theories to semiconductor materials, particularly silicon, has been a major contributor to the rapid development and growth of the semiconductor industry that significantly changed the world we live in today. Theories for amorphous semiconductors can be considered extensions of solid state theory because many fundamental concepts such as forbidden gap, conduction band, valence band, Fermi level, doping effect, etc. are still valid and frequently used. On the other hand, the lack of long range order in amorphous materials does impose severe limitations on the use of analytical mathematics in the theoretical work. In fact, one of the characteristics of the amorphous material study is that most of the scientific insight must be achieved without the help of mathematical amenities which accompany periodicity in the crystalline solid state. While some old approaches remain useful for amorphous solids (chemical bonding viewpoint, for instance), this challenge has been met mainly by new approaches such as localization and percolation theories. In this chapter, some related classical transport theory will be briefly reviewed. This is followed by a description of conduction mechanisms in amorphous

materials. Large portions of this chapter are devoted to small polaron theory because this is the only existing theory to tackle the Hall effect of amorphous material in a unique and comprehensive manner. And finally, some typical band models of amorphous materials are presented.

2.1 Classical Model of Electron Transport

2.1.1 Hall Effect and Conductivity

In Fig.2.1, if a current bearing (j_x) sample is introduced into a magnetic field (B_z), an electrical field E_y perpendicular to j_x and B_z can then be detected. Experimentally, it can be established that $E_y = R_H j_x B_z$ where R_H is the Hall coefficient. This phenomenon was first observed by Edwin Hall in 1879 and subsequently named after him. The simplest explanation of the Hall effect is the following: consider charge carriers moving in a solid as free particles with uniform velocity v_x ; the Lorentz force experienced by the particles is $v_x B_z e$. Under equilibrium condition, the Lorentz force should cancel the force due to Hall field E_y :

$$e v_x B_z = e E_y \qquad (2.1)$$

The current density j_x can be expressed as:

$$j_x = n v_x e \qquad (2.2)$$

where n is the carrier density. Combining Eq. (2.1), (2.2) and $E_y = R_H j_x B_z$, one can easily get:

$$R_H = \frac{1}{n e} \qquad (2.3)$$

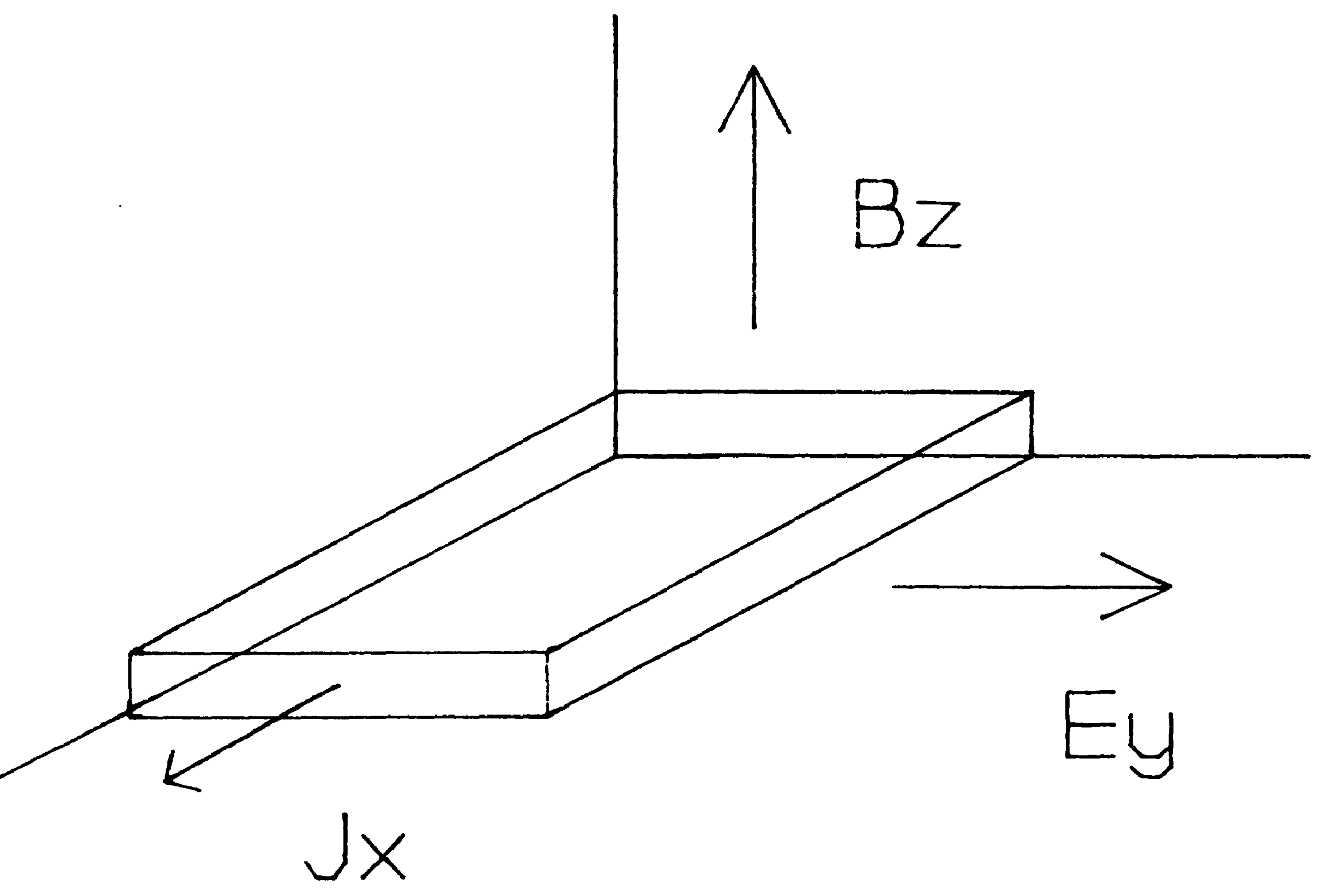

Fig. 2.1. The Hall effect

where e is the charge of each carrier. For electron, the charge is negative and for hole, positive. Hall coefficient R_H is thus closely related to the carrier type of the material. For n type material (electron conduction), R_H is negative and for p type material (hole conduction) R_H is positive. According to Eq. (2.3), the carrier concentration n can also be obtained through the measurement of Hall coefficient. It is amazing that this simple experiment can yield so much important information about the electrical property of the material.

The Hall mobility μ_H is defined as:

$$\mu_H = \sigma R_H \tag{2.4}$$

where σ is the conductivity of the material and can be expressed, under the free particle model, as:

$$\sigma = \mu_D e n \tag{2.5}$$

μ_D is the drift mobility of the carrier. Eq. (2.3), (2.4) and (2.5) give the conclusion that drift mobility μ_D is the same as Hall mobility μ_H . This is of course based upon the assumption that charge particles in solids act as free particles - a very simplified and yet effective model for the description of electron transport in crystalline materials. A much more refined model used in standard semiconductor physics literature (see, for example, Smith, 1978) that introduces different scattering mechanisms, gives basically the same conclusions.

2.1.2 Thermoelectric Power

When a semiconductor sample is subjected to a temperature gradient ΔT, a voltage drop proportional to ΔT will be generated

across the sample:

$$\Delta V = S\,\Delta T \tag{2.6}$$

where S is called the Seebeck coefficient.

For a non-degenerate n-type crystalline semiconductor, the thermoelectric power can be expressed as (Smith, 1978):

$$S = -\frac{k}{|e|}\left(\frac{E_c - E_F}{k\,T} + A_c\right) \tag{2.7}$$

where E_c is the energy level of the conduction band and E_F is the Fermi energy. A_c is a constant. In the case of extended state conduction, $A_c = 1$. The sign of the Seebeck coefficient is also carrier type dependent. In the case of crystalline materials, it is positive for p type and negative for n type. The carrier type determined by Hall effect measurement and thermoelectric power measurement are in complete agreement for crystalline samples. As we mentioned in chapter 1, this agreement no longer exists in amorphous materials where anomalous Hall coefficient has been observed.

In degenerate crystalline semiconductors, the Seebeck coefficient can be written as :

$$S=(\pi^2\, k^2\, T/3e)[d\ln\sigma(E)/dE] \tag{2.8}$$

which is proportional to the temperature, and identical to the equation used for metallic conduction. $\sigma(E)$ is the contribution to conductivity at energy level E.

2.2 Band Models

For single crystal semiconductors it is known that the energy distributions of the density of electronic states N(E) are abruptly terminated at the valence band maximum and the conduction band minimum. The sharp edges in the density of states produce a well-defined forbidden energy gap. Within the forbidden energy gap no electronic states are allowed while in the conduction or valence band, the electronic states are extended, which means the wave functions occupy the entire body of the material. These are the direct consequences of the perfect short-range and long-range order of the crystal. In an amorphous solid, however, the long-range order no longer exists whereas the short-range order, i.e. the interatomic distance and the bond angle, is only slightly changed. The loss of long-range order and short-range order will certainly influence the electronic structure of the material, but the concepts of forbidden gap, conduction band, valence band as well as density of states, originally from the study of single crystalline materials, are still applicable to noncrystalline semiconductor materials.

Anderson in his paper " Absence of Diffusion in Certain Random Lattices " (1958) first introduced the concept of localization. Mott (1970) further developed Anderson's work. According to Mott and Anderson, the spatial fluctuations in the potential caused by the structure disorder in amorphous materials may lead to the formation of localized states, which do not occupy

all different energy states, but form a tail above and below the normal bands. Mott assumed that there would be a sharp boundary between the extended and localized states, the so called mobility edge. In extended states the electron wavefunction occupies the entire volume, while in localized states, the wave function placed in a region does not diffuse at zero temperature to other regions. This diffusion can occur , however, with the assistance of phonons.

The properties of different amorphous materials are quite different. Based on Mott and Anderson's work, several band models were proposed. These models are similar to each other in a sense that they all use the concept of localized states in the band tails. However, as to the detailed structure of the tailing, these models do show some differences. Fig. 2.2 illustrates the main features of these models.

2.2.1 The C-F-O Model

The CFO model, shown in Fig. 2.2(a) and proposed by Cohen, Fritzsche and Ovshinsky (1969), assumes that the tail states occupy the whole band gap in a structureless distribution. This model was proposed basically for the multicomponent chalcogenide glasses used in switching devices. For these chalcogenide alloys the disorder of the structure is so great that the tails of the conduction and valence bands may overlap, leading to an appreciable density of states in the middle of the gap. Due to this overlapping effect, some of the states in the valence band, ordinarily filled, will have higher energies than those in the

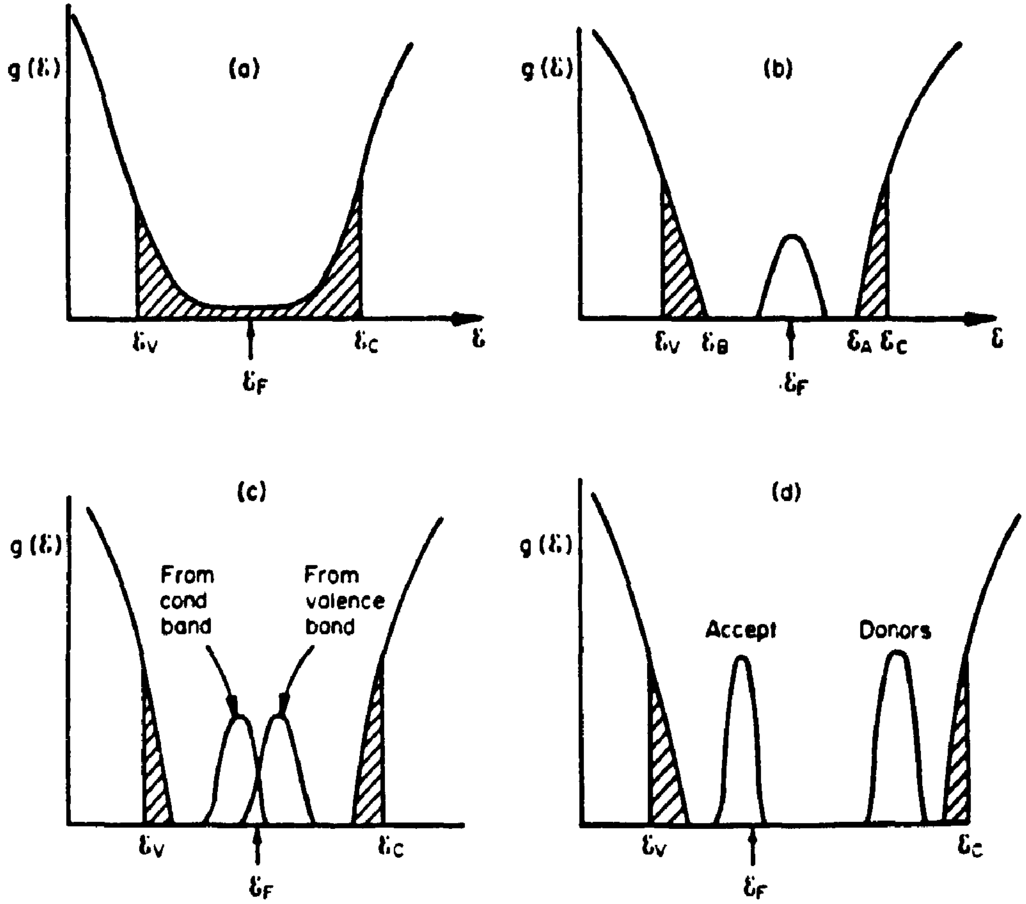

Fig. 2.2. (a) CFO model; (b) Davis and Mott model; (c) Mott model; (d) Marshall and Owen model.

conduction band which usually are unfilled. A redistribution of the electrons must then take place, forming filled states, which are negatively charged, in the conduction band tail, and empty states, which are positively charged , in the valence band tail. This model, therefore, ensures self-compensation, and pins the Fermi level close to the middle of the gap.

2.2.2 The Davis-Mott model

This model was proposed by Davis and Mott in 1970. According to their postulation, the tails of localized states do not occupy the whole forbidden gap; instead, the energy distribution of these states could be very narrow and extends a few tenths of an electron volt into the forbidden gap. There also exists a band of compensated levels near the middle of the gap, due to the defects in the random network, e.g., dangling bonds, vacancies, etc.. Fig. 2.2(b) shows the main features of this model: E_c and E_v represent the energies which separate the localized and extended states.

2.2.3 The Mott Model

The Mott Model is actually a modified Davis-Mott Model(some people call it " modified Davis-Mott Model "). It was proposed by Mott in 1972. The main feature of this model is that the band near the middle of the band gap may be split into a donor and an accepter band, which will also pin the Fermi level. It is shown in Fig. 2.2(c).

2.2.4 The Marshall-Owen Model

This model was suggested by Marshall and Owen in 1971. It was

proposed to explain the high field drift mobility in As_2Se_3. In Fig. 2.2(d), the energies E_v and E_c have the same meaning as that in the Davis-Mott model. The Fermi level is determined by a band of localized acceptor states which lies below and a band of localized donor states which lie above the gap center. The concentrations of donors and acceptors adjust themselves by self compensation to be nearly equal so that the Fermi level remains near the gap center.

2.3 Transport Mech sms in a - Si

2.3.1 Conductivity of a-Si

Electrical conductivity of amorphous silicon involves contributions from several conduction paths:

1) electron transport in extended states above mobility edge E_c (for electrons) or below E_v (for holes);

2) phonon - assisted hopping through localized states within the mobility gap;

3) at very low temperature the variable-range-hopping process will dominate the conducting process.

The long range disorder in amorphous Si causes strong scattering effects, resulting in a short electron mean free path L_e in extended states. L_e usually is defined as the distance in which the electron eigenfunction loses phase coherence. Near E_c , L_e is of the order of the average atomic spacing (Nagels, 1979). Thus, conduction in extended states resembles Brownian motion with a relatively poor mobility μ_{ext}. Mott and Davis (1979)

derived an expression for μ_{ext} as follows:

$$\mu_{ext} = 1/6\ (e/kT)\ h/m \qquad (2.9)$$

m in Eq. (2.9) is the mass of free electron and h, Planck's constant. Using expression (2.9), one can calculate the mobility value in extended states. At T=300 K (room temperature), it is estimated to be ≈ 6 $cm^2/V\ s$. This value is much smaller than that in c-Si and corresponds to a mean free path comparable to or less than the interatomic distance. Cohen suggested that conduction in this case would be described more properly as a diffusive or Brownian-type motion (Mott, 1970).

One expects the contribution to conductivity by electrons above E_C to have the form (see Fig. 2.2 for the definition of E_C , E_V , E_A , E_B and E_F):

$$\sigma = \sigma_o \exp[-(E_C - E_F)/kT] \qquad (2.10)$$

From optical absorption measurements on amorphous semiconductors it is known that the band gap decreases with the increase of temperature. The energy difference therefore will show a similar behavior. If the temperature range is not so wide, one can assume a linear relation as follows:

$$E_C - E_F = (E_C - E_F)_o - \gamma T \qquad (2.11)$$

Combining Eq. (2.10) and (2.11) we have:

$$\sigma = \sigma_o \exp[-(E_C - E_F)_o /kT] \qquad (2.12)$$

where

$$\sigma_o = e\,\mu_{ext}\,N(E_C)\,k\,T\,\exp(\gamma/k) \qquad (2.13)$$

from Eq. (2.9), μ_{ext} is proportional to 1/T, so σ_o is temperature independent and, according to Mott (1970), lies between 10 and 10^3 for most amorphous semiconductors.

Below E_C, carrier transport is phonon-assisted hopping between localized states. Carriers will be first excited into localized states at the band edges and then hop at energies close to E_A and E_B ; the conduction process can be written (Mott, 1979):

$$\sigma = \sigma_1 \exp[-(E_A - E_F + w_1)/kT] \qquad (2.14)$$

where w_1 is the activation energy for hopping and σ_1 should be several orders of magnitude less than σ_o.

At low temperature, the conductivity is determined by the distribution of localized states within the mobility gap. As the temperature is lowered, the maximum contribution to phonon-assisted hopping will shift towards the Fermi energy E_F, resulting in a decreased activation energy. At sufficiently low temperatures, the hopping conduction near Fermi level will dominate the transport process. Conduction near the Fermi level involves a hopping energy w_2 and is of the form:

$$\sigma = \sigma_2 \exp(-w_2/kT) \qquad (2.15)$$

where $\sigma_2 < \sigma_1$.

At an even lower temperature range, the energy of phonons is not sufficient to assist hopping between nearest neighbors. Carriers are forced to seek only energetically similar sites, resulting in a dominance of the variable-range-hopping process. The temperature dependence of conduction by variable-range-hopping has been derived by Mott (1979) and has the form:

$$\sigma = \sigma_3 \exp(-B/T^{1/4}) \qquad (2.16)$$

We have discussed so far the conduction process of different conduction mechanisms separately. The total conductivity for all processes can be obtained as an integral over all available energy states above E_F :

$$\sigma = \int \sigma(E)\, dE \qquad (2.17).$$

In Eq. (2.17) $\sigma(E)=e\ N(E)\mu(E)kT\ df(E)/dE$ and $f(E)$ is the Fermi-Dirac function. Fig. 2.3 shows N(E), $\mu(E)$, $f(E)$ and $df(E)/dE$ for states above E_F and the change of $\sigma(E)$ with temperature. This is also illustrated in Fig. 2.4.

2.3.2 Hall Effect of a-Si

The classical model of Hall effect (§ 2.1) is successful for crystalline semiconductor materials. In amorphous materials, due to the hopping nature of the electron transport process, things become much more complicated. We know from standard transport theory the following equations:

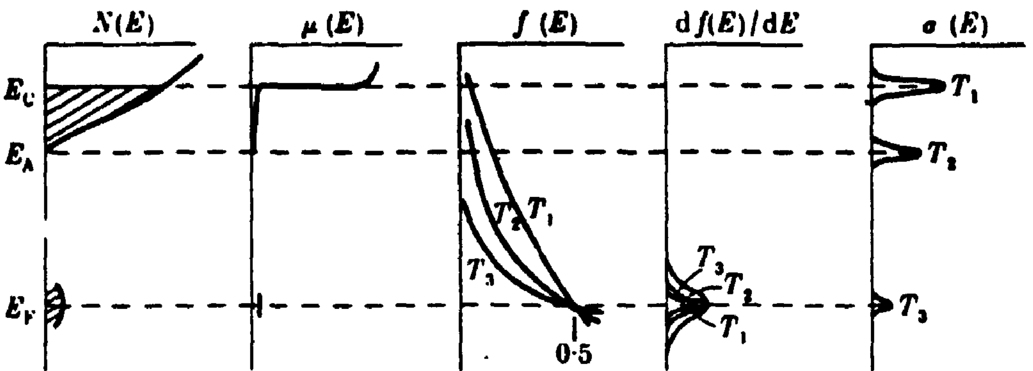

Fig. 2.3. Illustration of the effect of temperature on the mode of conduction: $T_1 > T_2 > T_3$.

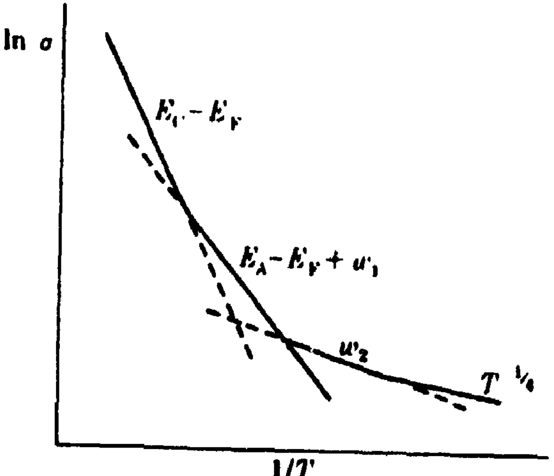

Fig. 2.4. Temperature dependence of conductivity expected from the model of Fig. 2.3.

$$\bar{L} = (D\ \tau)^{1/2} \tag{2.18}$$

$$D = \mu\ kT/e \tag{2.19}$$

$$\mu = (e/kT)\ \langle v^2\ \tau \rangle \tag{2.20}$$

v is the thermal-velocity of the carriers, D is the diffusion constant and τ the mean time between scattering events. Combining these equations we can relate the mean free path to the mobility:

$$\bar{L}\ (\mathrm{cm}) = 3.8\mathrm{x}10^{-9}\ (m^{*}/m)\ \mu\ (\mathrm{cm}^{2}/\ \mathrm{V\ s}) \tag{2.21}$$

where m is the free electron mass and m^{*} the carrier effective mass. From Eq. (2.21) one sees that when $\mu < 5$ cm^2/V s, the mean free path of the carriers is smaller than 2 Angstrom (taking m^{*} = m) which is comparable to or shorter than the mean distance between atomic sites in the semiconductor. When $\bar{L}$ is less than the interatomic distance, one can no longer use classic methods to treat this problem anymore, i.e. one cannot analyze the Hall effect by calculating the Lorentz force as though the electrons are delocalized. Instead, one must calculate the jumping probability between localized sites in the material using a quantum mechanical approach. One example of such a calculation will be presented in next section (§ 2.4).

By using a random phase model, Friedman (1971) has found theoretically an expression for the Hall mobility in the extended states near the mobility edge. His result has the form:

$$\mu_{H} = 4\pi(e\ a^{2}/h)[a^{2}J\ N(E_{C}\ )]\alpha(\chi^{*}/\chi) \tag{2.22}$$

J is the overlap energy integral between neighboring sites (see § 2.4); a is the interatomic spacing; z is the coordination number and z^* that of the interacting sites (Friedman took $z^*=z=6$); α is a parameter of the order of 1/3.

From Eq. (2.22) an estimate of the magnitude of μ_H is made and the value found ≈ 0.1 $cm^2/V\ s$. Furthermore, the Hall mobility and the conduction mobility have the following relation:

$$\mu_H / \mu_C \approx kT/J \qquad (2.23).$$

J usually is of the order of 1 eV. Unlike crystalline material, the Hall mobility of amorphous material is considerably smaller than the conduction mobility.

In the next section, we will further discuss Hall effect of a-Si from small polaron point of view.

2.4 Small Polarons

The classical free particle model in § 2.1 is based on the assumption that the carriers have long mean free path, i.e. the mobility of the carriers in solids is high. This is a valid model for wide band, high mobility material such as c-Si. In low mobility materials the behavior of carriers is expected to be different. Some aspects of those materials can be described by small polaron theory.

The notion of a small polaron was introduced by Lev Davidovich Landau almost 60 years ago (L.D. Landau, 1933). This

concept was further developed by T. Holstein, L. Friedman and D. Emin (Holstein, 1959, Friedman and Holstein, 1963, Emin, 1971). In this section, only the concept, physical picture of the transport process of small polaron and some important results regarding Hall effect are presented.

An excess charge carrier in a solid will distort its surroundings due to the Coulomb interaction. If the mobility of the carrier is sufficiently low so that it can stay in one location for a relatively long period of time, the distortion will be more prominent. These distortions or atomic displacements are such as to lower the potential energy of the excess charge. If the potential well produced by the displacement pattern is sufficiently deep, the carrier may occupy a bound state. In this circumstance the excess charge cannot escape from its position in the solid without an alteration of the positions of the surrounding atoms. Since the potential well that binds the carrier arises from atomic displacements caused by the presence of the carrier, the carrier is said to be self-trapped.

The polaron is the entire unit comprising the self-trapped carrier and the atomic displacement pattern. It is called "small" polaron because the spatial extent of the wave function of the excess carrier is less than or comparable to the atomic spacing. The electron wave function becomes localized and can move only in response to appropriate motions of the surrounding atoms. A possible process is pictured in Fig. 2.5: two neighboring sites 1 and 2 with wave function ψ_1 and ψ_2. From quantum mechanics, we

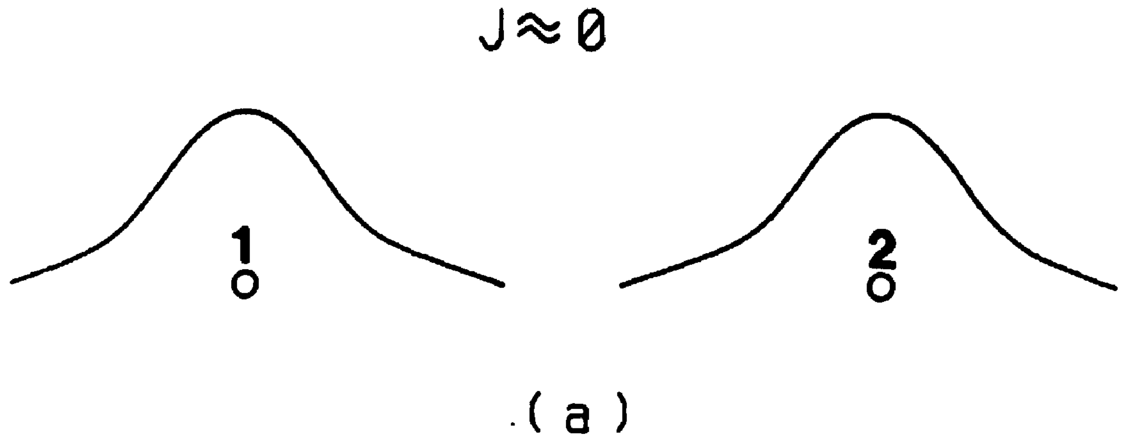

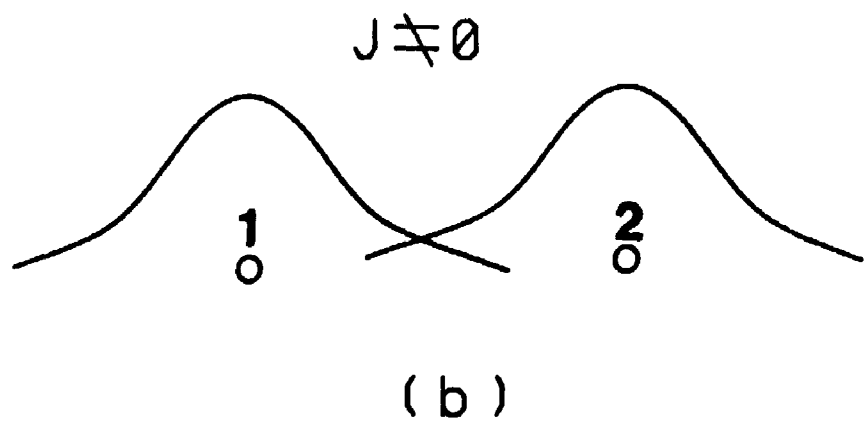

Fig. 2.5. Localized small polaron and overlap integral J.

know that the transition probability of an electron from 1 to 2 should be related to the quantity $J = \int \psi_1^* H \psi_2 d\vec{r}_1 d\vec{r}_2$ where H is the Hamiltonian of the electron-lattice interaction. If the two sites are so far away such that ψ_1 and ψ_2 almost do not overlap ($J \approx 0$), the transition probability from 1 to 2 will be almost zero. J is called the overlap integral that we have already mentioned earlier (see Eq. (2.22)). A nonzero J is important in hopping transport.

The jumping probability of the lowest order from site 1 to site 2 with the presence of a magnetic field H (see Fig. 2.6(a)) has the form (Holstein, 1959, Friedman and Holstein, 1963, Emin, 1971):

$$\omega_2 = C J^2 \exp(-\mathcal{E}_2 / kT) \qquad (2.24)$$

where C is a constant and $\mathcal{E}_2$ is the energy difference between 1 and 2. One notices that $\omega_2 \propto J^2$ and even more importantly, ω_2 is independent of magnetic field H (if H is sufficiently weak), therefore makes no contribution to the Hall effect.

If we consider jumping probability of higher order, i.e., the electron hops from site 1 to site 3 through an intermediate site 2 (see Fig. 2.6(b)), a magnetic - field dependent jumping probability can be obtained as follows (Friedman and Holstein, 1963):

$$\omega_3^{(H)} = (2\pi)^3 \left(\frac{e\, \mathbf{H} \cdot \mathbf{A}_{321}}{h^2 c} \right) \frac{J^3}{3\sqrt{3}\, kT\, \mathcal{E}_3} \exp(-\mathcal{E}_3 / kT) \qquad (2.25)$$

where H is the magnetic field and $\mathbf{A}_{321}$ is the area enclosed by

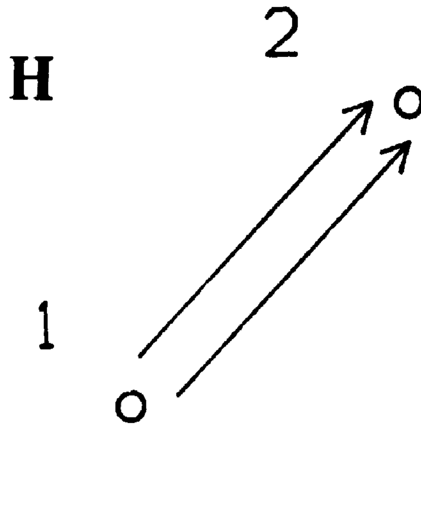

(a)

Fig. 2.5(a) Two sites electron transfer with the presence of magnetic field **H**.

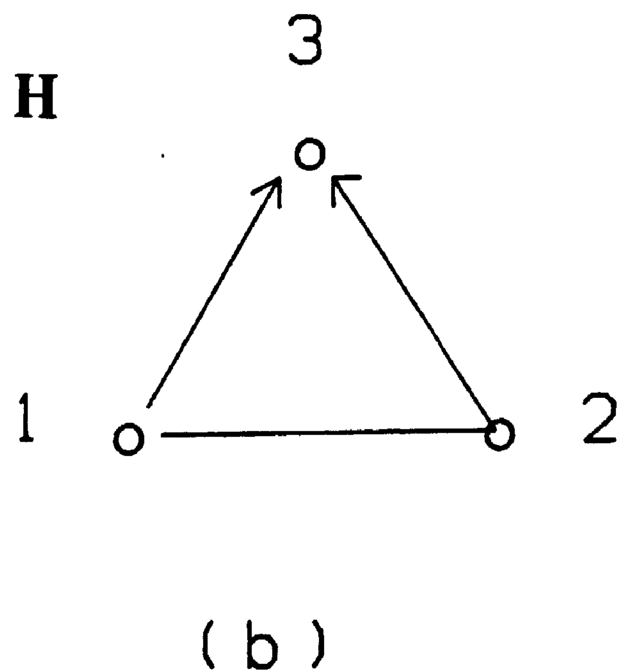

(b)

Fig. 2.5(b) three sites electron transfer with the presence of magnetic field **H**.

site 1-2-3 (Fig.2.6(b)). $\mathcal{E}_3$ is the energy of site 3 relative to site 1. This result can be viewed as a consequence of the interference effect of wave functions between route 1 $\rightarrow$ 3 and route 1 $\rightarrow$ 2 $\rightarrow$ 3. The magnetic field dependence factor in Eq. (2.25) comes from the phase difference of $\exp(i\gamma \mathbf{H}\cdot\mathbf{A}_{321})$ (γ is a constant) between route 1 $\rightarrow$ 3 and route 1 $\rightarrow$ 2 $\rightarrow$ 3.

Once the jumping probability from site 1 to site 2 is obtained, the average velocity of an electron in the solid can then be calculated from:

$$\vec{v} = \sum_i \vec{r}_i \, w_i^{(H)} \qquad (2.26)$$

$\vec{r}$ is the position of the ith atomic site relative to the original position of the electron and the summation in Eq. (2.26) is over all the nearest neighboring sites. From the velocity of the electron, the Hall mobility can be deduced. For a simple 2-dimensional hexagon configuration, Friedman and Holstein (1963) were able to obtain an expression of Hall mobility according to this small polaron model:

$$|\mu_H| = \pi \, e \, a^2 \left(\frac{\pi}{4kT\mathcal{E}_2} \right)^{1/2} \frac{J}{h} \exp\{-(\mathcal{E}_3-\mathcal{E}_2)/kT\} \qquad (2.27)$$

$\mathcal{E}_2$ and $\mathcal{E}_3$ are the energy of site 2 and 3 relative to site 1, a is the site distance. The behavior of Eq. (2.27) agrees quantitatively with the μ_H vs. 1/T data measured from various amorphous materials (Emin, 1979). Furthermore, according to this model, under certain atomic lattice configurations, sign anomaly of Hall coefficient may indeed occur. Emin (1977) concluded that

the sign of Hall coefficient follows the rule:

$$\mathrm{Sign}(R_H) = \mathrm{Sign}(\varepsilon^{n+1} \prod_{j=1}^{n} J^{i}_{j,j+1}) \qquad (2.28)$$

For "holes", $\varepsilon = +1$ and for electrons, $\varepsilon = -1$. i in Eq. (2.28) represents i^{th} band (for example, i can be conduction or valence band). n is the number of atomic sites in a complete ring (See Fig. 2.6(b): there are 3 sites in the ring). For rings with even-number sites, Eq. (2.28) predicts a normal Hall coefficient for both holes and electrons. For odd-number rings, Eq. (2.28) becomes:

$$\mathrm{Sign}(R_H) = \mathrm{Sign}(\prod_{j=1}^{n} J^{i}_{j,j+1}) \qquad (2.29)$$

The sign of R_H is then determined by the sign and number of overlap integral J:

$$J = \int \psi_1^{*} H \psi_2 \, d\vec{r}_1 d\vec{r}_2 \qquad (2.30)$$

If the conduction path is in conduction band - electron conduction, Eq. (2.30) gives a positive J for electron conduction because: i) ψ_1 and ψ_2 should be asymmetric wave functions for the anti-bonding configurations; ii) the small polaron energy H is also negative, the integration of Eq. (2.30) should then be positive. Following Eq. (2.29), the sign of the Hall coefficient is then positive - anomalous sign for electron conduction. For hole conduction in valence band, ψ_1 and ψ_2 are symmetric, Eq. (2.30) thus yields a J with negative sign. The Hall coefficient of hole conduction is negative according to Eq. (2.29): anomalous again for hole conduction.

The important conclusion from the discussions above is that the sign of Hall coefficient in amorphous material depends not only on the carrier type but also on the local lattice geometry of the material network. Even though the theory itself does not exclude the possibility of normal Hall coefficient from amorphous materials, in practice, it is surprising that so far all the Hall effect measurement of amorphous materials showed abnormal signs (see review by Rollos, 1978). In chapter 5, we will further discuss this matter and report the observation of normal Hall coefficient in our LPCVD a-Si samples.

Chapter 3 Sample Fabrication and Dopant Concentration*

3.1 Sample Fabrication

$B_X Si_{1-X}$ and $P_X Si_{1-X}$ (X is the percentage of boron or phosphorus atoms in solid phase films) thin film samples are fabricated by the LPCVD method (Low Pressure Chemical Vapor Deposition) which decomposes silane and diborane (or silane and phosphine) gas mixture thermally and deposits the film onto a substrate. Since the fabrication procedures of these two different materials are exactly the same, we only take the fabrication of $B_X Si_{1-X}$ film as an example here.

Fig.3.1 is the diagram of our LPCVD system. Two 1000 W light sources are employed as power sources to dissociate the reaction gas and raise the substrate temperature. During sample fabrication SiH_4 gas diluted by Ar (3 % silane and 97 % Ar, in some cases 10 % silane and 90 % Ar) and B_2H_6 , gas which is also diluted by Ar (1 % diborane and 99 % Ar, in some cases 0.03 % diborane and 99.97 % Ar), flow simultaneously into the reaction chamber, passing through a graphite reactor (the reactor is a graphite box with only two open ends in the direction of the gas flow so that the gas mixture can pass through it. the sample substrate is situated

---

* *This chapter has been published in J. Non-Cryst. Solids,* **110,** *179 (1989).*

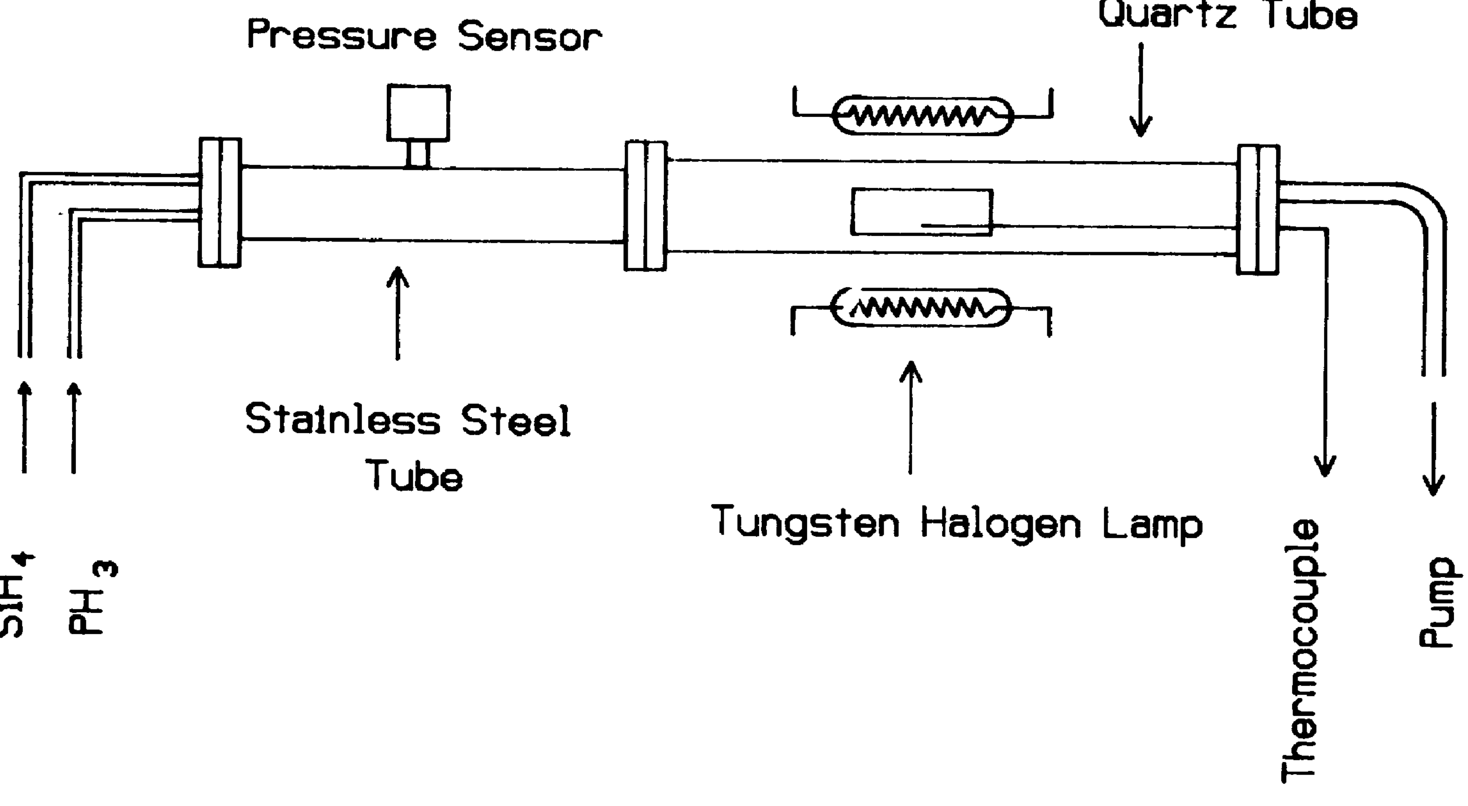

Fig. 3.1. Low pressure chemical vapour deposition system.

inside the graphite box) which is heated by the two light sources placed above and below the reactor. When the gases pass through the graphite reactor, they are dissociated and silicon films are deposited onto the substrates (usually we use Corning 7059 glass or c-Si wafer).

The parameters controlled in the fabrication process are the flow rates of SiH_4 and dibo· · e, the reaction chamber pressure, and substrate temperature T_s. The flow rate of the gas mixture (silane plus diborane) and the reaction chamber pressure are kept constant for all sample fabrications (total flow rate: 80±4 SCC/min.; reaction pressure:3.0±0.02 Torr). The parameters systematically changed are the flow rate ratio (R) of the two gases and the substrate temperature T_s . Co· rolling these two parameters, films with different properties over a very wide range can be obtained. In this chapter, the correlation between dopant concentration (phosphorus or boron concentration in the films) and fabrication parameters R and T_s will be discussed. In the next chapter, we will further discuss the influence of T_s and R on material structure (whether it is amorphous or microcrystalline) and how the transport properties are affected by R and T_s.

3.2 Dopant Concentration Study by SIMS

Doped silicon thin films are usually deposited from a gas mixture of silane and the corresponding hydrogen compounds of the dopant in the gaseous form: for example, diborane B_2H_6 and phosphine PH_3 . Thus in nearly all published articles, it is the gas mixture ratios that are specified no matter by what process

{Glow Discharge (GD), Homo-CVD (Chemical Vapour Deposition), or Laser-CVD and such } the films are deposited. The amount of dopant present in the solid phase film is estimated from this ratio. Through the work of Carlson (GD) (Carlson et al., 1982) and of Magarino (Magarino et al., 1982) (CVD), it has been realized that this estimation is lower than the true concentration by a factor that according to Carlson, is about 2.5, and Magarino, from 5 to 50. It is generally accepted that the concentration of dopants in the solid film is higher than that in the gas mixture, differing at most by one order of magnitude, and it is about the same for different dopants. For this reason, all studies on various properties of the film, for instance the position of Fermi level, the conductivity etc., are usually correlated to gas mixture ratios.

A little thought on the chemistry of decomposition of silane and the dopant gas, diborane or phosphine, would raise questions such as: would the decomposition in glow-discharge or microwave discharge be different from that in the pyrolysis of the gas mixtures, and would the concentration be insensitive to the dopant species? We have carried out a large scale SIMS (Secondary Ion Mass Spectrometry) study on the concentration of dopants, boron and phosphorus, in solid phase films produced by pyrolysis in a LPCVD (Low Pressure Chemical Vapour Deposition) system. Over 120 samples deposited at different substrate temperatures and different gas ratios R have been analyzed. The primary objective of this study was to investigate systematically the variations of solid phase dopant concentration in the LPCVD Si film as a

function of fabrication conditions since very little data are available on this subject. The predictions of solid phase concentration under different fabrication conditions require detailed knowledge of the chemical reaction process which is still not possible at the present time. Hopefully this study will provide some empirical relationship for LPCVD Si thin films. There is no reason, however, to believe that the B and P concentrations in the film have the same behavior over the fabrication conditions because the reaction species are not the same. SIMS results indicate that the ratio S/R (dopant concentration in the solid film (S) to that in the gas mixture (R)) for phosphorus and boron doped films are indeed substantially different. In general, we found that this ratio depends on the deposition temperature, gas mixture concentration, the dilution of carrier gases and other parameters. More interestingly it was realized that the physical properties of the films when presented in terms of the true concentrations in the solid film are significantly different and more meaningful from those presented against gas mixture ratios. During this investigation a Si-B alloy had also been identified and reported (K.P. Chik, N. Du et al, 1985).

Dopant concentration in the solid film was determined by SIMS (Cameca IMS 3f at Surface Science Western). The absolute amount of phosphorus or boron present in the film was obtained by comparing the measured mass-spectral signal with standards which are single crystal wafers implanted with a known dosage of dopant atoms. It was assumed that structural differences in amorphous, microcrystalline and single crystalline materials have no effect

in the concentration measurement. The "plough phenomenon" in SIMS provides no difficulty here since the profile is uniform throughout the film. The depth profile of dopant atoms in the films was measured by using O_2^+ ions for sputtering. Si^{30} was used as a reference to monitor the dopant concentration. An example of ^{11}B probing is shown in Fig. 3.2. Normally beyond the 50-100 Å surface layer, the concentration of dopant is uniform throughout the bulk of the film (usually around 5000 Å). The detection limits of both boron and phosphorus atoms are around $10^{16}/cm^3$.

The measured results are shown in Fig. 3.3(a) and Fig. 3.3(b) for boron and phosphorus doped films respectively. In the case of boron doped films, the value S/R seems to remain quite constant in the range of gas ratio R investigated. We suggest that this invariance can be expressed by a linear relation $S=b(T)R$ to a good approximation, where b(T) is a proportional factor which strongly depends on the substrate temperature. In Fig.3.3(a), it varies between 4 and 50 in the temperature range from 500°C to 620°C. On the other hand, the S/R value for phosphorus doped films depends not only on the deposition temperature, but also on gas ratio which is shown clearly in Fig.3.3(b). The different behavior of the S/R ratio for B and P doped films suggests that the chemical reaction mechanisms in the two cases are different.

It is known that the rate of dissociation of the individual gases diborane, silane and phosphine decrease in the order (R.P. Clark et al., 1951, J.K. Bragg et al., 1951, J.H. Purnell et al., 1966 and D.M. Wiles et al. 1957): $B_2H_6 > SiH_4 > PH_3$. One might

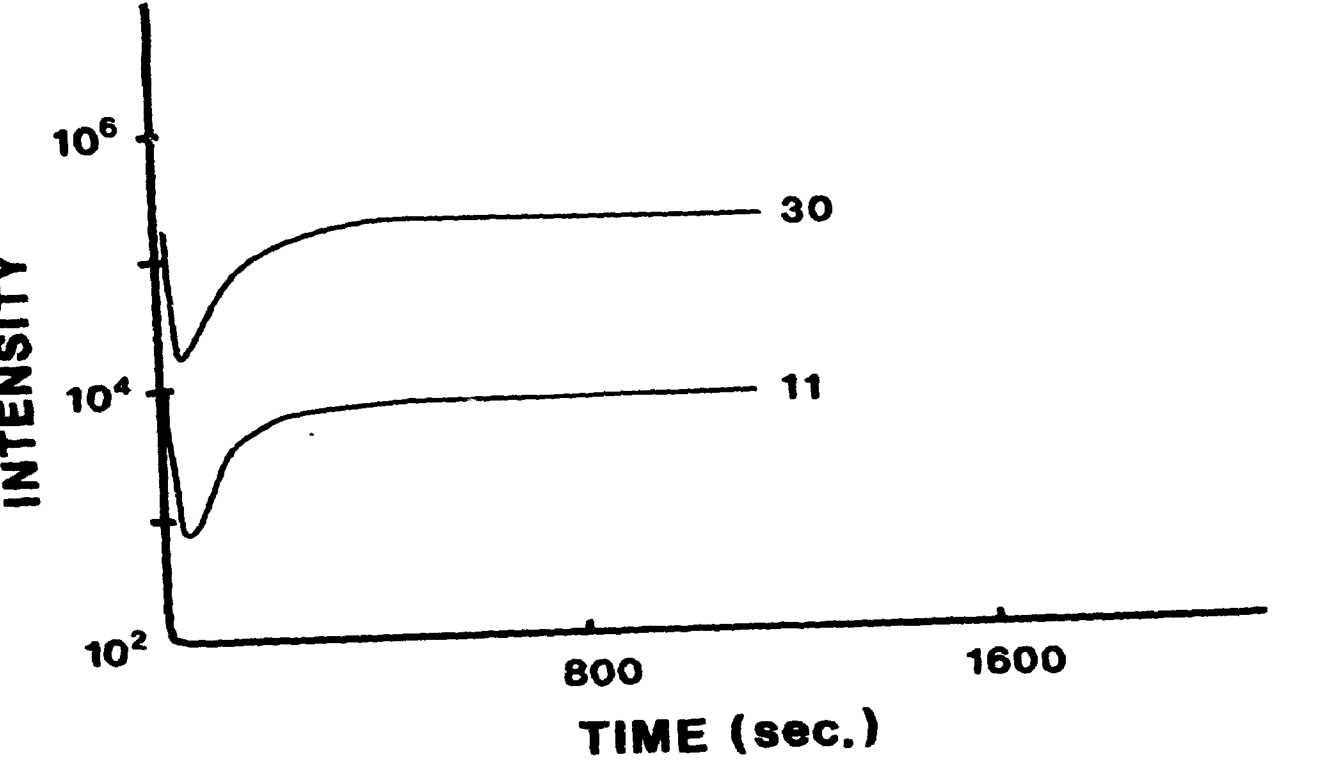

Fig. 3.2 The ^{11}B profile by SIMS of a typical boron doped film.

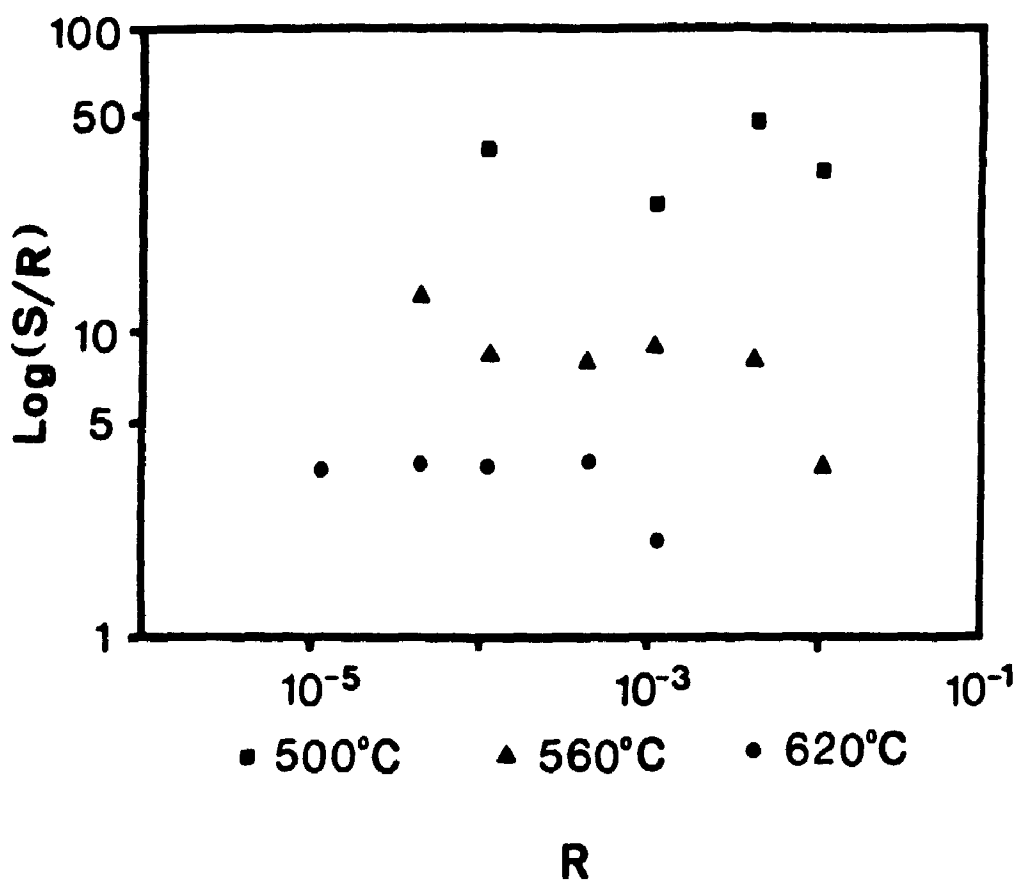

Fig. 3.3(a) The ratio of solid phase concentration and gas phase concentration S/R vs. gas phase concentration R for boron doped samples (substrate temperature Ts: ■ 500, ▲ 560, ● 620 °C).

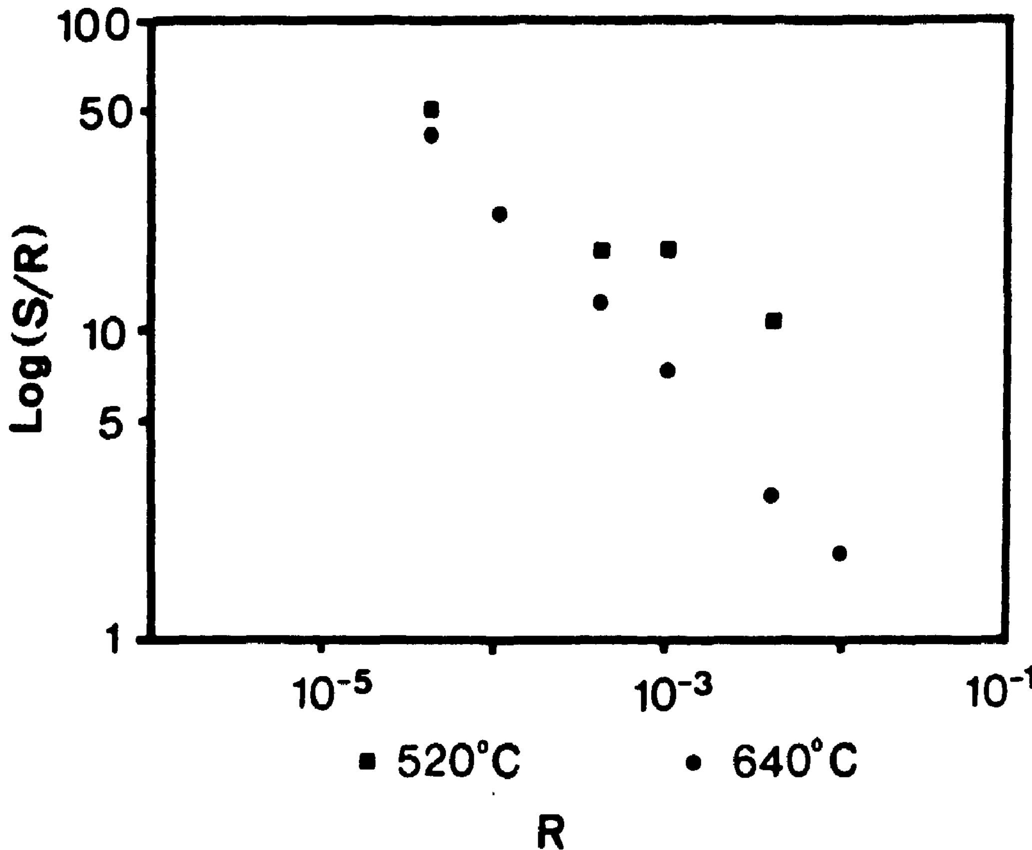

Fig. 3.3(b) The ratio of solid phase concentration and gas phase concentration S/R vs. gas phase concentration R for phosphorus doped samples (substrate temperature Ts: ■ 520, ● 640 ℃).

expect that the phosphorus concentration in the solid phase film would be less than that in the gas mixture if the decomposition of B_2H_6, SiH_4 and PH_3 were independent. However, experimental results show that for both boron and phosphorus doped films, the solid phase concentrations are all higher than that of gas mixture ratio. One has to consider the chemical reaction processes that take place between all species in the reaction chamber. In addition to these processes, the sticking coefficient of reactants to the growing surface must also play an important role. The functional relation between these parameters and film composition is unknown. A large change in dopant concentration in the solid film from 0.001% to 50% is observed in the range studied. Our strategy is to measure large number of samples at various fabrication conditions in order to gain a general trend of solid phase dopant concentration variations. SIMS measurements usually give us accurate results (better than 1% , for example). The uncertainty of the solid phase concentration in Fig. 3.3(a) and Fig. 3.3(b) is mainly due to the repeatability of the fabrication processes, which has been studied for some selected fabrication conditions. For example, 1.9 at.% , 7.5 at.% and 3.2 at.% were obtained for 3 repeated boron doped samples under the same fabrication conditions, e.g. $R=4\times10^{-3}$ and $T_s=540\ ^{\circ}C$. Our estimates of the standard deviation of the data points in Fig. 3.3(a) and Fig. 3.3(b) are in the range from 10% to 300% . The fabrication parameters have to be controlled carefully. A Vacuum General 84-4 flow/ratio controller with a range of 0 - 100 scc/min. was used for gas ratio control. The fluctuation of gas ratio readings are less than 5% . A variation of $\pm4\ ^{\circ}C$ in the

temperature distribution was generally observed in our reaction chamber. Other factors were gas pressure, the speed of gas flow, and the dilution of the carrier gas, the dependence on which has not been determined.

Many important consequences emerge when the true dopant concentration in the solid film is known. A few examples of boron doped LPCVD films will be mentioned here.

Fig.3.4 gives a 3-dimensional plot of boron concentration (S) in films deposited under the various conditions of gas ratio B_2H_6/SiH_4 (R) and substrate temperature (T_S). There is a sharp rise of S, boron concentration in solid phase, when R, boron concentration in gas phase, is larger than $1x10^{-3}$ and when the substrate temperature is below 500°C. Under the conditions reported here, S can peak at nearly 50 atom%. It is obvious that the material can no longer be regarded as a boron doped silicon film in the whole range of deposition conditions. We define that material containing more than 5% boron as silicon-boron alloy. The deposition conditions producing amorphous, alloy (also amorphous in structure), and microcrystalline materials are shown in Fig.3.5. Previous authors also realized that under certain conditions high concentration boron material (B/Si=0.7) was produced by the glow discharge method (C.C. Tsai et al., 1977).

Dark conductivity and photoconductivity of LPCVD microcrystalline material when plotted against the gas mixture ratio have the same general shape (Fig.3.6, 3.7). The curves are

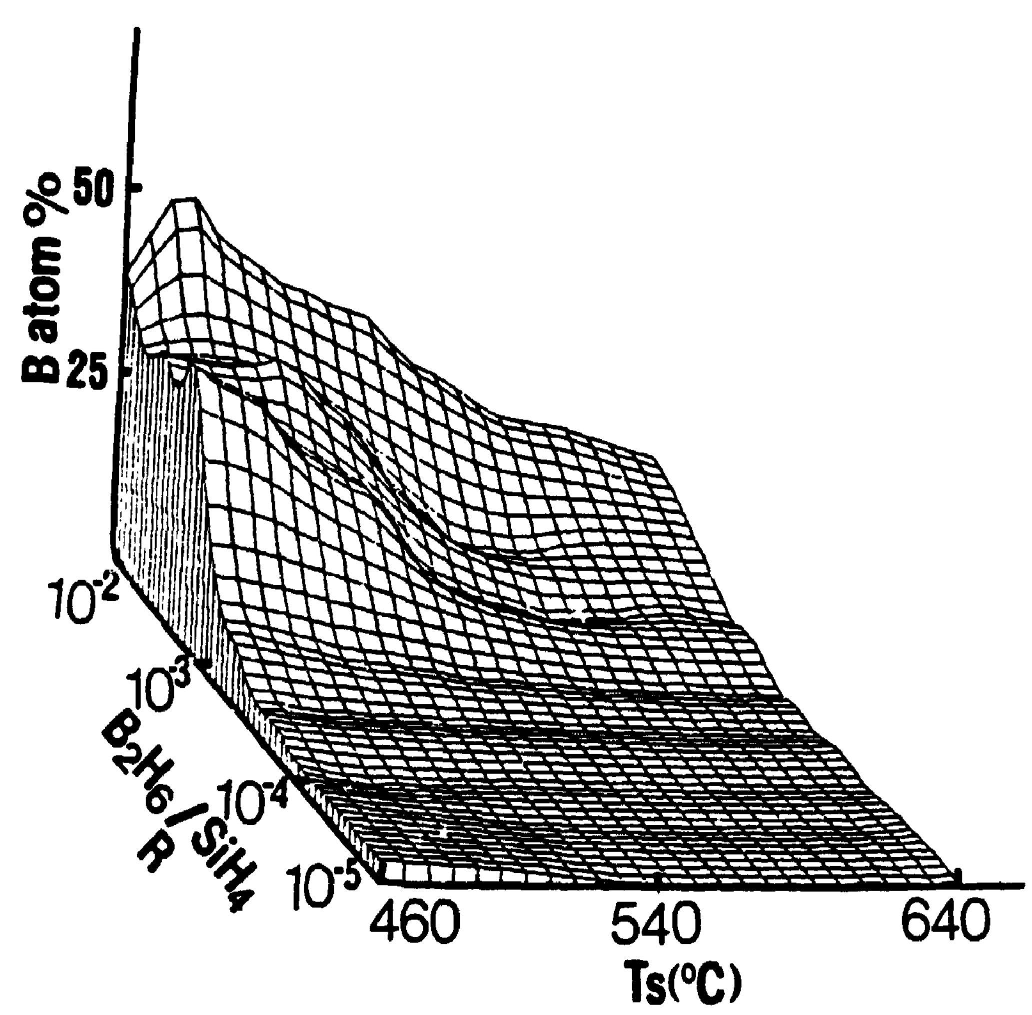

Fig. 3.4. Boron concentration in film varies as function of gas ratio R and substrate temperature T_s.

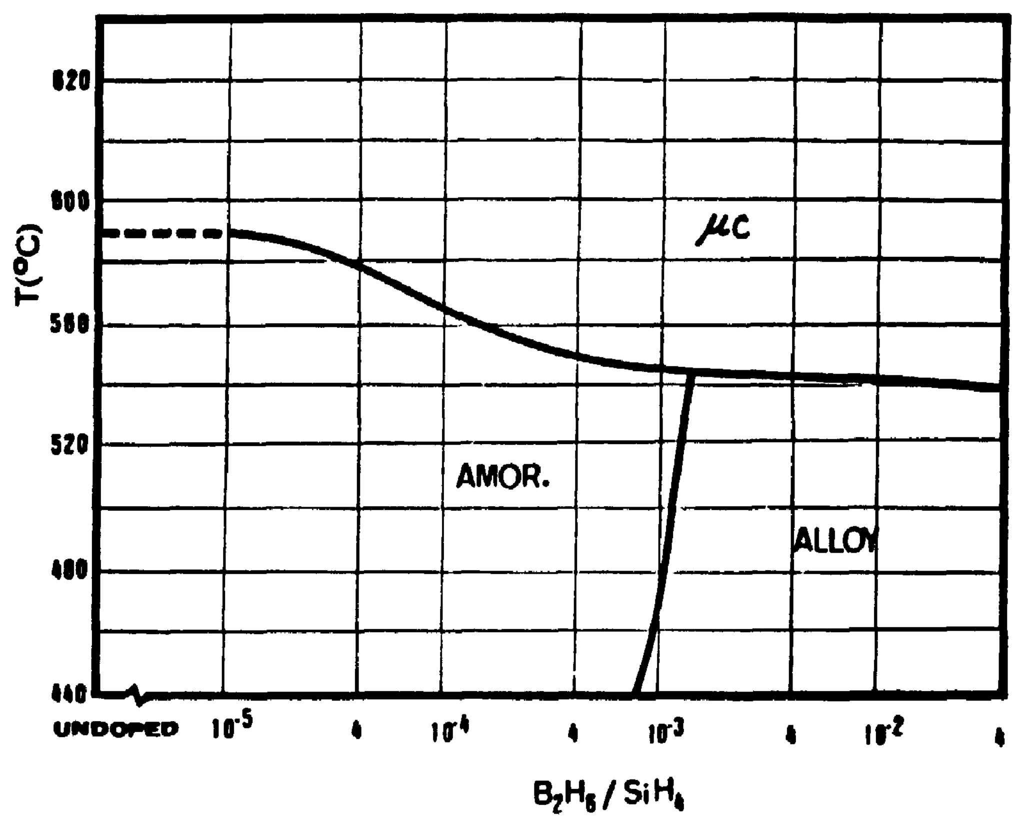

Fig. 3.5. Zones of different boron doped LPCVD-Si material: amorphous (AMOR.), amorphous alloy (ALLOY) and microcrystalline (μc).

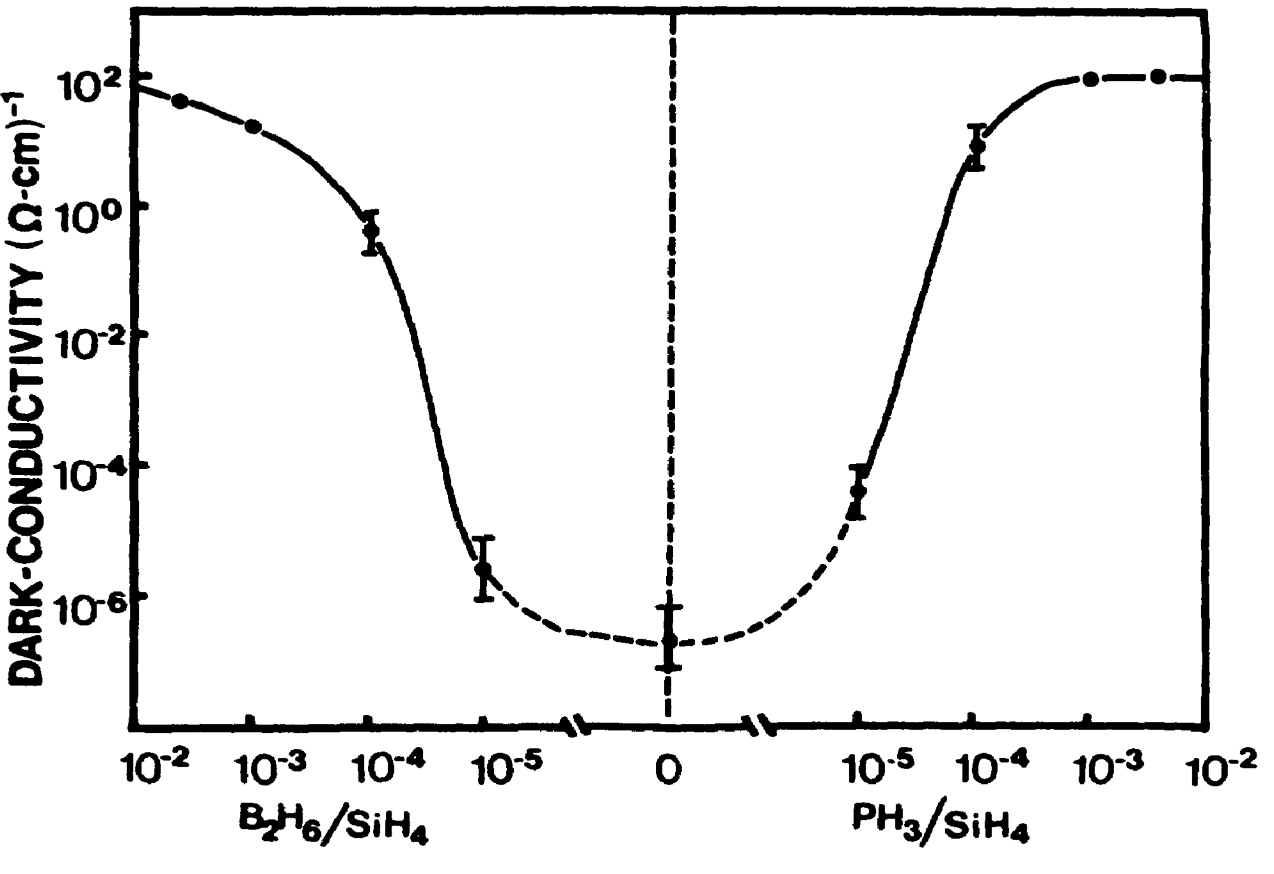

Fig. 3.6. Dark conductivity of microcrystalline films vs. gas ratio. Since no data points were available below $R=10^{-5}$, dashed line is used to connect the data points.

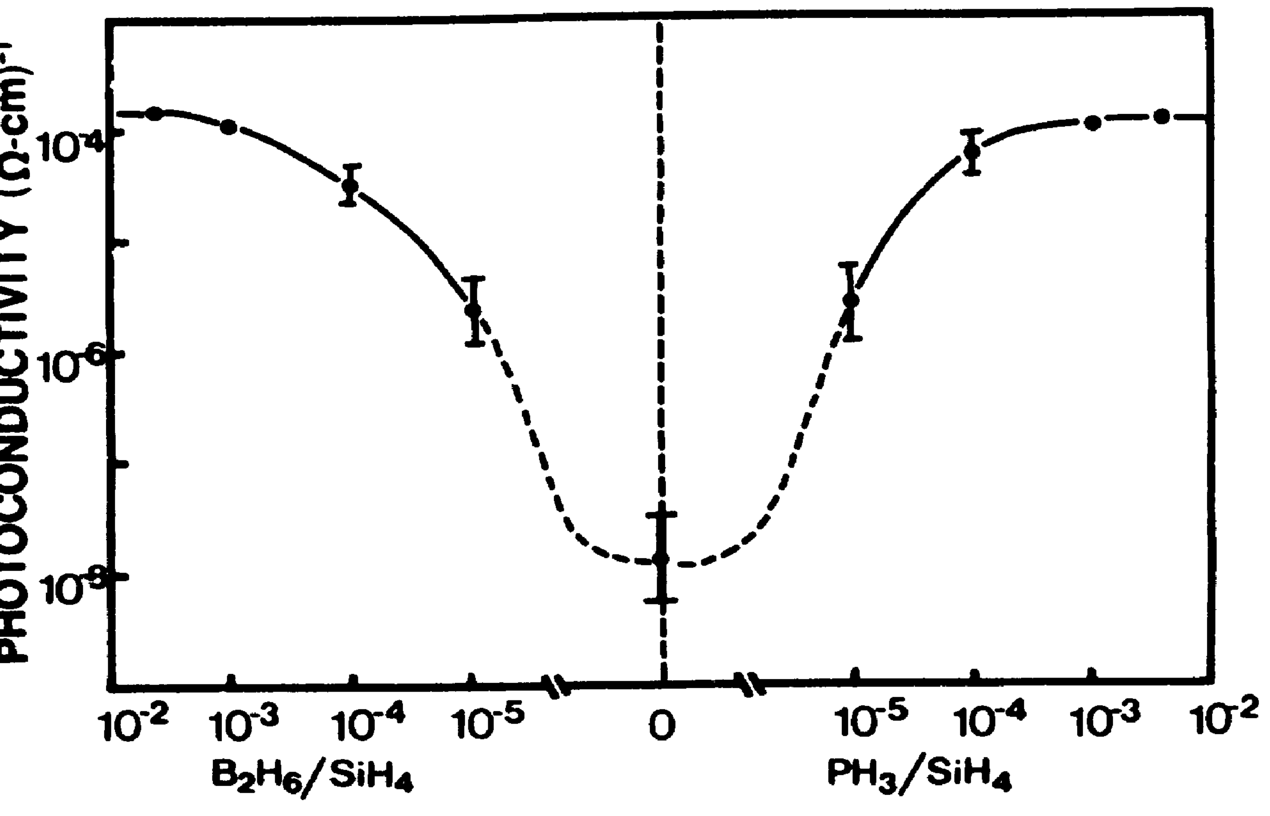

Fig. 3.7. Photo conductivity of microcrystalline films vs. gas ratio. Since no data points were available below $R=10^{-5}$, dashed line is used to connect the data points.

approximately symmetric about the zero dopant vertical axis. The same plot against the solid phase film concentration, however, do not have this symmetry (Fig.3.8, 3.9). Measurement results in Fig.3.8 indicate that dark conductivity of boron doped microcrystalline films increase rapidly when the solid phase concentration exceeds 1×10^{19} atoms/cm^3. For phosphorus doped films, the dramatic change in conductivity occurs when solid concentration is higher than 5×10^{19} atoms/cm^3. Therefore, boron doped microcrystalline films have higher doping efficiency than phosphorus doped ones. Below the solid concentration threshold of 10^{19}, the dark conductivity is insensitive to the dopant atoms, suggesting the phosphorus (or boron) atoms in the low doping range are doping inactive. The threshold value of 10^{19} is in agreement in magnitude with the ESR (Electron Spin Resonance) signals of undoped or very lightly doped microcrystalline samples which are generally correlated with defects due to dangling bonds. A detailed ESR measurement (X.W. Wu et al., 1987 and M. Hirose, 1978) shows that the dangling bond density of microcrystalline films decreases with the increase of phosphorus (or boron) solid phase concentrations (ESR signal decreases from 10^{19} to 10^{17}, for example), due to the compensation by P (or B) atoms. In microcrystalline Si films, dangling bonds are possibly located at grain boundaries (C.H. Seager et al., 1981 and P.M. Lenahan et al., 1984) and P (or B) segregation may occur. But we have little direct evidence at the present time.

In conclusion, the gas ratio R which usually serves as a fabrication parameter is not indicative of the physical properties

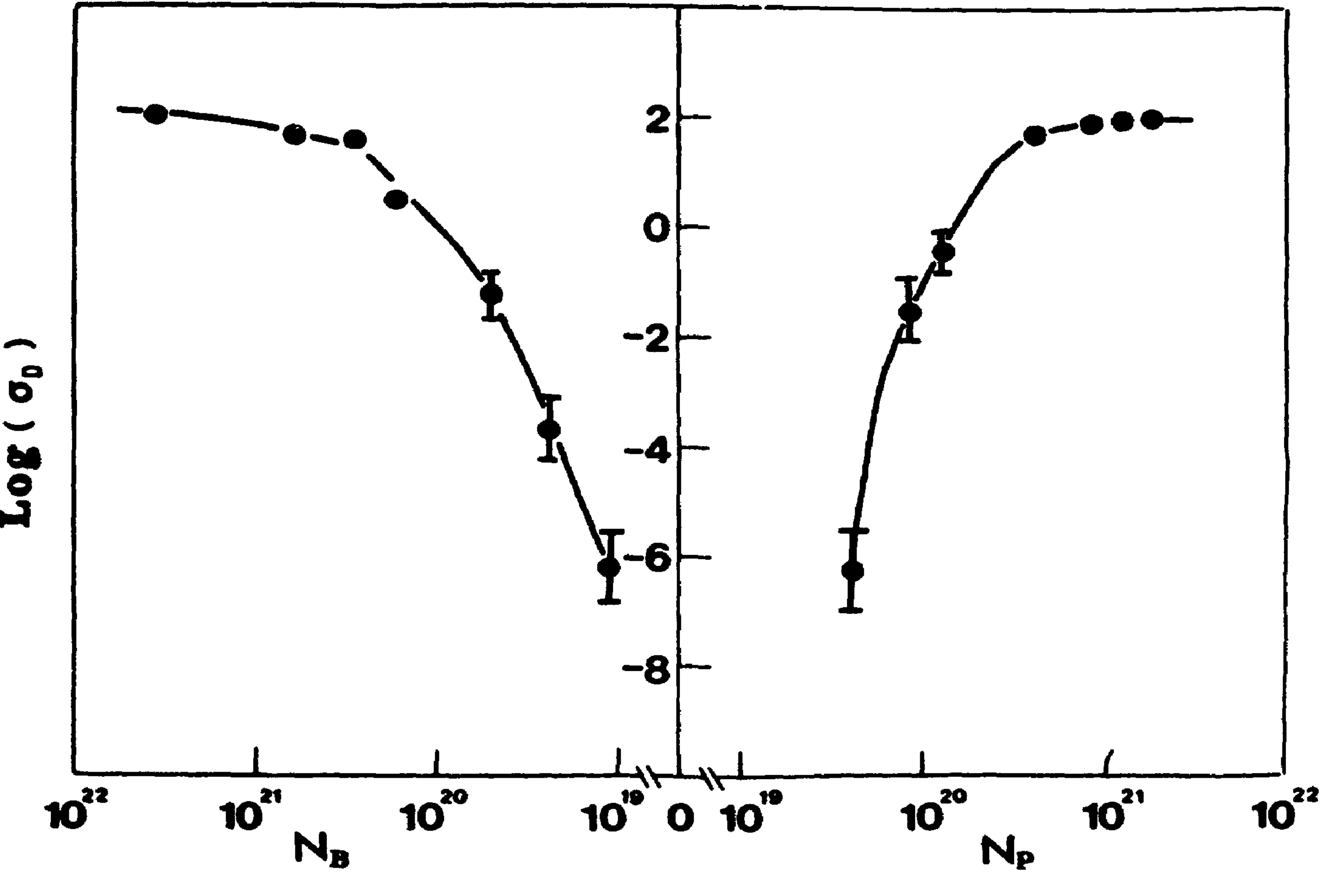

Fig. 3.8. Dark conductivity of microcrystalline films vs. solid phase concentration. N_B and N_P represent number of boron and phosphorus atoms in the films.

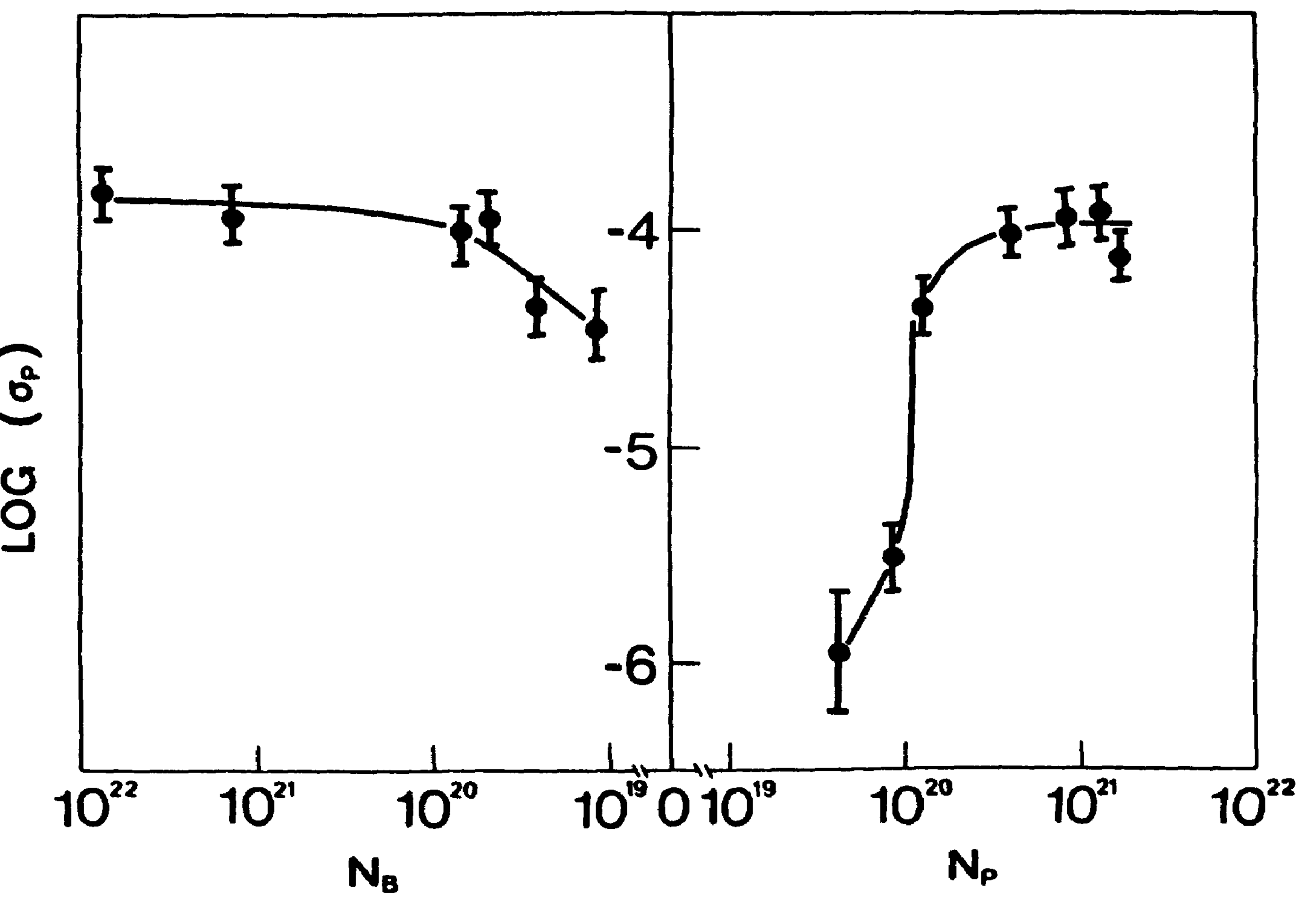

Fig. 3.9. Photo-conductivity of microcrystalline films vs. solid phase concentration. N_B and N_P represent number of boron and phosphorus atoms in the films.

of the deposited films. One has to measure the dopant concentration S in order to gain some insight into the properties of the film.

Chapter 4 Structure Characterization*

In chapter 3, we discussed the fabrication process of Si thin films by low pressure chemical vapor deposition (LPCVD) method and demonstrated that the substrate temperature T_s and gas flow ratio R ($R = PH_3 / SiH_4$ or $R = B_2H_6 / SiH_4$) are the two most important fabrication parameters which determine the dopant concentration (S) in Si films. Another even more important aspect of Si film is its network structure (whether it is amorphous or microcrystalline) because it is the structure of the material which largely determines its electrical, optical and other properties. In this chapter the structure of LPCVD Si thin films and its relation with T_s and R are studied systematically by the following approaches:

1) Direct structural characterization techniques such as X-ray diffraction, Raman scattering and transmission electron microscopy (TEM);

2) Transport properties of the films (conductivity, Seebeck coefficient, etc.) because a-Si and μc-Si are expected to have different electrical properties;

---

* *This chapter has been published in J. Appl. Phys. 66, 5894 (1989).*

3) The performance of a p-n heterojunction fabricated by n type LPCVD Si films on top of p type c-Si wafer.

4.1 Direct Structural Analysis

4.1.1 Determination of Film Thickness

Most of our films have a thickness of several thousand Å. The thickness was measured using a stylus (Dektak M-611(0) at Surface Science Western) with a thickness resolution of 50 Å. In order to create the substrate-film step for the measurement, part of the substrate was covered with graphite. It was then removed after deposition to expose the bare substrate surface. To check this measurement, a secondary ion mass spectrometry (SIMS, Cameca IMS 3f of Surface Science Western) depth profile for Si was made. The results of the two methods agreed within the experimental error.

4.1.2 X-ray Diffraction

All the LPCVD Si samples were subjected to X-ray diffraction analysis. Crystalline samples usually show some characteristic diffraction peaks while for amorphous samples, no peaks are observed. Fig. 4.1 shows typical diffraction scansfor μc-Si and a-Si. If we map X-ray results with fabrication parameters T_s and R, two-dimensional diagrams are obtained as in Fig. 4.2 (P doped films) and Fig. 4.3 (B doped films). One can clearly see that for our fabrication conditions, both a-Si and μc-Si can be obtained. The crystallinity of the Si film is more sensitive to substrate temperature than it is to gas ratio R. With increase in substrate temperature, the structure of the material gradually change from amorphous to microcrystalline.

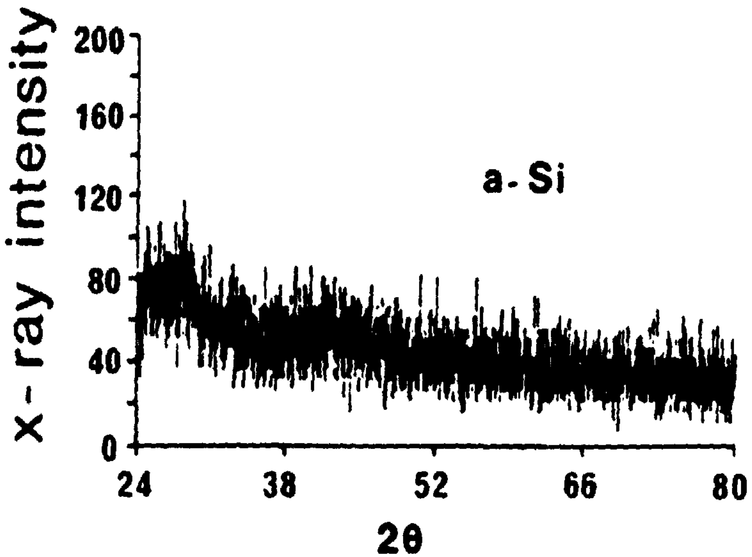

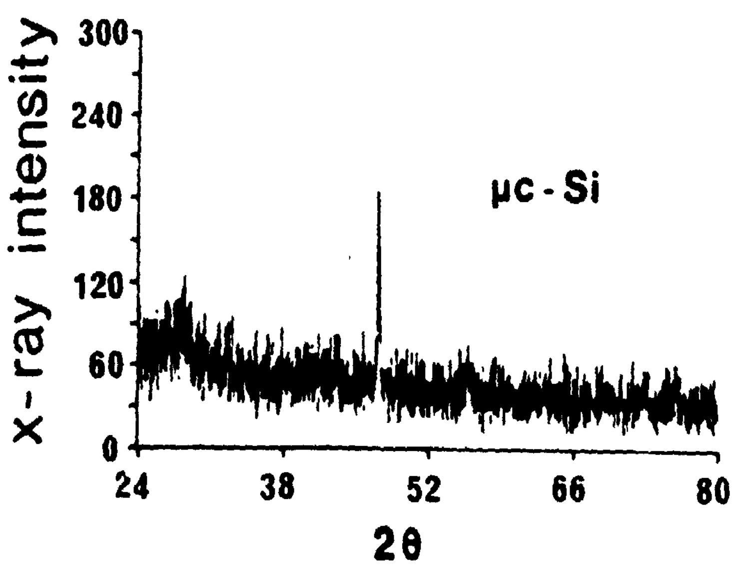

Fig. 4.1. X-ray diffraction of a-Si and μc-Si.

Fig. 4.2. X-ray results of P doped samples as function of gas ratio R and substrate temperature T_s.

Ratio / T(°C)	1×10^{-5}	4×10^{-5}	1×10^{-4}	4×10^{-4}	1×10^{-3}	4×10^{-3}	1×10^{-2}
500	No peaks	No peaks	No peaks	No peaks	No peaks	No peaks	No peaks
520	No peaks	No peaks	No peaks	No peaks	No peaks	No peaks	No peaks
540	No peaks	No peaks	No peaks	No peaks	No peaks	No peaks	No peaks
560	No peaks	No peaks	No peaks	No peaks	No peaks	No peaks	No peaks
580	No peaks	No peaks					
600							
620							
640							

Fig. 4.3. X-ray results of B doped samples as function of gas ratio R and substrate temperature T_s.

T(°C) \ Ratio	1×10^{-5}	4×10^{-5}	1×10^{-4}	4×10^{-4}	1×10^{-3}	4×10^{-3}	1×10^{-2}
480	No peaks	No peaks	No peaks	No peaks	No peaks	No peaks	No peaks
500	No peaks	No peaks	No peaks	No peaks	No peaks	No peaks	No peaks
520	No peaks	No peaks	No peaks	No peaks	No peaks	No peaks	No peaks
540	No peaks	No peaks	No peaks	No peaks	No peaks	No peaks	No peaks
560	No peaks	No peaks		No peaks			
580							
600							
620							

4.1.3 Raman Spectroscopy

X-ray diffraction gives us a general trend of the structural changes of Si film with fabrication conditions (Fig. 4.2 and 4.3). With the X-ray data, one at least knows qualitatively where the a-Si/μc-Si boundary lies. For the materials in the transition area, more detailed structural analysis has been further carried out by Raman spectroscopy. Raman is a powerful technique because of its sensitivity to the structural changes in the material. In particular, some very important information about the short range order of the material network can be obtained by Raman spectroscopy. For example, the bond angle fluctuation of a-Si or a-Ge can be derived from Raman spectrum (Kshirsagar and Lannin, 1982). Our Raman spectrum was obtained at Surface Science Western (DILOR OMARS 89) by Dr. I. Hill. The wave length of the laser beam was 514.5319 nm and the laser power was between 25 mW to 80 mW.

Fig. 4.4 is the Raman result for typical phosphorus doped amorphous ($R=4x10^{-3}$, T_s = 540 °C) and microcrystalline (R = $1x10^{-3}$, T_s = 600 °C) samples. For comparison, a spectrum of P doped single crystal Si (c-Si) is also included in Fig. 4.4. The Raman peak for c-Si is situated around 520 cm^{-1} while the broad peak near 475 cm^{-1} is characteristic of amorphous Si (Kshirsagar and Lannin, 1982). For μc-Si, the peak is shifted towards high wave-number direction.

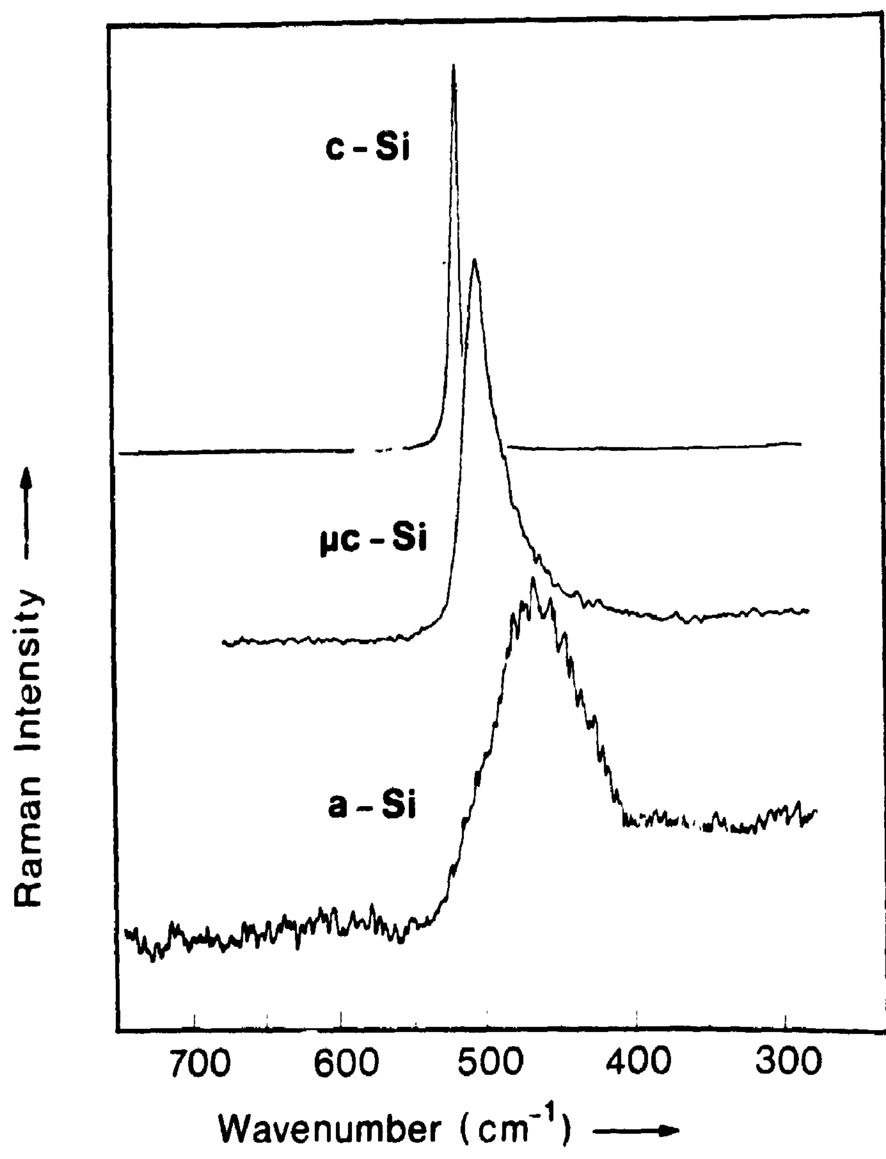

Fig. 4.4. Raman scattering results of a-, µc- and c-Si.

4.1.4 Transmission Electron Microscopy (TEM)

Transmission electron microscopy (TEM) results of a-Si as well as μc-Si are shown in Fig. 4.5 (HITACHI H-800 at Dept. of Pathology. The electron acceleration voltage was 100kV and the magnification was 0.4 -1.5 k). The amorphous sample shows typical diffused diffraction rings which are associated with the lack of long range order. In the case of μc-Si, sharp rings and some times scattered diffraction spots are observed. Amorphous samples usually have smooth surface under electron microscopy while for μc-Si films, some columnar microstructure were observed, especially when the film is relatively thick (over 1 μm, for example).

Raman scattering and TEM are generally more sensitive to structural changes of materials than X-ray diffraction. This becomes very important for samples close to the a-Si ⟶ μc-Si transition boundary. In some cases the samples show no X-ray diffraction peaks, while Raman and TEM clearly indicated that they are μc-Si.

4.2 Material Structure and Transport Properties

Electrical transport properties of Si thin films can be used as an indirect approach to study the influence of T_s and R on the network structure because the electrical properties of the material are usually closely related to its network structure and should reflect its changes. While it is difficult to assess the sensitivity of this approach to small structural changes (average

a- Si

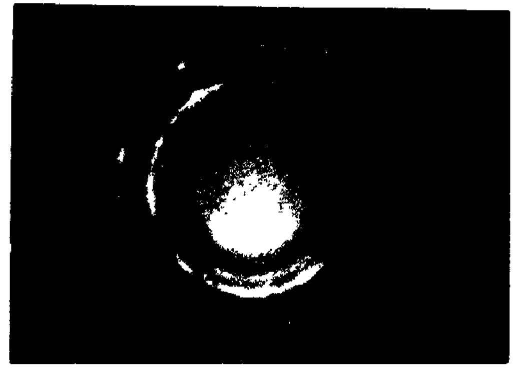

μc - Si

Fig. 4.5. Transmission electron microscopy (TEM) of a- and μc-Si.

bond angle, for example) in a-Si, drastic structural change such as a-Si to μc-Si transition should be reflected in electrical transport properties. The conductivity measurement (σ), when combined with Seebeck coefficient S, can give us important information about different current transport processes and paths in a-Si. S is an energy-weighted sum of the microscopic conductivity $\sigma(E)$ of the material and is therefore sensitive to which energy path contributes most to the conduction process. In literature, σ and S are the most widely studied aspects of a-Si because of their practical importance (Chik, Chan, Tam, Tong, Wong and John, 1989, Jones, Le Comber and Spear 1977, Beyer, Mell and Overhof 1977, Jan, Bube and Knights 1979, Anderson and Paul 1982, Zimmer, Bube and Knights 1989, Ghiassy, Jones and Stewart 1985). In this section, the effects of T_S and R on conductivity and thermoelectric power are presented. One will see that a-Si $\longrightarrow$ μc-Si transition from transport property study agrees well with the result from direct structural analysis techniques of § 4.1.

4.2.1 Conductivity

The general features of room temperature dark-conductivity (σ) of various n type films fabricated under varying substrate temperatures (T_S) and gas ratios (R) are shown in Fig. 4.6. One notices that there is a large change in conductivity (by several orders of magnitude) in each curve at a certain substrate temperature. With increase in R, it shifts towards lower temperatures . Beyond T_S = 580°C and R = 1 x 10^{-3}, the conductivity is high and remains saturated. The drastic change in conductivity around 560 - 580 °C is clearly an indication of

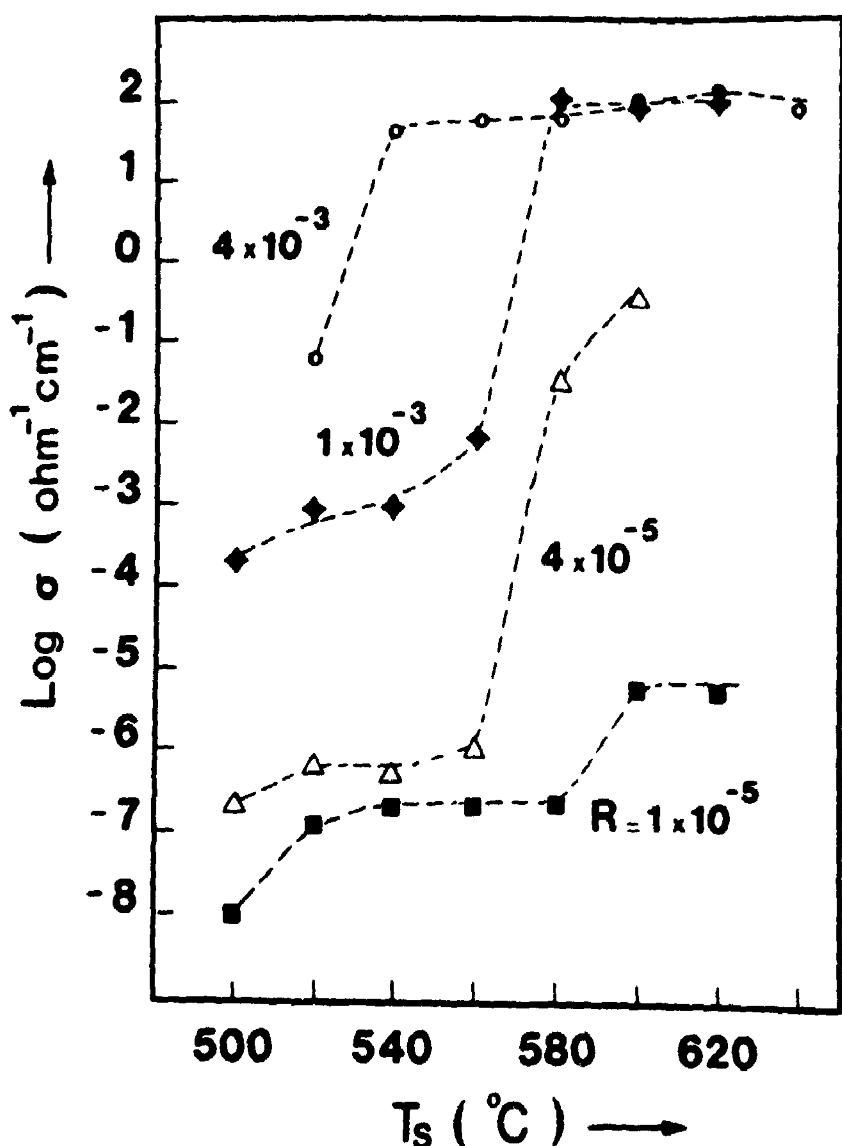

Fig. 4.6. Conductivity σ vs. substrate temperature T_s of P doped samples.

structure transition from a-Si to μc-Si. μc-Si has lower defect density and better lattice structure, and its doping efficiency (the ratio of carrier concentration and solid phase dopant concentration) and drift mobility are much higher than those of a-Si. The conductivity of μc-Si should also be much higher. The structure of the films has been examined by x-ray diffraction, Raman spectroscopy and transmission electron microscopy measurements (§ 4.1). The transition temperature from a-Si to μc-Si obtained by those methods agrees well with what is observed in transport property measurement. Based on these data, an amorphous-microcrystalline transition temperature close to 560 - 580°C for phosphorus doped films was identified . Notice that at R = 4 x 10^{-3}, there is a range from T_s = 520 - 560°C which produces amorphous silicon which has high conductivity. Optical band gaps of the various silicon films were measured to be in the range 1.2 to 1.6 eV, progressively increasing for amorphous films. Boron doped films have similar results. A-Si to μc-Si transition temperature for p type film is lower than that of n type films. Typically it is around 440 - 460 °C.

The influence of gas ratio R on conductivity σ is shown in Fig. 4.7 (n type) and Fig. 4.8 (p type). Again, there exists a sudden change in conductivity at a certain gas ratio R which also depends on substrate temperature T_s: at higher T_s, it shifts to lower R values. This means that the Si film fabricated at high temperature (μc-Si) has higher doping efficiency than those fabricated at lower temperatures (a-Si). The drastic change in conductivity here is clearly due to doping effect, i.e., the Fermi

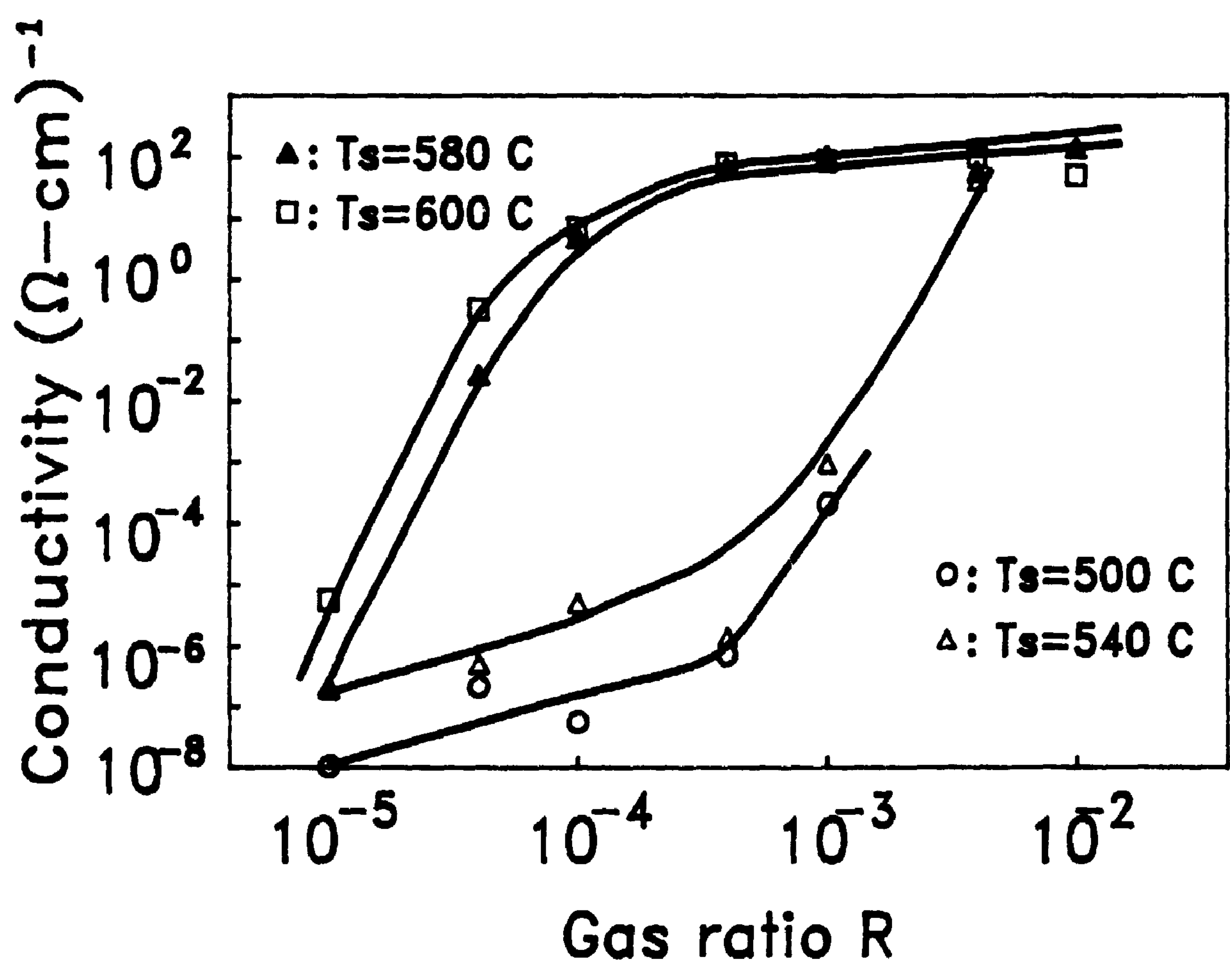

Fig. 4.7. Conductivity σ vs. gas ratio R of P doped samples.

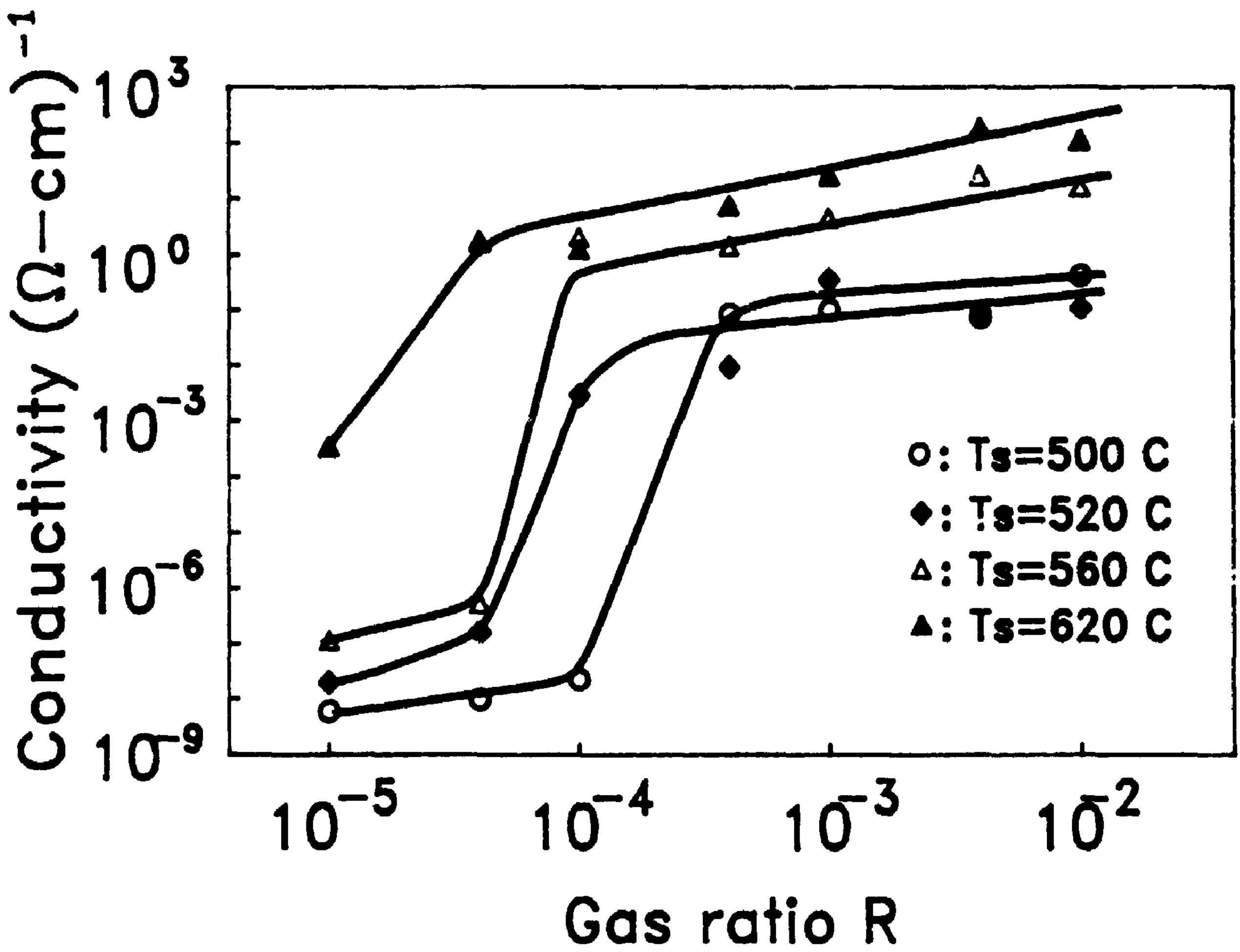

Fig. 4.8. Conductivity σ vs. gas ratio R of B doped samples.

level is shifted by the introduction of P or B atoms into Si. From SIMS study in chapter 3, we knew that a-Si has much higher solid phase concentration S than μc-Si under the same gas phase ratio R and even in the low conductivity range in Fig 4.7 and Fig. 4.8 , P (or B) concentration in Si film can still be quite high. Obviously not all doping atoms (P or B) are doping active in Si films. In fact, the doping efficiency of a-Si is usually very low. The reasons are probably twofold: first, P (or B) atoms can act as dopant only in a 4-fold environment such as c-Si. In a-Si, due to the relaxation of network structure, large number of B (or P) atoms will be in 3-fold configurations.* The doping efficiency of a-Si is thus considerably reduced. Secondly, the existence of unpaired dangling bonds in the middle of the band gap traps electrons, reducing the carrier concentration in conduction band and thus also lowering the doping efficiency. While those two processes may coexist in a-Si, Hall effect results indicate that the latter dominates in μc-Si films (see § 5.3.2 of chapter 5) where the threshold value of solid phase concentration for filling up the dangling bonds is almost identical to the value of dangling-bond density. This is easy to understand because when the material network structure changes from a-Si to μc-Si, most of the dopant atoms are forced into fourfold configuration. The dangling bonds, however, will still exist, particularly in the region of grain boundaries. Our electron spin resonance (ESR) measurements

---

* *According to N.F. Mott (Adv. Phys.16, 49, (1967)), the atomic coordination in random network follows the "8-N" rule: the atoms bonded into amorphous solid should have a coordination of min(N, 8-N), where N is the number of valence electrons. Following this rule, both B (N=3) and P (N=5) have 3-fold configurations.*

show that both undoped a-Si and μc-Si have basically the same dangling-bond density (in the order of 5×10^{19} cm^{-3}). Comparing with a-Si, μc-Si should have higher doping efficiency because only one mechanism operates. This is also why a single electrical compensation model works so well in the case of μc-Si (this model is presented in chapter 5).

The network structure change from a-Si to μc-Si is also clearly reflected in conductivity vs. temperature measurements. Conductivity (σ) as a function of inverse temperature (1/T) yields important information about the electron transport process in the material such as the position of Fermi level, the different conduction path at different temperatures, etc. (see chapter 2). Fig. 4.9 are the results of σ vs. 1/T of P doped films fabricated at $R = 1 \times 10^{-3}$ and T_s from 540 °C to 620 °C. The slope of the curve at higher temperature yields the position of the Fermi level. It shifts drastically towards conduction band as the T_s passes the transition temperature from a-Si to μc-Si. Fig. 4.10 is σ vs. 1/T of B doped films.

4.2.2 Thermoelectric Power

Thermoelectric power measurements were made by P.H. Chan and K.P. Chik at The Chinese University of Hong Kong (P.H. Chan, 1988). With their permission, we will quote some of the results here.

Fig. 4.11 shows Seebeck coefficient as a function of 1/T for P doped samples fabricated at $R = 1 \times 10^{-3}$ and T_s of 520, 560 and

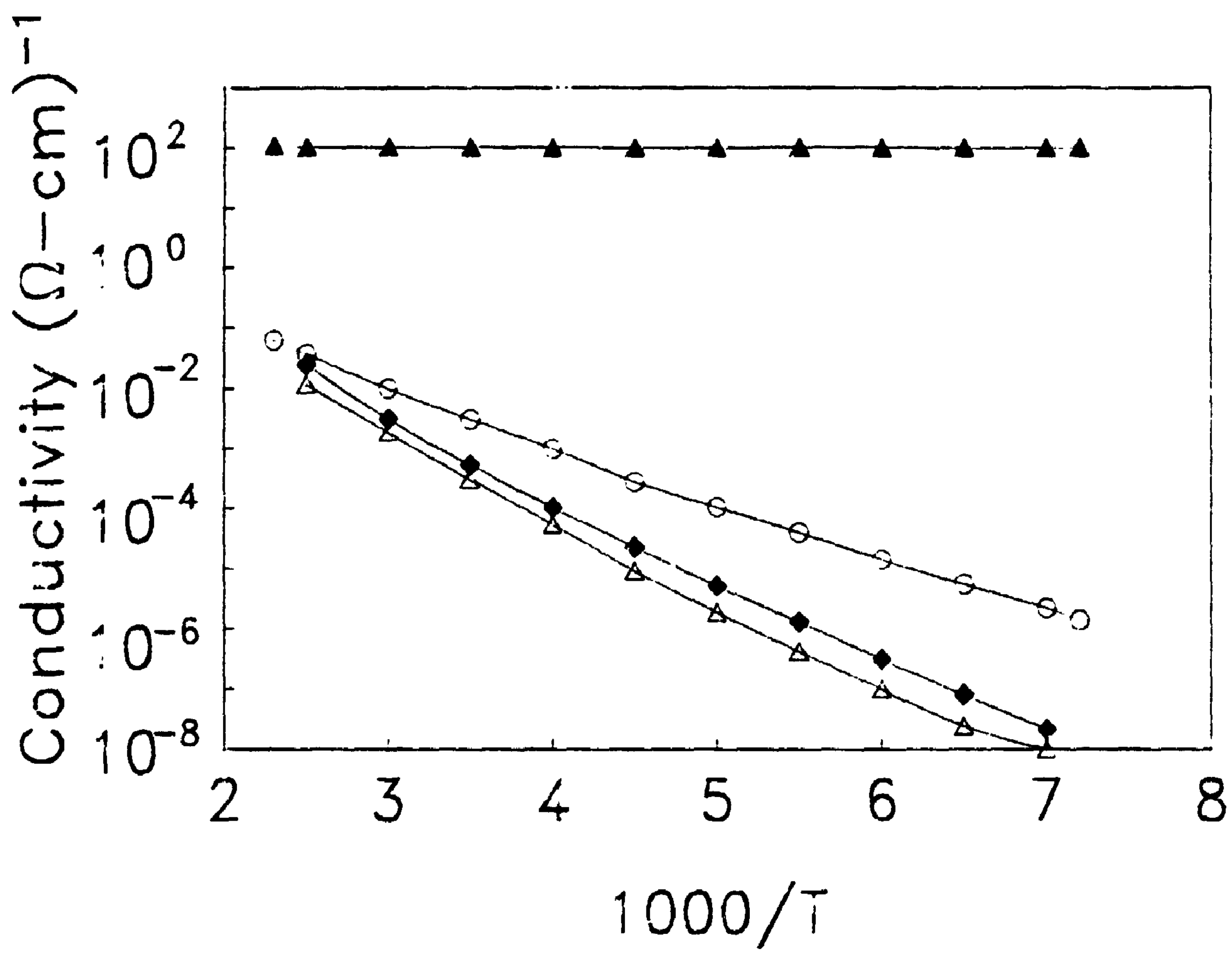

Fig. 4.9. σ vs. 1/T of heavily P doped samples ($R = 1 \times 10^{-3}$).

△ :500, ◆ :520, ○ :540, ▲ :580 °C.

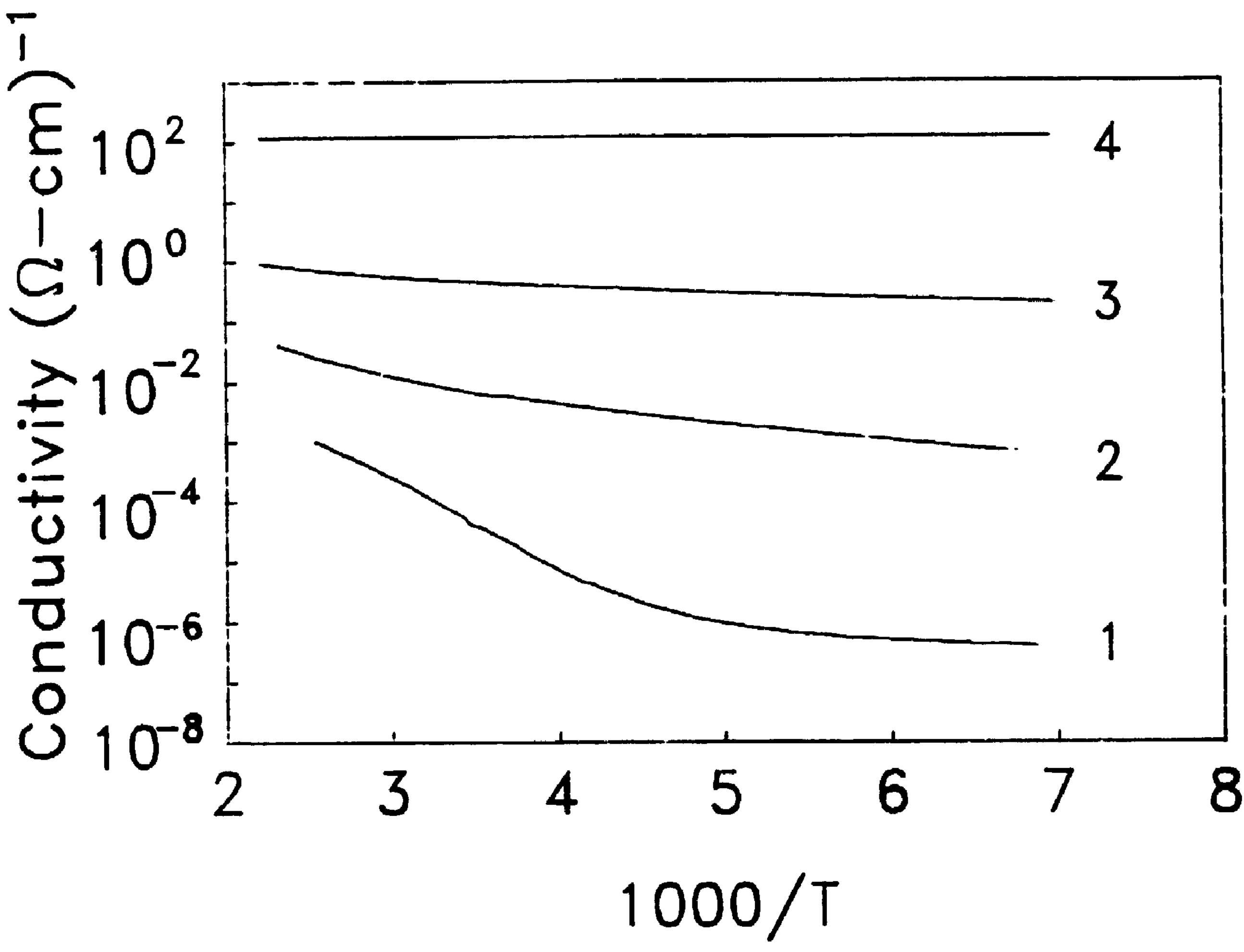

Fig. 4.10. σ vs. 1/T of B doped samples ($R = 4 \times 10^{-4}$).
1 :460, **2** :520, **3** :540, **4** :580 °C.

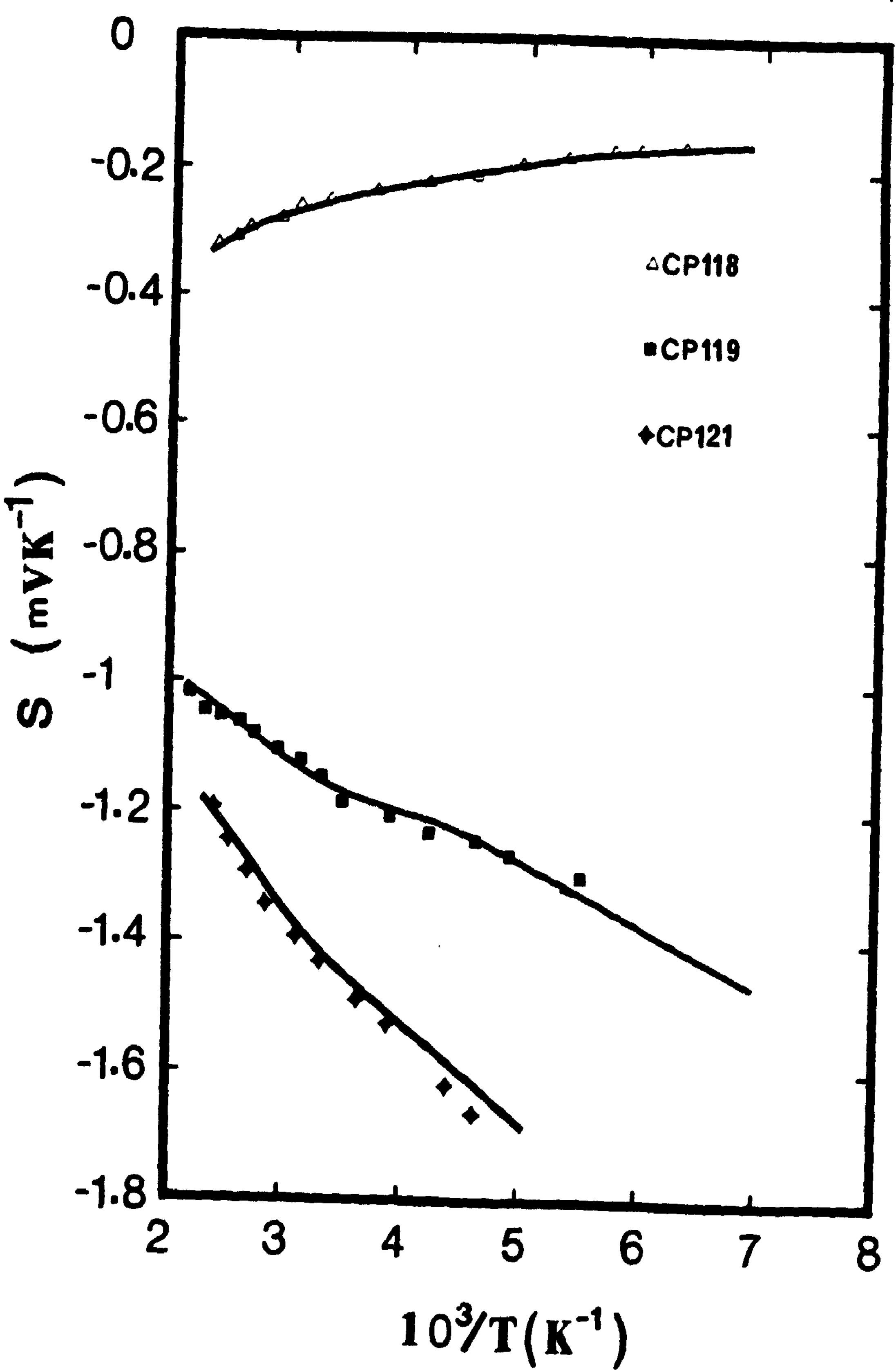

Fig. 4.11. Seebeck coefficient S vs. 1/T for typical a- (CP-121, CP-119: R=1x10^{-3}, T_s=520, 560 °C) and μc- (CP-118: R=1x10^{-3}, T_s=580 °C) Si.

580 °C. As the material structure changes from a-Si to μc-Si, the behavior of Seebeck coefficient also changes drastically. Spear et al. reported the same results for glow discharge a-Si:H (Willeke, Spear, Jones and Le Comber, 1982). Seebeck coefficient is an energy-weighted sum of the microscopic conductivity σ(E) of the material, it is therefore sensitive to which energy path contributes most to the conduction process. Jones et al. (Jones, Le Comber and Spear, 1977) proposed a two-conduction-path model to interpret their data. Recently, K.P. Chik and his co-workers (Chik, Chan, Tam, Tong, Wong and John, 1989, P.H. Chan, 1988) have developed a three-path-conduction model, i.e. conduction via conduction (or valence) band, the band tail and a dopant related impurity band. The conductivity and thermoelectric power data of our LPCVD sample can be fitted very well by this model.

4.3 Material Structure and p-n Heterojunction Performance

The p-n heterojunction structure used in this study consists of a layer of n-type LPCVD Si thin film deposited onto p-type single crystal Si wafers under various fabrication conditions. This is an interesting research subject because amongst their potential applications, a-Si films have shown great promise as efficient photo-absorbers in photovoltaic devices. This particular heterojunction is frequently used in tandem solar cells as base cells. In this context, junction profiles and device characteristics have been more thoroughly investigated in metal/a-Si:H Schottky barriers (C.R. Wronski et al., 1976 and Y. Mishima et al., 1981) and to a lesser extent in p-n junctions (W.E. Spear et al., 1976) formed from films (a-Si:H) deposited by

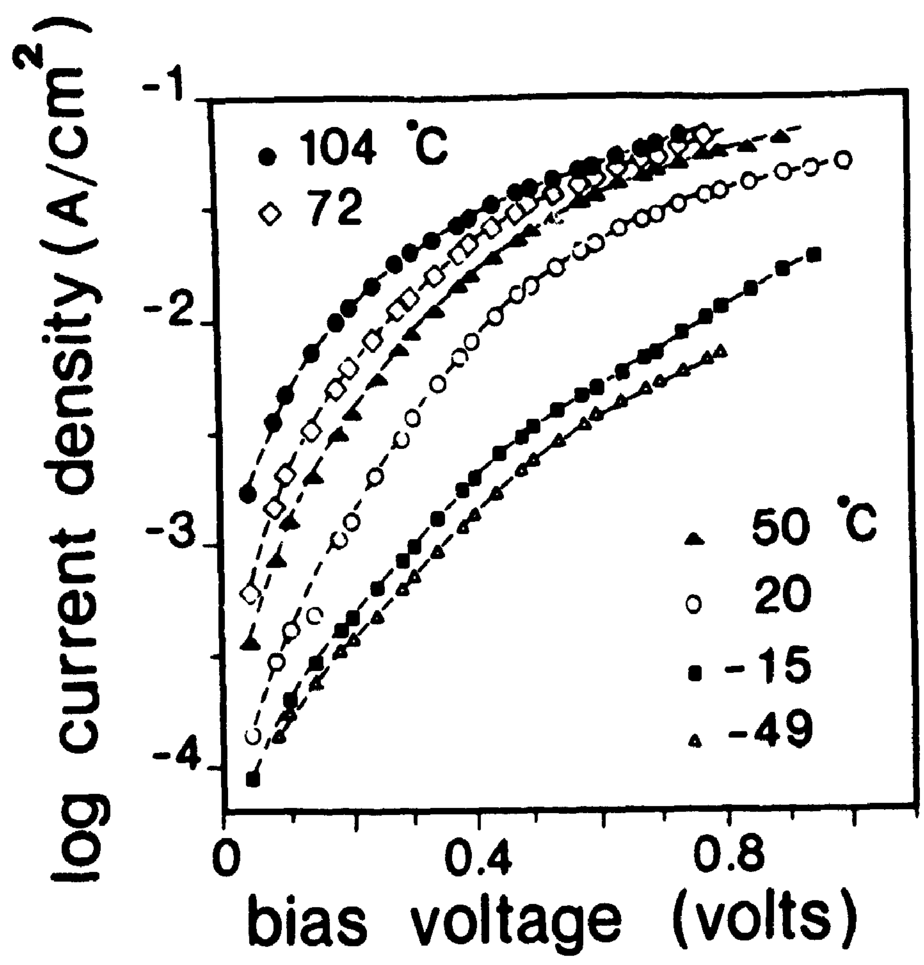

Fig. 4.14. Forward dark I-V characteristics of diode CP 116 at different temperatures.

4.3.1 Experimental Procedures

The LPCVD system used to fabricate doped Si films operates at a constant pressure of 3 Torr with a constant flow rate of 80 standard cubic centimeter per minute of either 3% or 10% SiH_4 in Argon. Films are doped by copyrolysis of silane mixed with phosphine. The dopant gas-to-silane ratio (R) varied between 4 x 10^{-5} to 1 x 10^{-2}. The substrate temperature (T_S) was varied from 460 to 640°C. Cleaned single crystal (p-type, <100>) Si substrates (5 - 15 ohm cm) were mounted in a cavity within a silicon-coated graphite reactor.

As-deposited Si films were first characterized by evaluating their hydrogen content (nuclear resonance reaction with N^{15}), phosphorus concentration (SIMS), crystallinity (x-ray diffraction), electrical conductivity, etc. as a function of deposition parameters namely T_S and R. Hydrogen and Oxygen concentrations were found to be less than 0.5 and 1 atomic percent, respectively. Phosphorus concentration increased with dopant gas ratio as expected, whereas for higher substrate temperature the concentration decreases (see chapter 3).

Using evaporated aluminium contacts on the n-a,μc:Si/p-c:Si diodes, dark I-V (current - voltage) curves at different temperatures were measured in a small vacuum chamber capable of maintaining stable temperatures in the range -150°C to +200°C. Illuminated I-V characteristics were measured on cells with an active area of 0.16 cm^2 (excluding the area shaded by Al

electrodes) at a light intensity of 100 mW/cm^2.

4.3.2 Results

1). <u>Room temperature, forward dark I-V characteristics:</u>

(a) Influence of substrate temperature

The forward I-V curves of diodes fabricated at constant doping ratio $R = 1 \times 10^{-3}$ and different temperatures T_s = 620, 580 and 500°C are plotted in Fig. 4.12. Three linear portions are seen in the low T_s regime which are characterized by different slopes in the voltage bias range studied. The first transition occurs at about 0.4 volts and the second is around 0.7 volts. The second transition is the effect of series resistance. In the low bias range, the two-slope behavior is clearly discernible in films which are deposited at low temperatures and low dopant ratios. On the other hand, the curve has only one distinct linear portion in the low bias range for samples fabricated at high substrate temperature. These features suggest two different transport mechanisms acting in series or in parallel combination. The magnitude of the dark currents also varies in these samples, as may be expected with changes in doping concentration or crystalline structure in the a-Si layer.

(b) Influence of gas ratio

At T_s = 540°C and R ranging from $4 \times 10^{-[illegible]}$ to 4×10^{-3}, the I-V curves of all diodes (CP 102, CP 120, CP 145 in Table 4.1) reveal the two-exponential behaviour similar to that of the diode fabricated at T_s = 500°C in Fig. 4.12.

2). <u>Forward dark I-V characteristics and their temperature dependence:</u>

Table 4.1.

Fabrication details of a,μc-Si films used for diode I-V measurements.

Dopant gas-to Silane ratio	Substrate Temperature T_s ($^{\circ}$C)			
R	620	580	540	500
1×10^{-2}	CP 148	---	---	---
4×10^{-3}	CP 154	---	CP 145	---
1×10^{-3}	CP 116	CP 163	CP 120	CP 122
4×10^{-4}	CP 164	---	CP 102	---

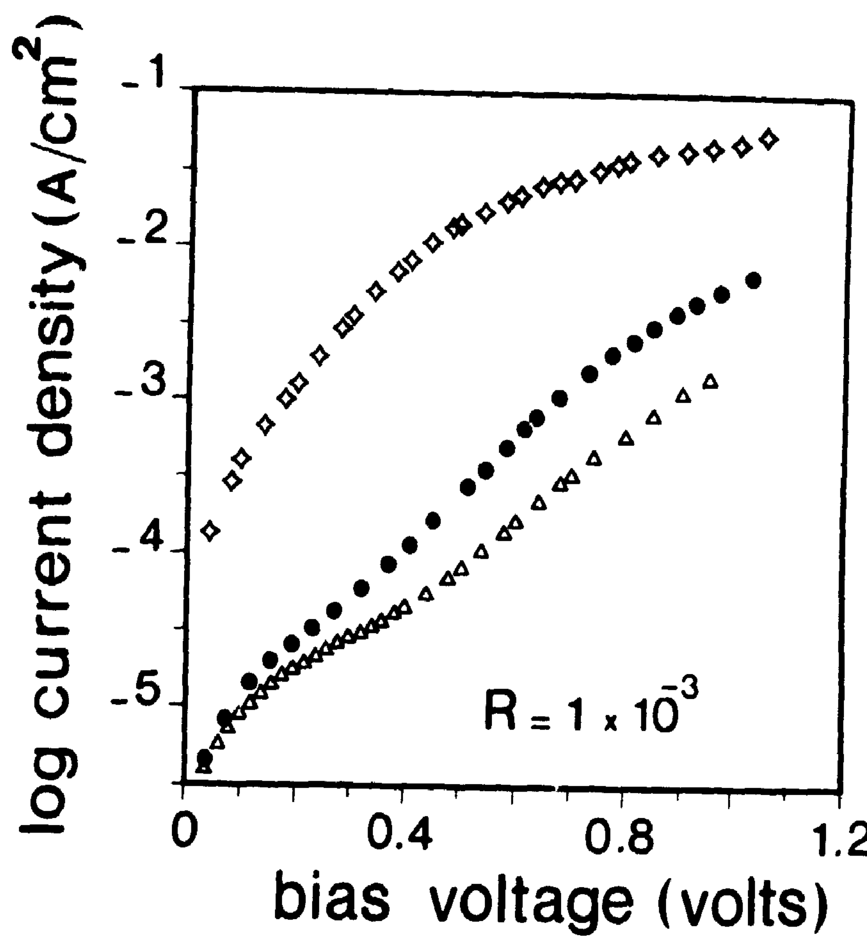

Fig. 4.12. Forward dark I-V characteristics of n-a,μc:Si/p-c:Si diodes at room temperature: ◇ CP 116, ● CP 163, Δ CP 122.

To extract the transport parameters and to identify the current loss mechanisms clearly, I-V data were acquired as a function of temperature. For compactness, we present two typical sets of curves corresponding to diodes CP 102 and CP 116 in Fig. 4.13 and Fig. 4.14.

In general, for diodes where the films are deposited at low T_s (typically less than 540°C), the two-exponential nature of the I-V curve is clearly visible (Regions 1 and 2 in Fig. 4.13) at low measurement temperatures (T_m). However, diode #116 (T_s = 620°C) shows a one-component behaviour at all temperatures studied as illustrated in Fig. 4.14. It is interesting to note that for diode #102, the dual slope nature of the curves reduces to a single component behaviour as the measurement temperature is raised (Fig. 4.13). The two marked regions also reveal a bias dependence whereby the smaller slope manifests itself at lower applied voltages. The experimental data for diode CP 116 obtained at temperatures of -49°C and - 15°C show some qualitative difference from its behaviour above room temperature.

4.3.3 Analysis and Discussion

In region 1 of Fig. 4.13, the slope of the curves at various measurement temperatures is fairly constant. This result is in favour of a temperature independent transport mechanism such as,

$$J_1 = J_{01} \exp(BV), \tag{4.1}$$

where B is a temperature independent constant. When the data is analyzed using this relation, the pre-exponential factor J_{01} shows a temperature dependence as shown in Fig. 4.15 and yields a

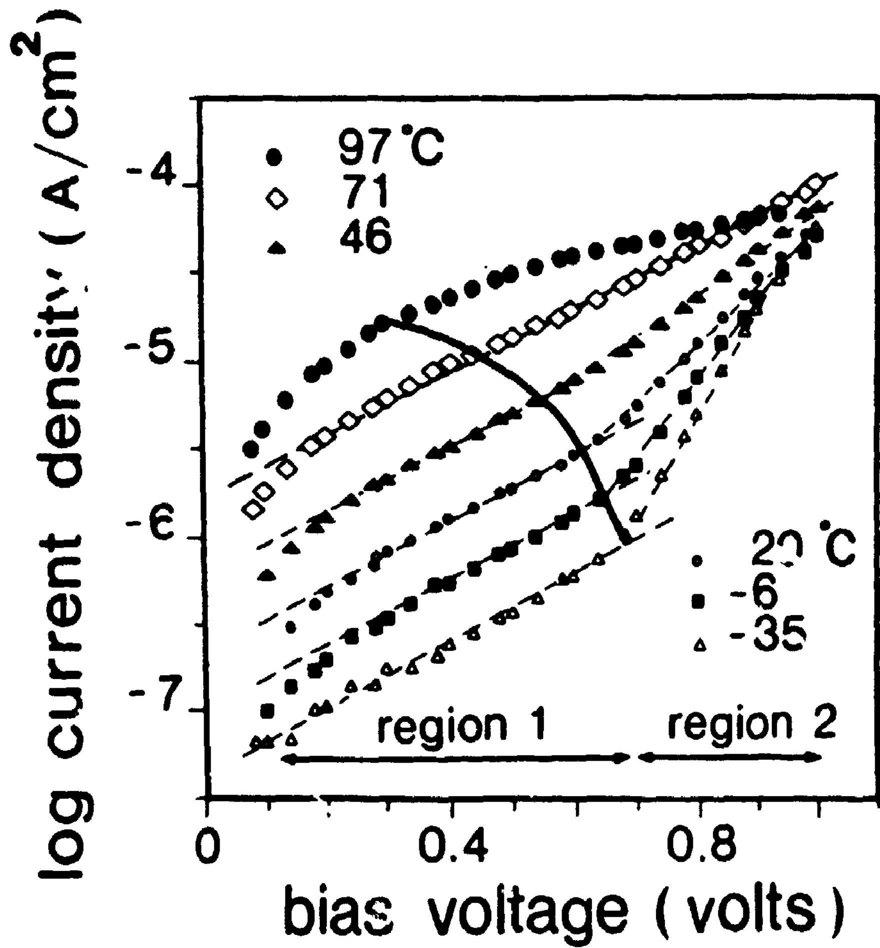

Fig. 4.13. Forward dark I-V characteristics of diode CP 102 measured at different temperatures. Dual slope features are marked (Regionsl and 2) for each curve. Notice that the transition point between region 1 and 2 shifts towards lower bias voltage (solid line) and finally, disappears completely as measurement temperature (T_m) is raised.

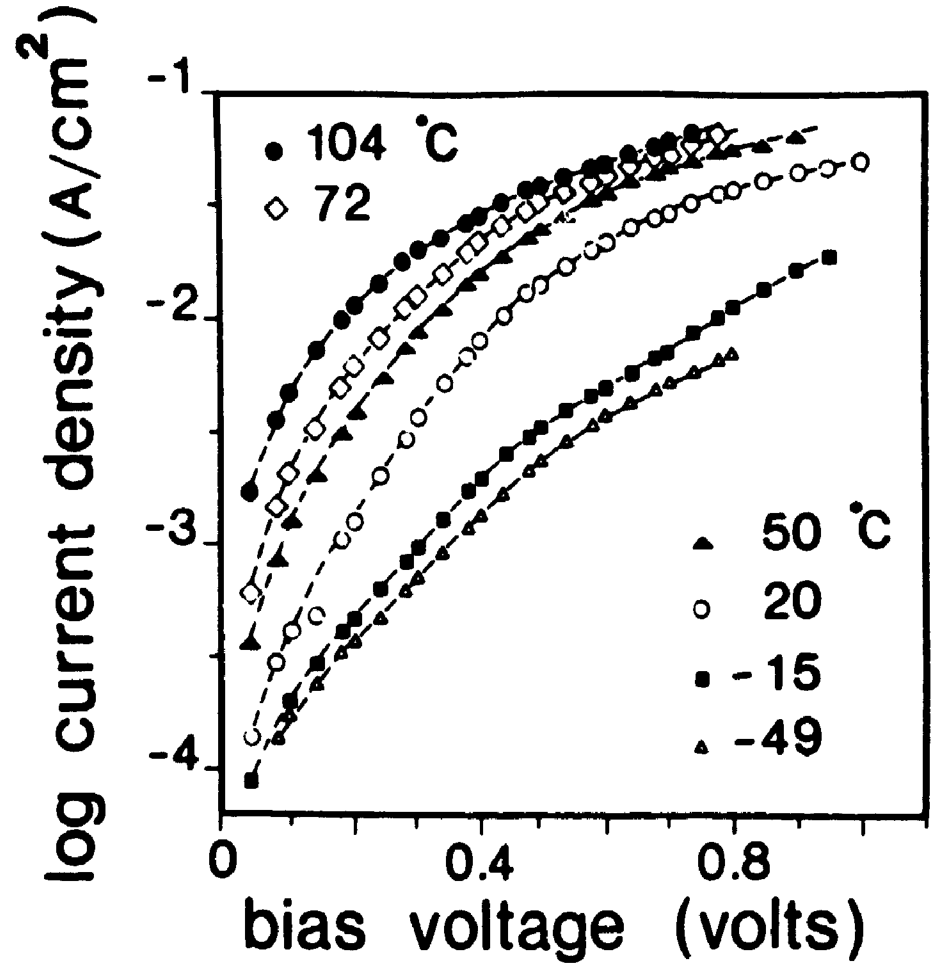

Fig. 4.14. Forward dark I-V characteristics of diode CP 116 at different temperatures.

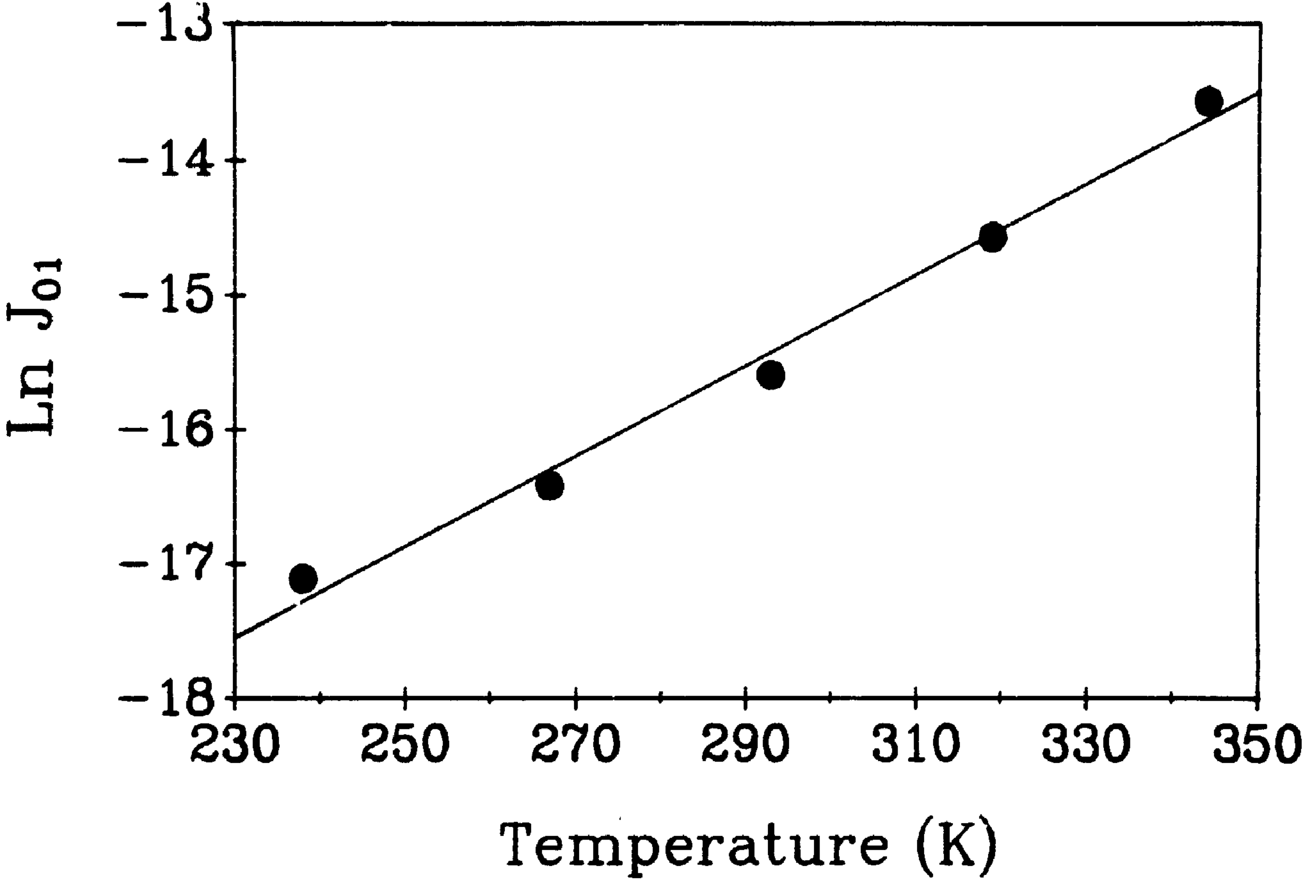

Fig. 4.15. Variation of J_{01} as a function of measurement temperature for diode CP 102.

relationship such as,

$$J_{01} = J_0 \exp(\alpha T) \qquad (4.2)$$

where $\alpha = 0.03\ K^{-1}$ and $\ln J_0 = -25.31\ A/cm^2$.

Exponential variation of J_{01} with temperature in the low temperature region and at low bias voltages is known to be associated with a tunneling effect (S.M. Sze, 1981). The behaviour of other diodes in the first region is similar to that of #102 but with varying magnitudes of J_0 and α, and consequently we assign a similar type of current transport mechanism.

One encounters some difficulty in trying to extract detailed information in the second region; it is clearly a temperature dependent process operating here. Such an analysis has been attempted (W.A. Miller and L.C. Olsen, 1984) with a fair amount of success on Cd(Zn)S/$CuInSe_2$ system using a curve-fitting approach. We conjectured, from the manner in which the two-exponential nature of the curves (in Fig. 4.13) gradually transforms into a one-slope behaviour, that a single mode of current transport dominates at higher temperatures. The transition point at which the slope changes shifts to lower bias voltages as the measurement temperature (T_m) is increased. This is shown in Fig. 4.13 by a solid line curving to the left. At 97°C, the curve resembles that of diode CP 116. Now, if this curve is analyzed using a relationship such as

$$J_2 = J_{02} \exp\left[(V-RI)/nkT\right] \qquad (4.3)$$

it yields a value of n = 1.91. Here V is the applied voltage and

R is the series resistance. Deviations of n from unity are usually ascribed to the presence of insulating layers and interface states, and to excess currents that flow due to recombination, tunneling, etc. (S.M. Sze, 1981). An n value around 2 is known to be due to electron-hole recombination through localized states at the interface. We can transform Eq. (4.3) into an ordinary differential equation of the type,

$$\frac{dy}{dV} = \frac{1}{(nkT/\log e + R\ 10^{y}\ \ln 10)} \qquad (4.4)$$

where y = log I, I is the current.

If one solves Eq. (4.4) numerically, the results are obtained as in Fig. 4.16. Curves 1, 2 and 3 are plotted (with n = 2, T = 300 K and $I_o = 10^{-5}$ A) for R = 0, 200 and 400 ohms, respectively. The I-V curve deviates from a straight line (R = 0) as the series resistance increases. Curve 4 is the simulated I - V curve at higher temperature T = 330 K (R = 170 ohm, $I_o = 10^{-4}$ A). The smaller slope observed in the experimental curves in region 2 at high measurement temperature can be understood as a consequence of the increase in value of the term IR (Eq. (4.3)) with temperature.

I-V curves of diode #116 in Fig. 4.14 were also analyzed on the assumption that a similar mechanism was operative. The resulting values of diode factor n are listed in Table 4.2. n has a nearly constant value of 2 except at -49°C where a discrepancy

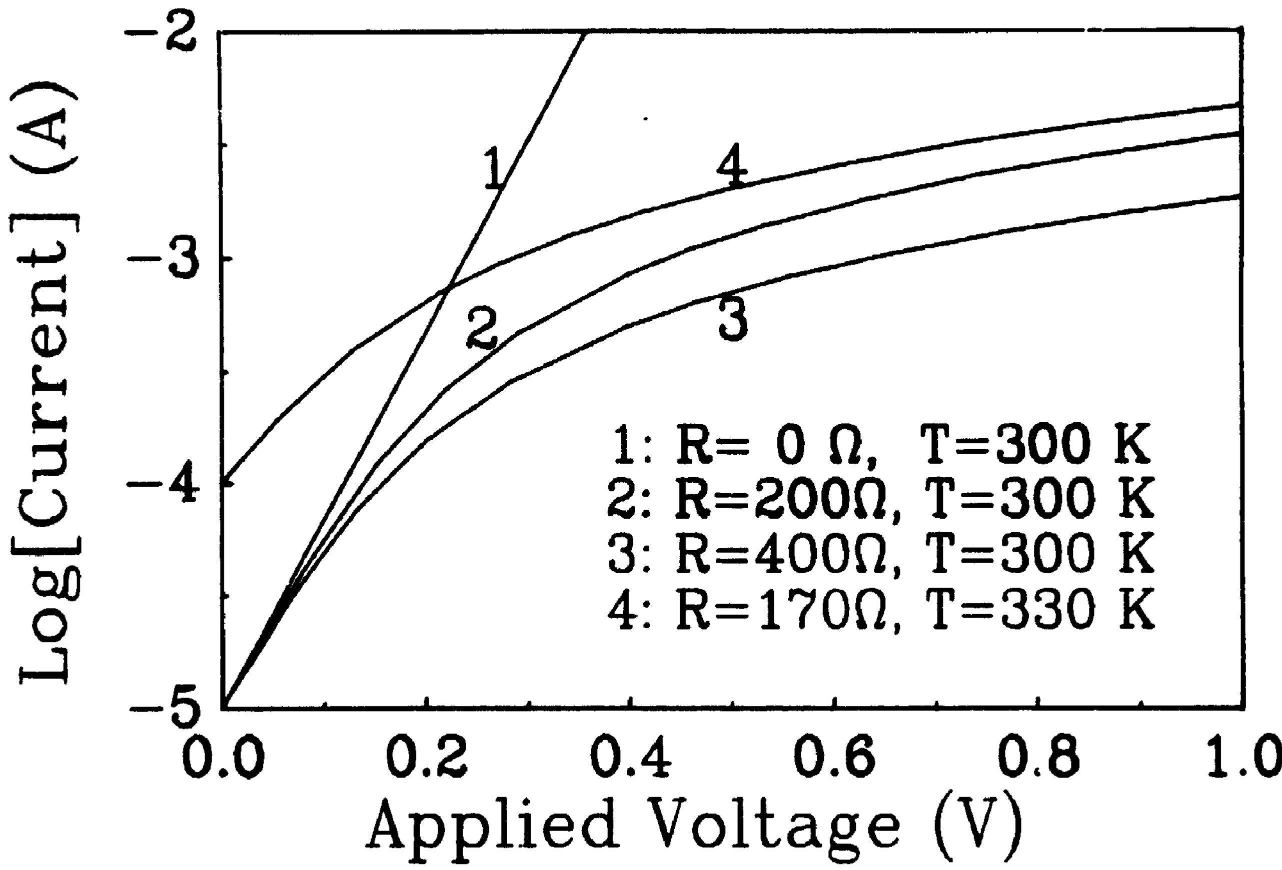

Fig. 4.16. Simulated I-V curves using eqn (4). See text.

Table 4.2.

Diode factor for diode CP 116

T (^{o}C)	n
-49	4.38
-15	2.06
20	2.11
50	1.99
72	2.08
104	1.37

is observed. The anomaly at low temperature could not be verified due to lack of additional I-V data. An exponential variation of J_{02} with 1/T is observed confirming the role of recombination process. This is plotted in Fig. 4.17 which gives an activation energy of 0.4 eV.

Experimental evidence for the dual-slope behaviour at low temperatures and their disappearance at higher temperature was reported by Yu and Wang (L.S. Yu and C.D. Wang, 1983) in the I-V characteristics of p-GaAs/n-$A\ell_xGa_{1-x}As$ (x = 0.25) crystalline heterojunction LED's. The I-V data were expressed as a sum of low-voltage, tunneling current through interface states in the barrier and the usual injection current over the barrier by thermalemission at higher voltages. The transition in slope was observed to be between 1 and 1.5 volts. There has also been a previous attempt to analyze the current-voltage characteristics of Cd(Zn)S/$CuInSe_2$ heterojunction solar cells by integrating the observed behaviour using a tunneling-interface recombination model (W.A. Miller and L.C. Olsen, 1984), in which it was assumed that tunneling and recombination processes act in series. In hydrogenated amorphous silicon Schottky barrier diodes, the occurrence of dual mechanism of transport was previously reported by Madan and co-workers (A. Madan et al., 1982) where a voltage induced transition from one mode of transport to another at fixed temperature was observed. The values of n obtained by assuming the simple diffusion/drift and recombination model were found to increase with phosphorus concentration and a second channel for the current flow via an impurity band 0.3 eV below the conduction

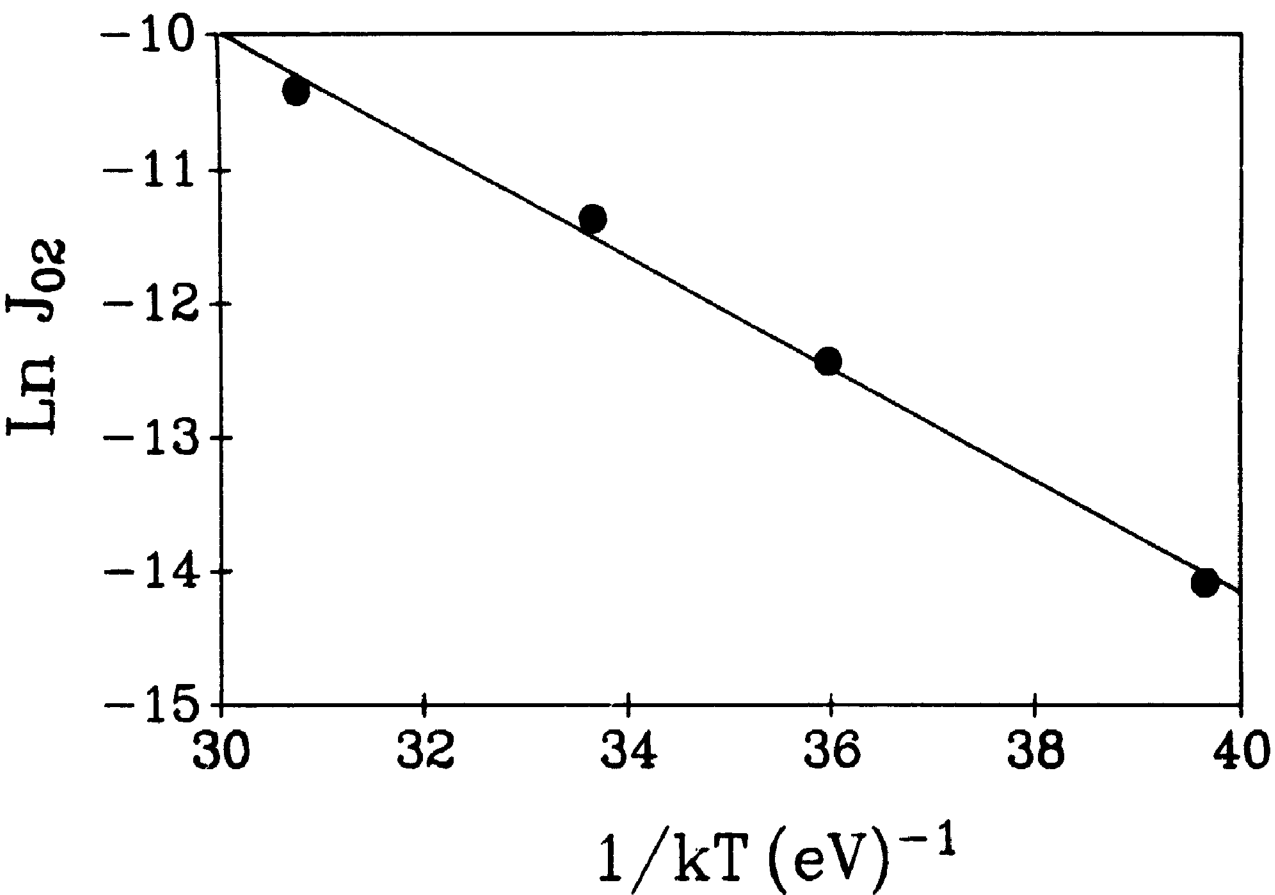

Fig. 4.17. Variation of J_{02} as a function of 1/kT for diode CP 116.

band was postulated. Hopping currents dominated at high dopant concentrations. In the study of I-V characteristics of glow-discharge produced undoped hydrogenated amorphous silicon heterojunctions on p-crystalline silicon substrates (H. Matsuura et al., 1984), there was no indication of a dual transport mechanism, but the forward currents of all junctions showed a voltage and temperature dependence as $\exp\left[-\frac{\Delta E_{af}}{kT}\right]\exp(AV)$, where ΔE_{af} and A are constants independent of voltage and temperature. These results were explained by a multi-tunneling capture-emission model. However, data showed that the pre-exponential factor J_o varied exponentially with $-1/T$ rather than T as expected for the tunneling process.

Changes in the I-V curves of our diodes are closely associated with the observed transition in conduction mechanisms due to the changes in the network structure of the LPCVD a-Si films. The temperature dependence of conductivity in as-deposited amorphous films is generally described by (see chapter 2):

$$\sigma = \sigma_{01}\exp\left[-E_1/kT\right] + \sigma_{02}\exp\left[-E_2/kT\right]$$

where the first term denotes extended state conduction and the second represents localized state, phonon-assisted hopping conduction. In the typical σ vs $1/T$ plot illustrated in Fig. 4.18 for lightly doped n-type films deposited at different substrate temperatures, the low and high temperature regimes are clearly distinguished by two different slopes. The low temperature regime

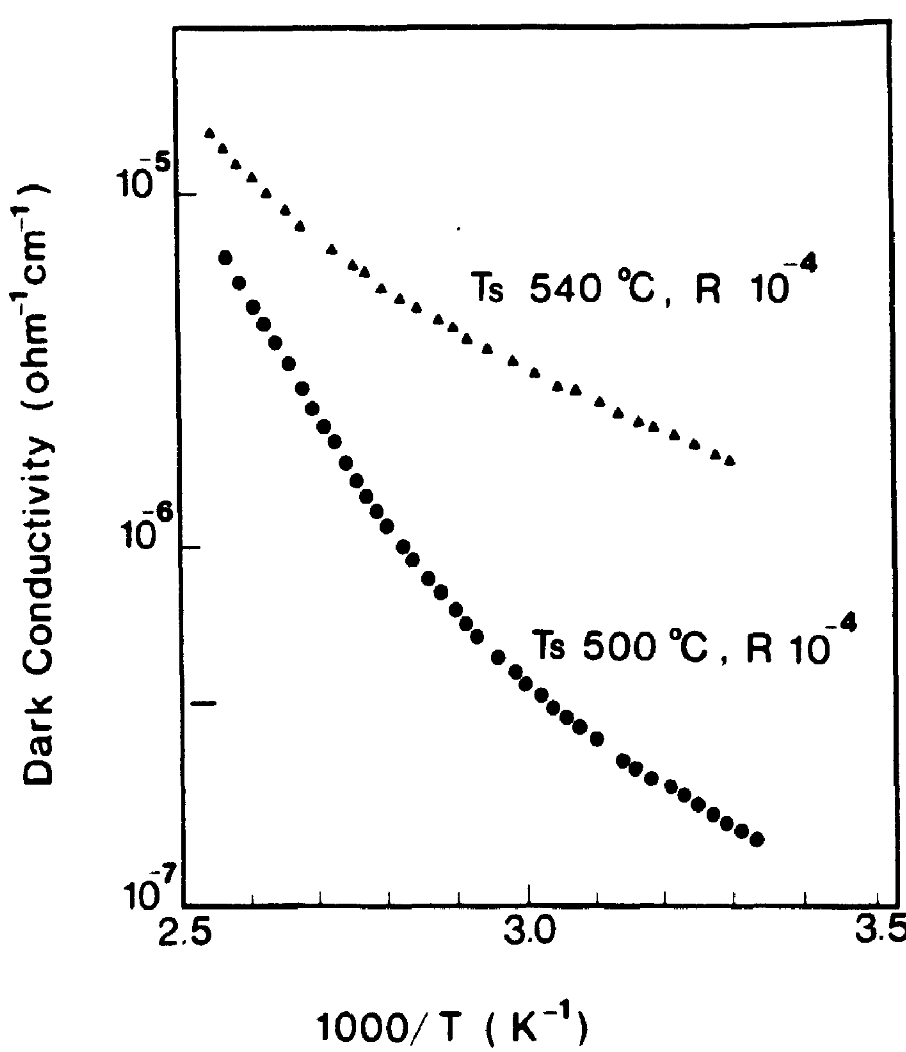

Fig. 4.18. Temperature dependence of conductivity of phosphorus doped amorphous silicon films.

in the curve can be treated as the hopping current component whereas above room temperature, conductivity is an activated process leading to extended state conduction. Activation energies of E_1 = 0.63 and 0.41 eV were calculated for films deposited at T_S = 500 and 540°C, respectively. The transition occurs near about the same temperature as observed in I-V curves of CP 102 in Fig. 4.13 where the two linear portions of the curve merge into one. This might indicate that hopping conduction is closely associated with the tunneling process in the heterojunction while extended state conduction corresponds to the recombination process.

In films deposited at $T_S \geq 580°C$, the activation energy E_1 is significantly reduced. Amorphous-microcrystalline transition occurs at about this temperature. The one-slope behaviour in the I-V curves of diode #116 (T_S = 620°C) can be understood as a consequence of the above transition.

At low deposition and measurement temperatures, it is reasonable to expect a tunneling/hopping mode of current transport to be dominant. The various current transport mechanisms are sketched in Fig. 4.19. The phosphorus concentration in the films was determined to be of the order of 10^{20} atoms/cm^3. If one allows a large discontinuity in the conduction band for n-a:Si/p-c:Si heterostructures (K. Ueda et al., 1988), then transport occurs mainly by tunneling through an impurity band across the barrier. As the forward bias increases, it reduces the field in the space charge region, lowers the barrier and more electrons can climb the barrier than can tunnel through it. Also

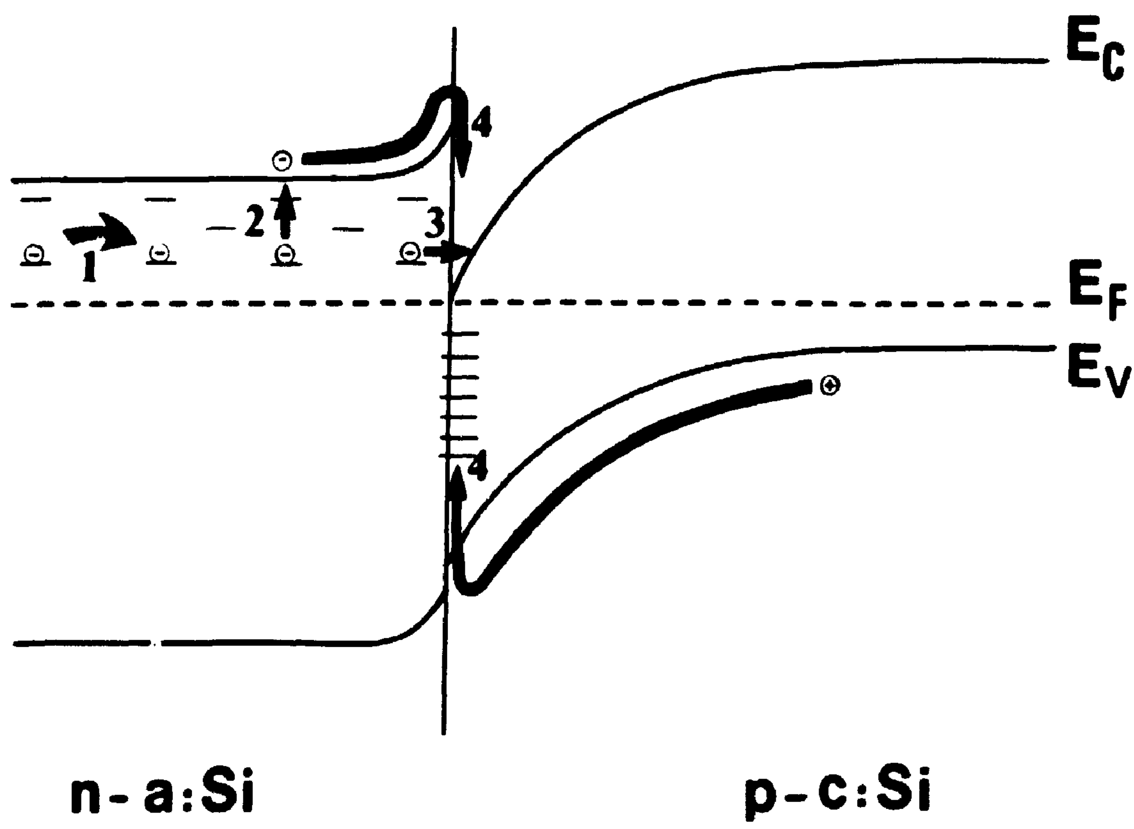

Fig. 4.19. Schematic diagram showing current transport mechanisms in n-a:Si/p-c:Si heterojunction. (1) hopping, (2) thermal excitation, (3) tunneling and (4) recombination.

at higher temperatures, more electrons are excited to the conduction band. One would, in these cases, expect to see a transition from tunneling to drift- recombination mode which is indeed observed in the I-V curves.

It is generally accepted that presence of hydrogen in the material can terminate the dangling bonds and consequently reduce the density of states in the bandgap. To understand the role of hydrogen in modifying the transport properties of LPCVD a-Si films, we performed post-hydrogenation experiments on lightly doped a-Si films as well as on n-a:Si/p-c:Si diodes. The samples were hydrogenated using an atom gun with a beam current density of 100 $\mu A/cm^2$ which is equivalent to a dose of 6×10^{14} atoms/(s.cm^2) and a variable beam energy of 5-8 keV. Specimens were heated to 400°C during the procedure. This was expected not to cause any instability, since our films are deposited above 500°C. Exposure times were less than 10 minutes.

An enhancement of conductivity is observed in the hydrogenated amorphous films accompanied by a decrease in activation energy, to 0.56 and 0.25 eV for films deposited at T_s = 500 and 540°C respectively. This indicates a reduction of density of states in the gap and consequent shift in the Fermi level. Results of the post-hydrogenation process on diodes #122 and #116 reveal that the dual slope I-V curve of diode #122 reduces to a one-slope profile after hydrogenation. This is analogous to the characteristic features in diodes where the films are deposited at high temperature (T_s) or when the I-V data are

acquired at relatively high temperature (T_m). Diode #116 shows similar features before and after hydrogenation as one would expect with relatively low density of states in a LPCVD microcrystalline material. Results of hydrogenation experiments on LPCVD Si films have been previously reported (P.X. Zhang et al., 1987).

The heterojunctions show promising solar cell characteristics when fabricated at high temperatures (T_s = 580 - 620°C) and doping ratios (R = 4 x 10^{-3} - 1 x 10^{-2}). This is illustrated by the illuminated I-V curves shown in Fig. 4.20 and Fig. 4.21.

When films are deposited at low T_s (500°C for #122), the short circuit current (I_{sc}) deteriorates (Fig. 4.20). This is consistent with the view that poor junction performance is strongly related to hopping conduction mechanisms due to electron localization and defects in the amorphous material. Open circuit voltage (V_{oc}) is more severely affected by changes in dopant concentration in the silicon films. The overall cell rating (I_{sc}, V_{oc} and fill factor) improves when doping ratio increases and reaches an optimum value at R = 4 x 10^{-3} (#154 in Fig. 4.21). The highest V_{oc} and I_{sc} achieved under these conditions are 0.55 V and 5.45 mA, respectively yielding a photovoltaic conversion efficiency of 9% (active area 0.16 cm^2 at a light intensity of 100 mW/cm^2).

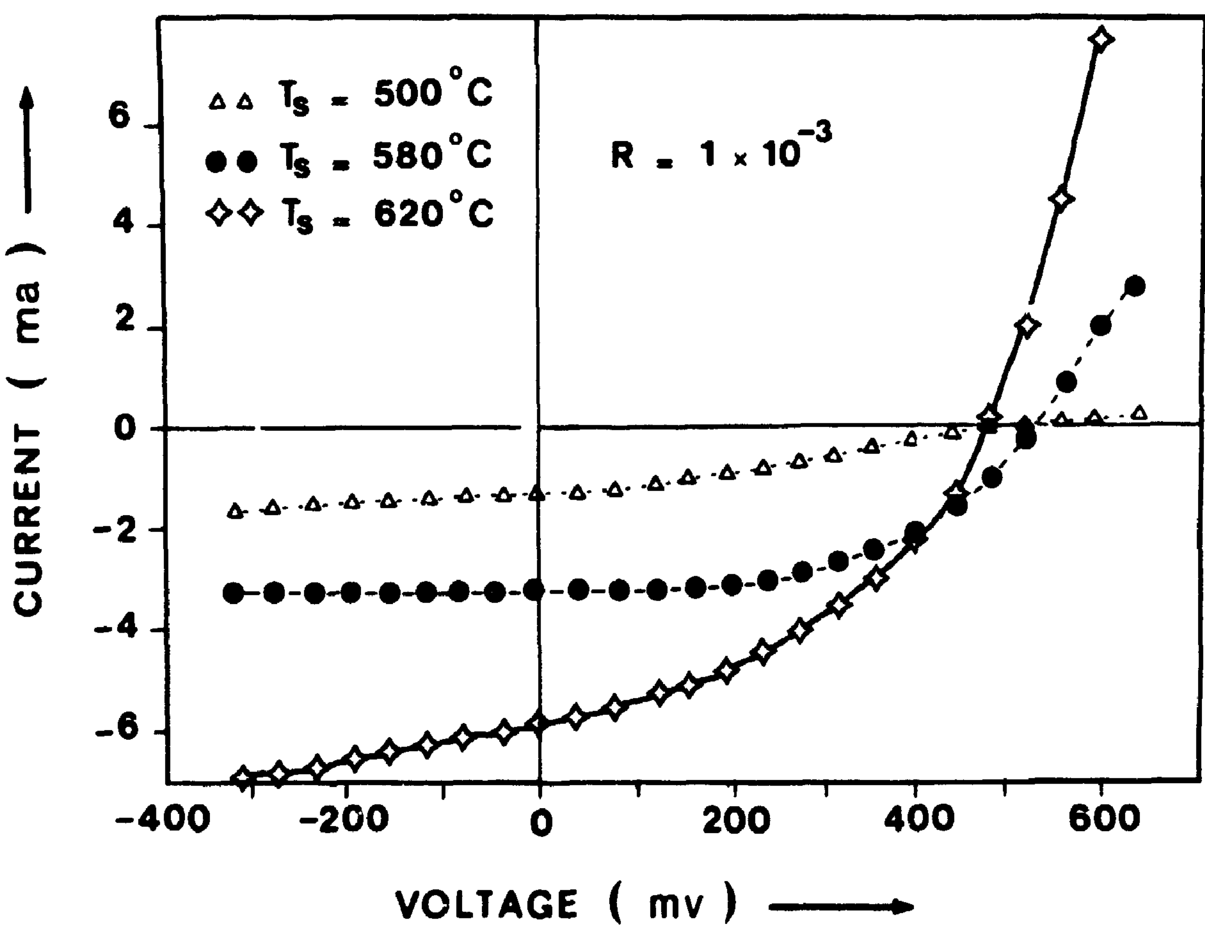

Fig. 4.20. Illuminated I-V characteristics of n-a,μc:Si/p-c:Si solar cell devices fabricated from Si films deposited at various substrate temperatures: △ CP 122, ● CP 163, ◇ CP 116.

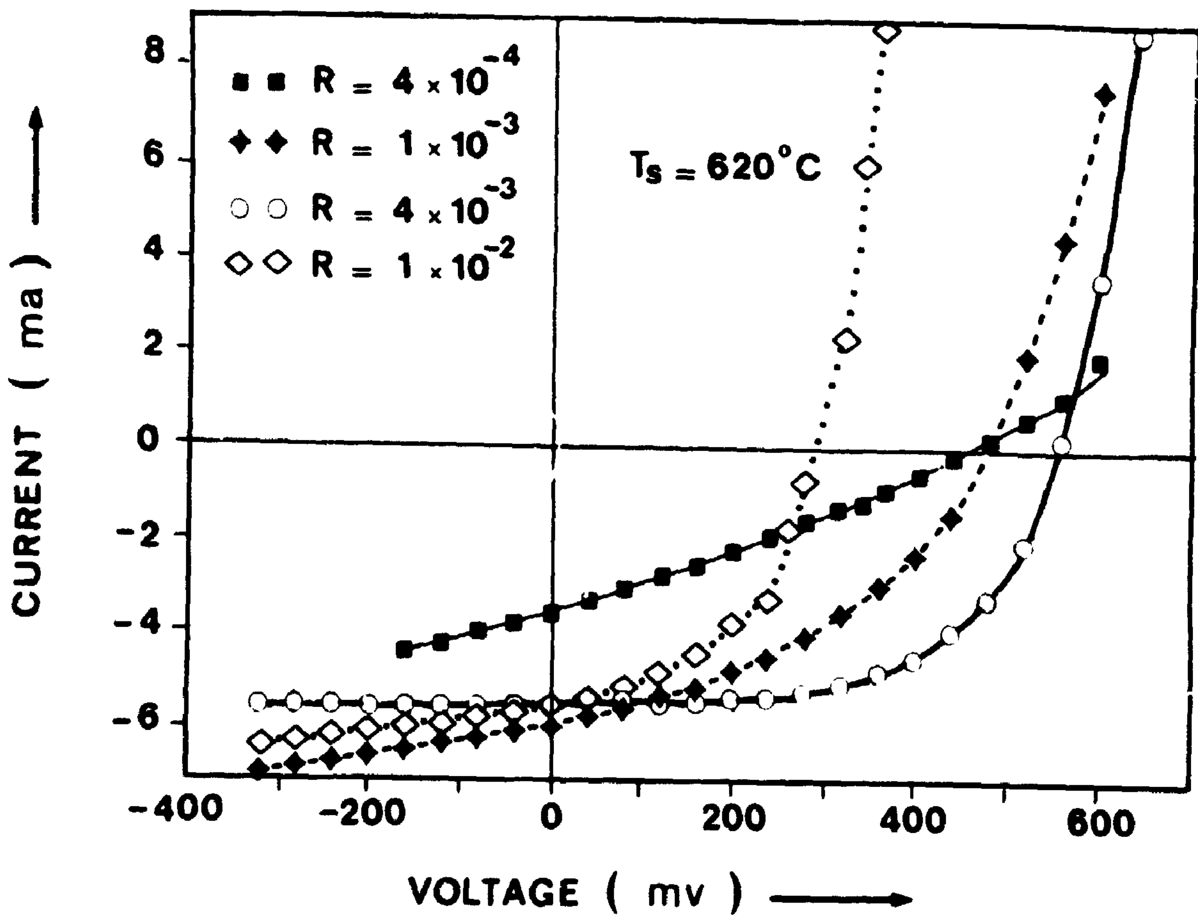

Fig. 4.21. Illuminated I-V characteristics of n-a,μc:Si/p-c:Si solar cell devices fabricated from Si films deposited at various gas ratios: ■ CP 164, ◆ CP 116, O CP 154, ◇ CP 148.

4.4 Conclusions

In this chapter, we studied various aspects of LPCVD Si films through a variety of methods all of which indicate, that in our fabrication condition range, both a-Si and μc-Si can be obtained. A-Si and μc-Si have different properties from each other and behave differently in devices. Based on those data, we classify our material and identify the transition boundary in Fig. 4.22 (P doped films) and Fig. 4.23 (B doped films). In the case of B doped samples, we define amorphous material with more than 5% B atoms as amorphous alloy. With the knowledge gained so far, we will begin an even more difficult and challenging experiment in the next chapter: Hall effect of a-Si. We will show that a-Si could have normal Hall coefficient.

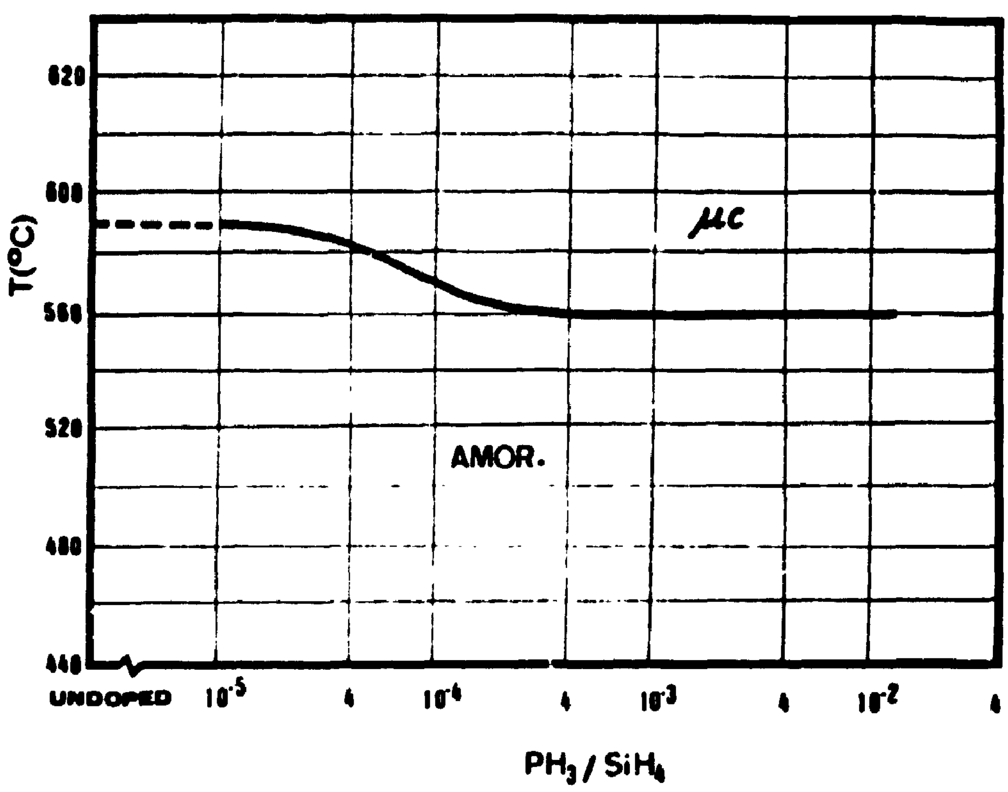

Fig. 4.22. Zones of different phosphorus doped LPCVD-Si material: amorphous (AMOR.), and microcrystalline (μc).

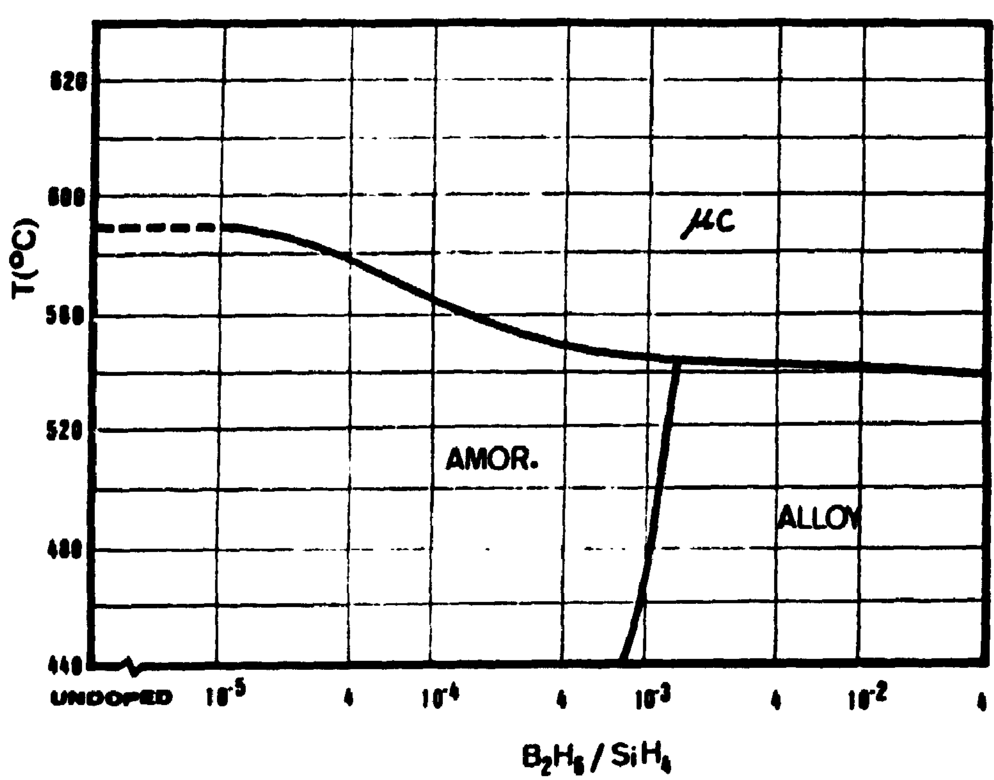

Fig. 4.23. Zones of different boron doped LPCVD-Si material: amorphous (AMOR.), amorphous alloy (ALLOY) and microcrystalline (μc).

Chapter 5 Hall Effect*

The Hall effect of amorphous semiconductors is a fascinating subject and yet the least studied and understood of transport properties of the material. Extremely small Hall signal and high resistivity of the sample are, among other things, the difficulties one encounters in this experiment. Early Hall measurements were concentrated on chalcogenide glasses (See reviews by Rollos, 1978 and Fritzsche, 1974). Measurements on amorphous Si:H thin films fabricated by glow discharge method have been made and reported by the Dundee group (LeComber, Jones and Spear, 1977), the Marburg group (Beyer, Fischer and Overhof, 1979, Overhof, 1981), and by Dresner (Dresner, 1980). In general,the magnitude of Hall mobility is very small(between 10^{-2} to 10^{-1} $cm^2/V.s.$) and increase slightly with temperature. More interestingly, all the studies mentioned above reported the "anomalous Hall effect": in the case of a-Si thin films, the sign of Hall coefficient of both phosphorus and boron doped films are opposite to that of thermoelectric power. So far, no systematic measurements on LPCVD (Low Pressure Chemical Vapour Deposition) a-Si thin films have been reported. At U.W.O., we have started a

---

* *Parts of this chapter have been published in:*
1) *J. Non-Cryst. Solids,* **114**, *369(1989) and*
2) *Phys. Rev. B, Rapid Communication,* **41**, *1251(1989).*

research program to study the Hall effect of a-Si thin films fabricated by LPCVD method and observed, for the first time, a normal Hall coefficient in some good structured amorphous LPCVD samples.

5.1 Experimental Considerations

The electron transport in a-Si is mainly through hopping conduction. The samples are thus expected to have high resistivity and small Hall voltage signals. From experimental point of view, when measuring Hall effect in amorphous semiconductors, some difficulties arise that are not usually encountered in crystalline semiconductors. Because of those difficulties, the task of measuring Hall effect of a-Si becomes a very challenging one. It requires careful consideration and good experimental design in order to obtain reliable Hall signals. For example, Hall measurement by alternating current (A.C.) source is not considered suitable for a-Si. D.C. Hall effect is therefore the only approach one can use in studying a-Si. The inability of using A.C. current source in Hall effect measurement is distressing because many standard small signal processing techniques (such as lock-in amplifier) do require A.C. signal input (A.C. Hall measurement has been attempted by R.S. Klein in the range of impurity hopping conduction on p-type crystal Ge samples. The Hall signal was not detected in their detection limit. R.S. Klein, 1985). In the following, we briefly summarize the difficulties and possible measures one may employ in order to neutralize or reduce the problems.

1) Problem: The value of μ_H is small. Reported values have ranged from $5x10^{-3}$ to 0.5 cm^2/V s. For a typical value of $\mu_H = 1x10^{-2}$ cm^2/V s, the Hall voltage will be on the order of 10 μV.

Solutions: Increase the sensitivity of the data acquisition system by reducing the misalignment voltage (see Fig.5.3. When a current passes through a Hall sample from E to F, there will be a voltage drop between the two Hall probes A and C or B and D. It is called misalignment voltage.). This can be accomplished by reducing the sample size and improving sample patterning through lithography. Increase signal/noise ratio by rotating the magnet (change the direction of B) to get a reading of $2V_H$ instead of V_H , by increasing current and by reducing the noise level through improved shielding and grounding.

2) Problem: The noise level of Hall voltage is often high, particularly when the current contacts to the sample are not ohmic and the samples are not homogeneous.

Solutions: Improve the electrode contacts by using suitable metal contact and substrate temperature during evaporation. Annealing can also be used for this purpose. Improve the shielding and grounding of the measurement system.

3) Problem: The resistance of amorphous sample could be high because the samples usually are thin (few thousand angstroms).The capacitance of the measuring circuits must be taken into consideration.

Solutions: Use smaller sample to reduce the resistance. Due to

the time constant of the circuit, when measuring Hall voltage, it is important to wait until the signal becomes stabilized.

4) Problem: The thermoelectric power for a-Si is in the range of 100 - 1000 $\mu V/K$ for doped material. Therefore small temperature gradients can cause signals much larger than the Hall voltage.

Solutions: Use smaller samples. Use good heat conductor such as copper for sample holders. Improve the sample heating and cooling systems.

5) Problem: The large density of deep states in amorphous material can act as electron and hole traps. It may take as long as 8 hours to relax and stabilize sufficiently the potential at the Hall electrodes after changing the temperature or reversing the current direction (Dresner, 1984).

Solutions: Use good D.C. current source. When measuring Hall voltage, it is important to wait until the signal becomes stabilized.

6) Problem: Inhomogeneities in the structure or in the electrical properties can cause a magnetoresistance effect, resulting in signals that do not reverse with the direction of the magnetic field. This signal can be much larger than the Hall voltage.

Solutions: Improve the deposition process. Use as small a sample as possible.

5.2 Experimental Setups

The a-Si thin films for Hall effect study were deposited onto Corning 7059 glass substrate by an LPCVD system which has been described in chapter 3. The following conditions were used for

film fabrication: substrate temperature T_S from 460 °C to 620 °C and phosphine/silane (or diborane/silane) ratio from 1×10^{-5} to 1×10^{-2}. In this fabrication condition range, both amorphous and microcrystalline materials can be obtained. In chapter 4, we identified the transition temperature from a-Si to μc-Si for both P or B doped Si films.

For Hall effect measurement, systematic approaches taking account of all the considerations mentioned in § 5.1 must be adopted in order to obtain reliable results. From experimental point of view. those approaches can be divided into three categories: measurement system design, Hall sample preparation and measurement procedures. In the following, we discuss those three aspects separately.

5.2.1 Measurement System Design

The Hall measurement system consists of a rotatable magnet (Varian V-3400) capable of producing a magnetic field of 0 to 1.5 T, a stainless steel sample chamber with vacuum pump and a data acquisition and processing system. The complete system is illustrated in Fig. 5.1. The sample holder (see Fig. 5.2) is made of solid copper with tunnels inside the block for the circulation of liquid nitrogen. A heater is also incorporated into the holder so the temperature of the Hall sample can be varied. The entire system has to be shielded and grounded very carefully in order to reduce the interference of outside electrical noises.

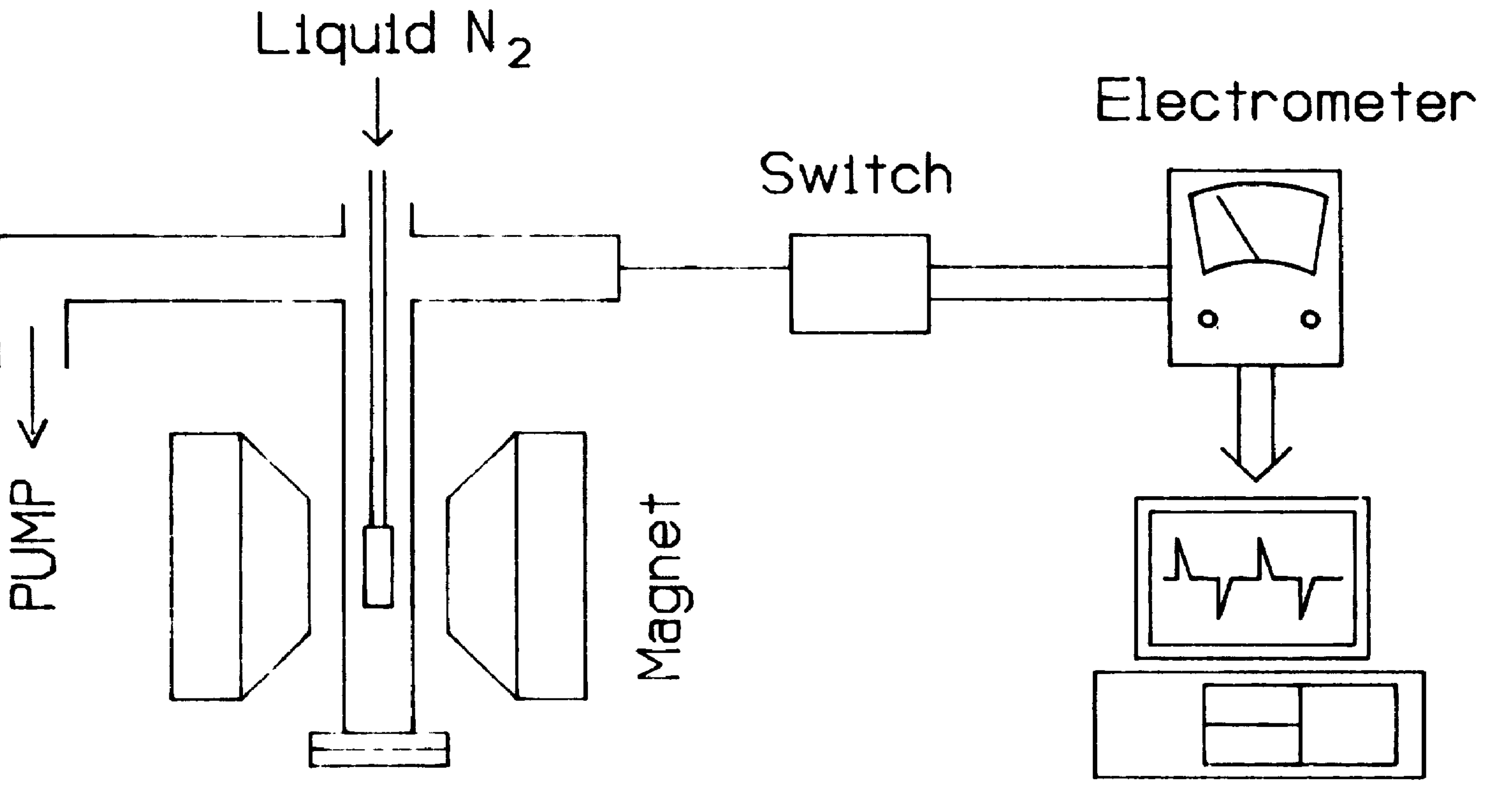

Fig. 5.1. Hall effect measurement system.

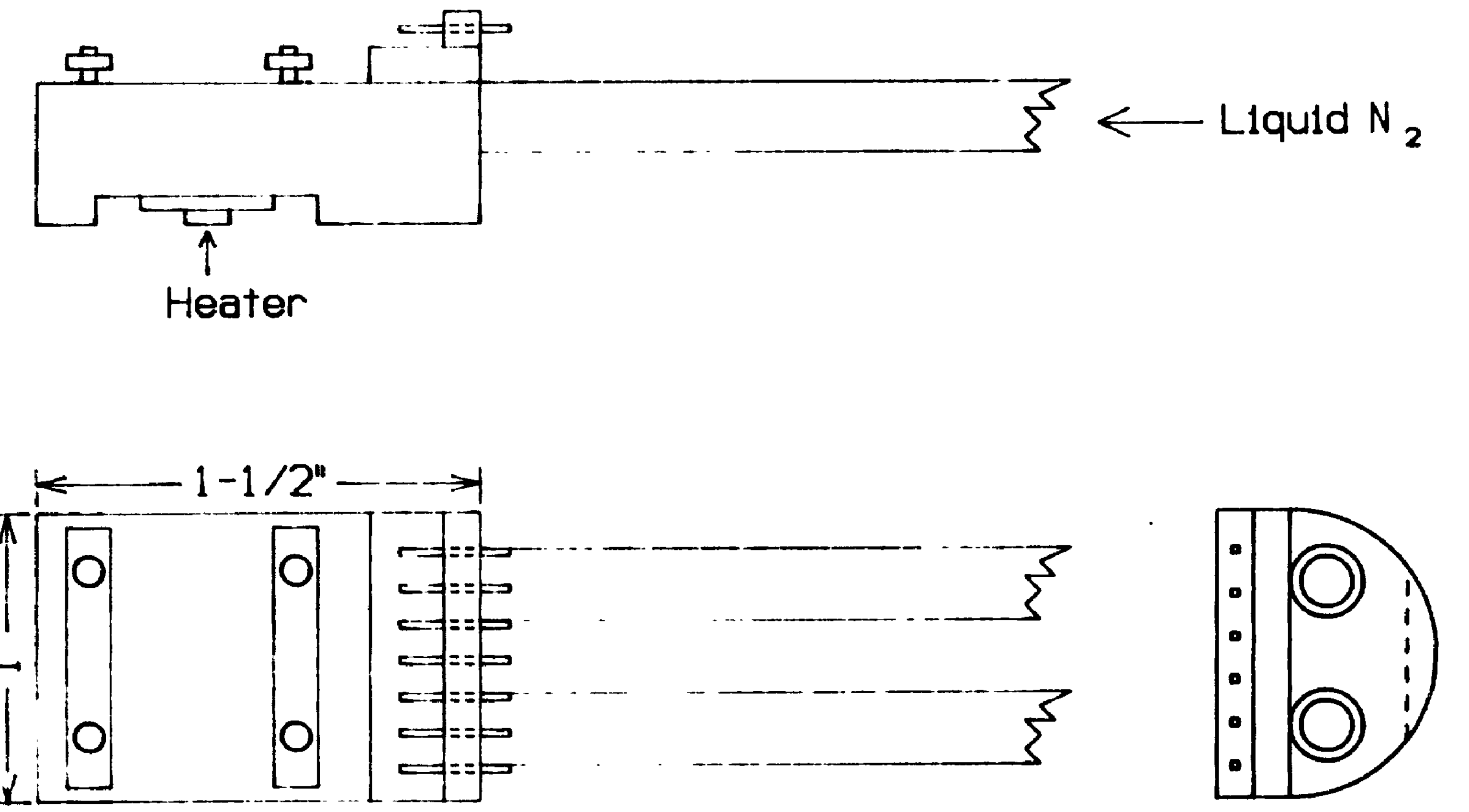

Fig. 5.2. Sample holder for Hall measurement.

5.2.2 Hall Sample Preparation

The Hall samples are designed to be as small as can be easily handled in order to compensate the possible inhomogeneity of the films and reduce the misalignment voltage (Fig. 5.3). Misalignment voltage is the "base" voltage level between Hall probe A and C or B and D when a current is passing through the Hall sample from E to F. Ideally, it should be zero. Since Hall voltage is proportional to the current through the sample, it is natural to increase the applied voltage V_{EF} in order to enhance the Hall signal. In our system for example, we use a 147 V battery as our Hall current source. With this magnitude of applied voltage, misalignment voltage can be easily in the range of 1 V. If this happens, it will severely affect the ability to detect the Hall signal because one has to use 1 V range of the electrometer to detect a signal on the order of 10 μV. Thus the first major concern in designing Hall sample is to reduce the misalignment voltage. Misalignment voltage basically comes from two sources: the mismatch of the Hall probes and inhomogeneity of the samples; both can be circumvented considerably by using as small Hall sample as possible. While reducing the sample size will certainly improve the situation, too small a sample will introduce operational problems. For example, small samples are more difficult to connect to external measurement circuits because 6 electrodes have to be connected to the sample by soldering. The suitable sample size should be a compromise of these considerations. In our experiment, the dimension of the sample is 0.9525mm x 3.175mm. The sample pattern was realized by lithography

to ensure better alignment of the probes. The sample pattern is shown in Fig. 5.3. The shaded areas are the metal electrodes. Photo plate 1 is the Hall sample. Fig. 5.4 (a) is the mask for the a-Si Hall sample. The mask for metal electrodes is in Fig. 5.4 (b).

For the electrodes, evaporated Cr was used as the first layer to make contact with the silicon thin film and Au as second layer on top of Cr.* During the metal evaporation, the sample was kept at a temperature of 250 °C. The purpose of the Au layer is that indium solder can form alloy with Au layer easily and thus create an electrically good and mechanically strong contact with the external measurement circuits. Annealing process may also be used to reduce the contact noise. In our experiment, Cr and a-Si (p- or n-type) form a good Ohmic contact because: i) most Hall samples are highly doped, and ii) the voltage for the Hall measurements is very high, usually around 150 V. The sample was connected to the measurement circuits by indium solder. The sample chamber is made of stainless steel and operated under vacuum.

5.2.3 Measurement Procedures

For the sample pattern shown in Fig. 5.3, Hall mobility acquires a very simple expression:

---

* *J. Dresner (J. Dresner, 1980) used Cr for the electrodes and Le Comber et al. (P. G. Le Comber, D. I. Jones and W. E. Spear, 1976) used Gold film for their n-type a-Si and Al for the p-type.*

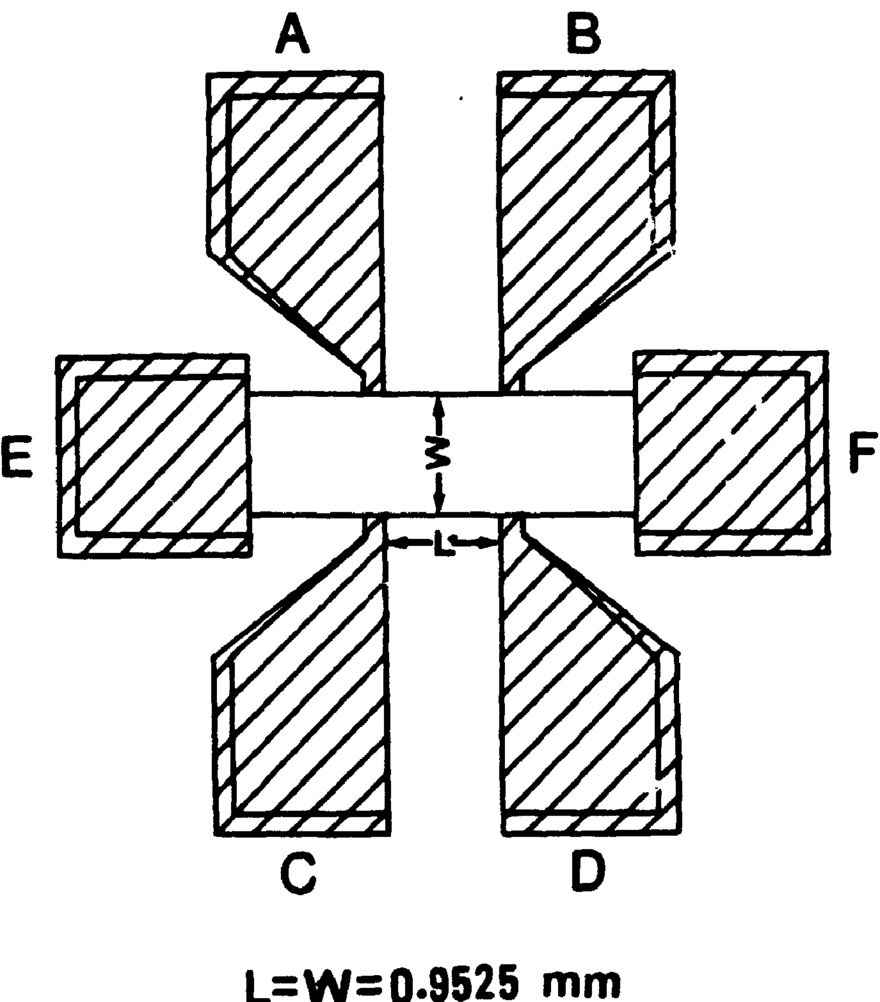

Fig. 5.3. Hall sample pattern diagram.

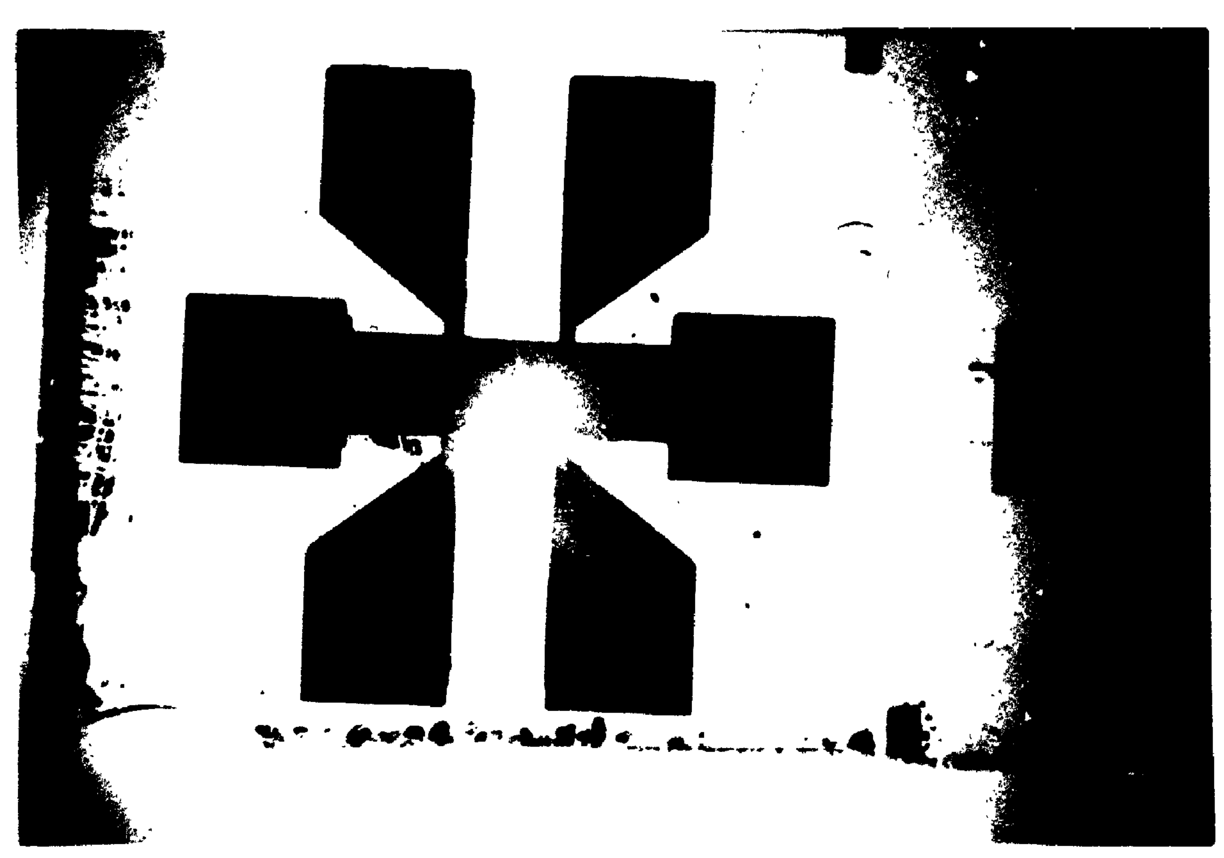

Plate 1. Photo of an actual Hall sample.

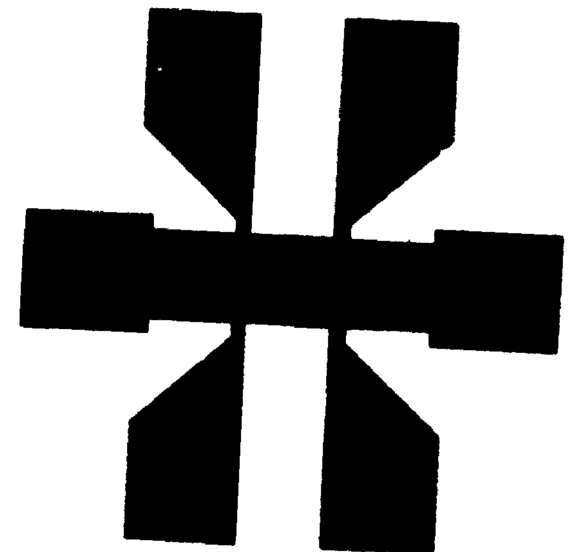

Fig. 5.4(a) The mask for the preparation of Hall samples.

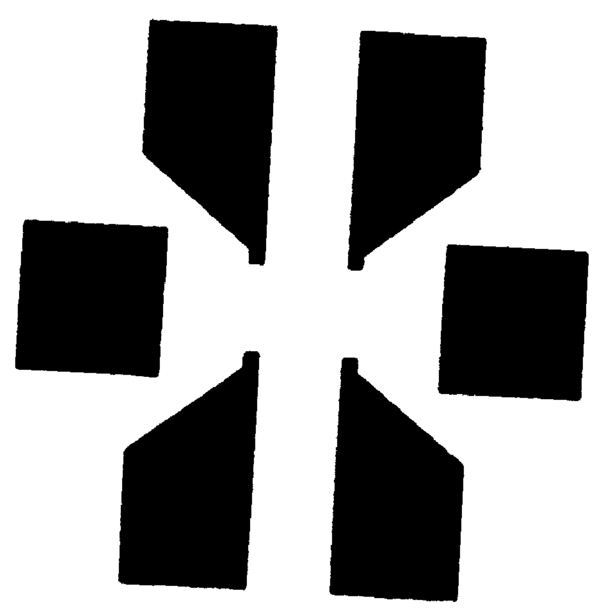

Fig. 5.4(b) The mask for the electrodes on Hall samples.

$$\mu_H = \frac{V_H}{V_{AB}} \frac{1}{B} \qquad (5.1)$$

where V_H is the Hall signal (can be measured from probes AC or BD) and V_{AB} (or V_{CD}) is the voltage drop across probes AB (or CD). B is the magnetic field. The μ_H in (5.1) has a unit of (m^2/ V sec) when B is in Tesla. We derive eq. (5.1) in the following: From experiment, Hall field is proportional to current density j and magnetic field B:

$$E_H = R_H \; j \; B \qquad (5.2)$$

$$\therefore \qquad V_H = R_H \; j \; B \; W \qquad (5.3)$$

R_H is the Hall coefficient and W is the sample width (see Fig. 5.3). The resistance of the sample has the form:

$$R = \frac{V_{AB}}{I} = \rho \frac{W}{T \; L} \qquad (5.4)$$

T is the sample thickness and L the sample length. ρ is resistivity.

$$\therefore \qquad \rho = \frac{V_{AB} \; T \; L}{I \; W} \qquad (5.5)$$

The Hall mobility μ_H is defined as:

$$\mu_H = \sigma \; R_H \qquad (5.6)$$

Combine Eq. (5.3), (5.5), (5.6) and noting that j = I/(W T), one

can obtain:

$$\mu_H = \frac{V_H}{V_{AB}} \frac{1}{B} \frac{L}{W} \qquad (5.7)$$

For our Hall sample shown in Fig. 5.3, L = W = 0.9525 mm, Eq. (5.7) then becomes:

$$\mu_H = \frac{V_H}{V_{AB}} \frac{1}{B} \qquad (5.8).$$

In the actual experiment, we use:

$$\mu_H = \frac{V_\perp}{V_\parallel} \frac{1}{B} \qquad (5.9)$$

to calculate the Hall mobility where

$$V_\perp = \frac{(V_H^{AC} + V_H^{BD})}{2} \qquad (5.10)$$

$$V_\parallel = \frac{(V_{AB} + V_{CD})}{2} \qquad (5.11)$$

Hall effect measurement of a-Si is a constant struggle with the extremely small Hall signal and the interference of external electrical noises. One effective way to increase measurement signal is to rotate the magnet (change direction of B) in order to obtain a reading of 2 V_H . Fig. 5.5 is a typical Hall effect measurement result for a-Si. The spikes in Fig. 5.5 immediately after the rotation of B is due to induced e.m.f.. The decaying

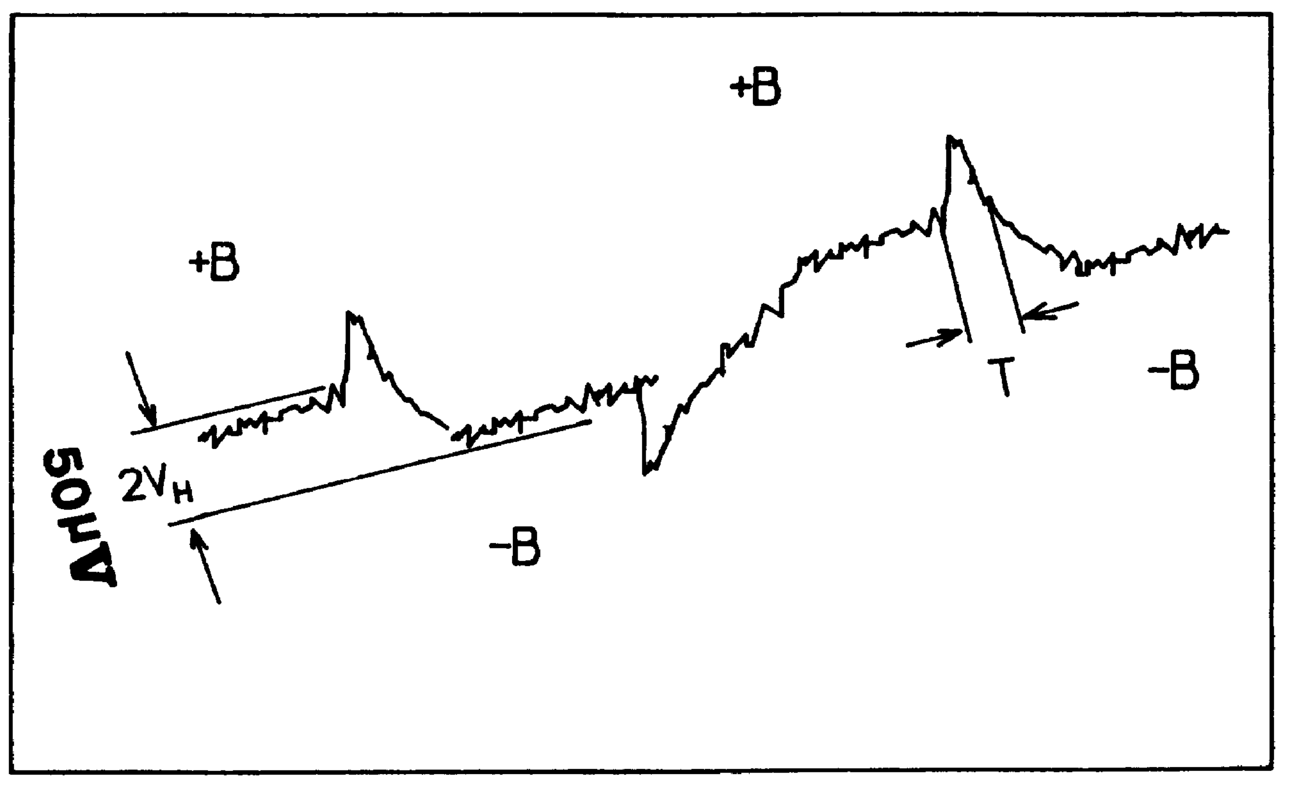

Fig. 5.5. A typical Hall signal from measurements.

time T is sample dependent; in most cases, it is in the range of several seconds to less than 1 min.

We begin the measurement by making sure that the signals we observe are indeed Hall signals. One can verify this by: 1) changing the direction of the current; 2) changing the direction of **B**; 3) changing the magnitude of **B**. If the response of V_H after those changes satisfies Eq. (5.3), the signal observed is then confirmed as Hall signal. This step is important and necessary because, in some instances, the polarity of observed voltage signal does not change as the direction of current or magnetic field is switched (K. Murase et al., 1983). The reasons for this can be complicated, some of which have been mentioned in § 5.1. The imperfection of external circuits could also be a contributor to this phenomenon. To eliminate these complexities, one must check the polarity and magnitude of V_H according to Eq. (5.3).

Fig. 5.6 and 5.7 are V_H vs. **B** for μc-Si (CP-128) and a-Si (CP-121), respectively. The measurement for μc-Si is relatively easy as compared to a-Si sample because of large signal/noise ratio. For a-Si sample CP-121, two current values ($V_{\parallel}$ = 12.5 V and $V_{\parallel}$ = 37.4 V) are used and both results are shown in Fig. 5.7. It is clear that V_H of both μc-Si and a-Si are proportional to **B** and *j*. The polarity of V_H also changes when the direction of **B** is switched.

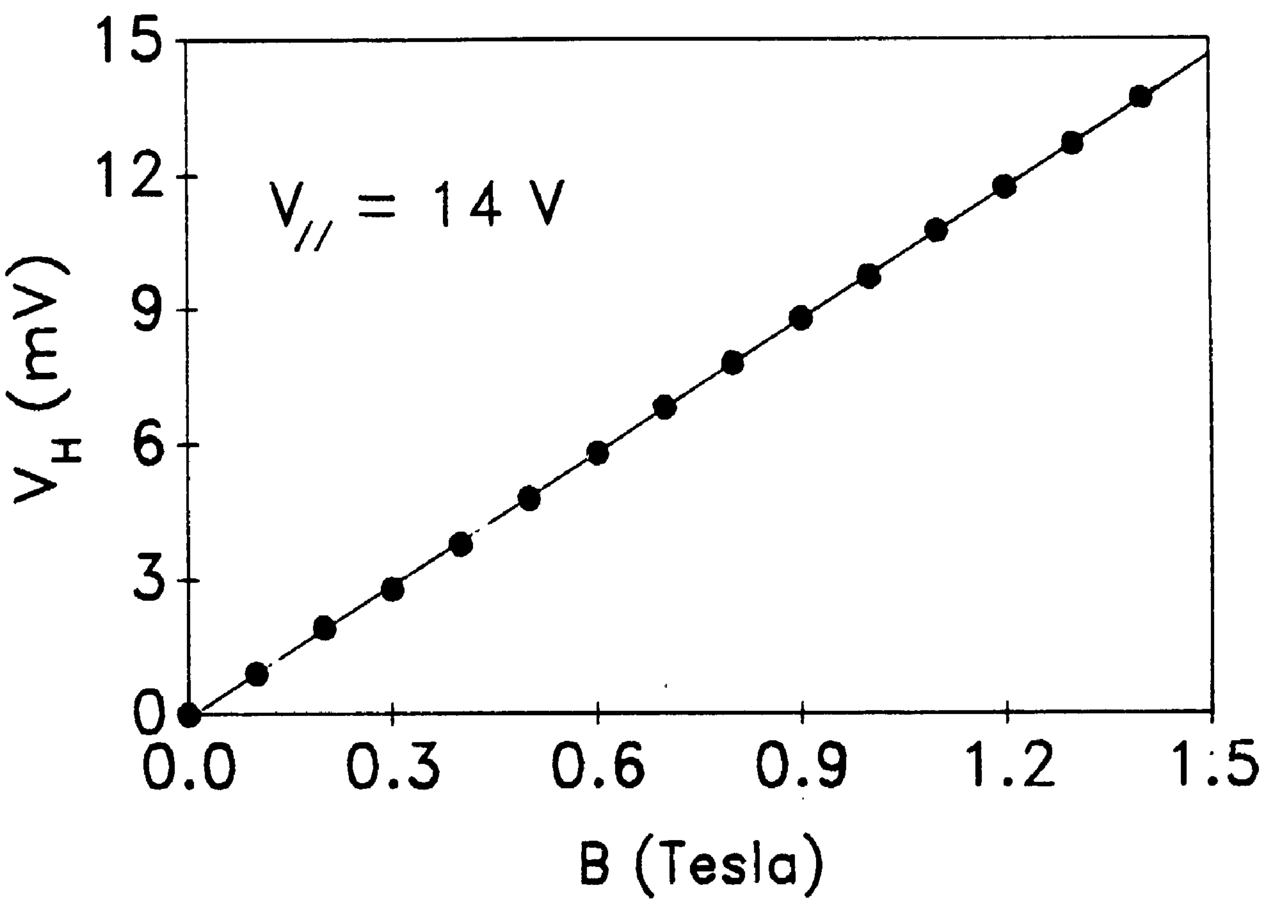

Fig. 5.6. Hall voltage vs. magnetic field for μc-Si samples.

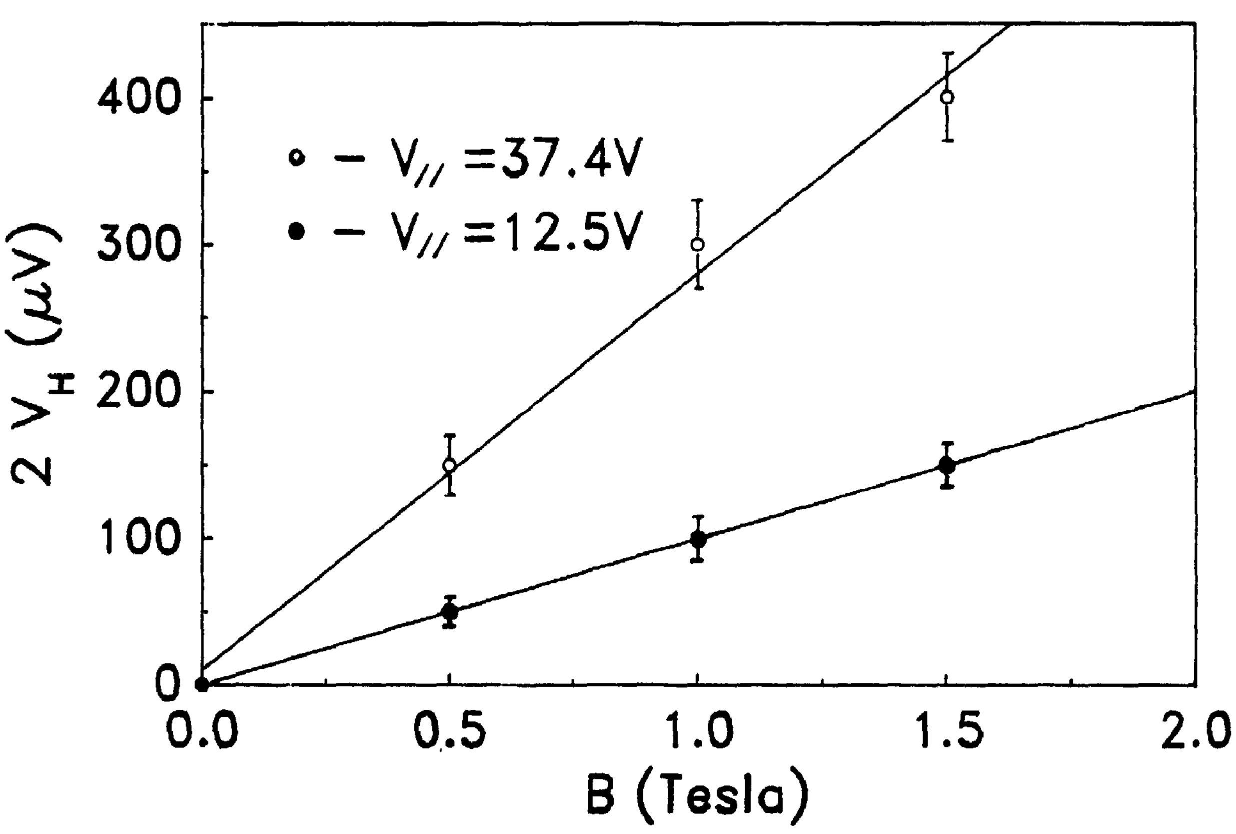

Fig. 5.7. Hall voltage vs. magnetic field for a-Si samples.

5.3 Results and Discussion

In the following, we present the experimental results and discussion of a-Si in § 5.3.1 and μc-Si in § 5.3.2 and § 5.3.3.

5.3.1 The Observation of Normal Hall Coeff: :ient

Hall effect measurements indicate that all microcrystalline samples show normal Hall sign while for amorphous samples both normal and anomalous Hall coefficient are observed. The normal Hall coefficient shown by the amorphous samples greatly interested us. In Fig. 5.8, we present two typ ι Hall effect measurement results for phosphorus doped amorphous Si samples CP145 and CP119. The result for a boron doped sample is in Fig. 5.9. Table 5.1 lists the deposition parameters of CP145 and CP119 (a microcrystalline sample CP118 is also listed in Table 5.1). We define $+\mu_H$ as Hall mobility from normal Hall coefficient (sign the same as its microcrystalline counterpart) and $-\mu_H$ as Hall mobility from anomalous Hall coefficient(sign opposite to its microcrystalline counterpart). In Fig. 5.8, the magnitude of normal Hall mobility (CP119) is about 3 times higher than that of anomalous Hall mobility (CP145). In general, the magnitude of observed $|-\mu_H|$ from anomalous sample is substantially less than that of normal Hall samples.

It has been reported (Willeke, Spear, Jones and LeComber, 1982) and also found in our observation that all microcrystalline films have normal Hall coefficient. An important question arises: is CP119 really an amorphous material? To answer this question,

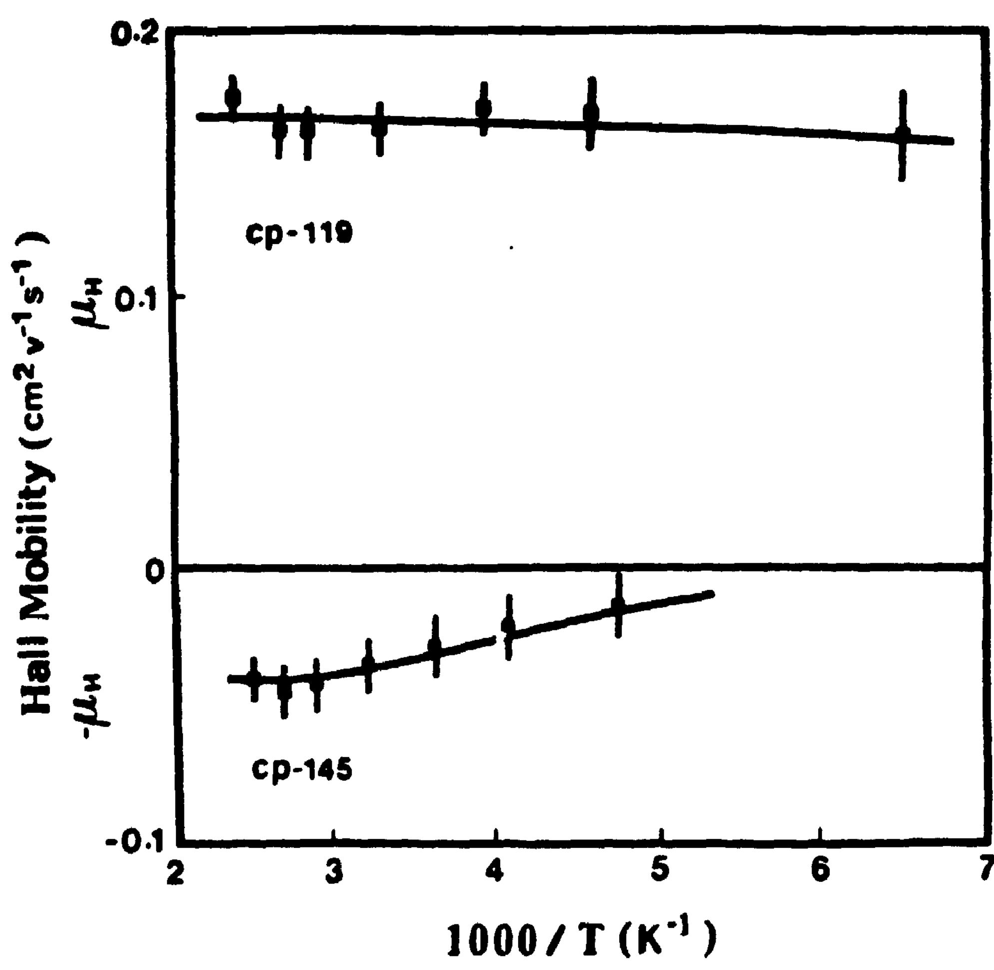

Fig. 5.8. Hall mobility of P doped a-Si CP-119 (Normal Hall sign, $R=1x10^{-3}$, $T_s=560\ ^oC$) and CP-145 (abnormal Hall sign, $R=4x10^{-3}$, $T_s=540\ ^oC$).

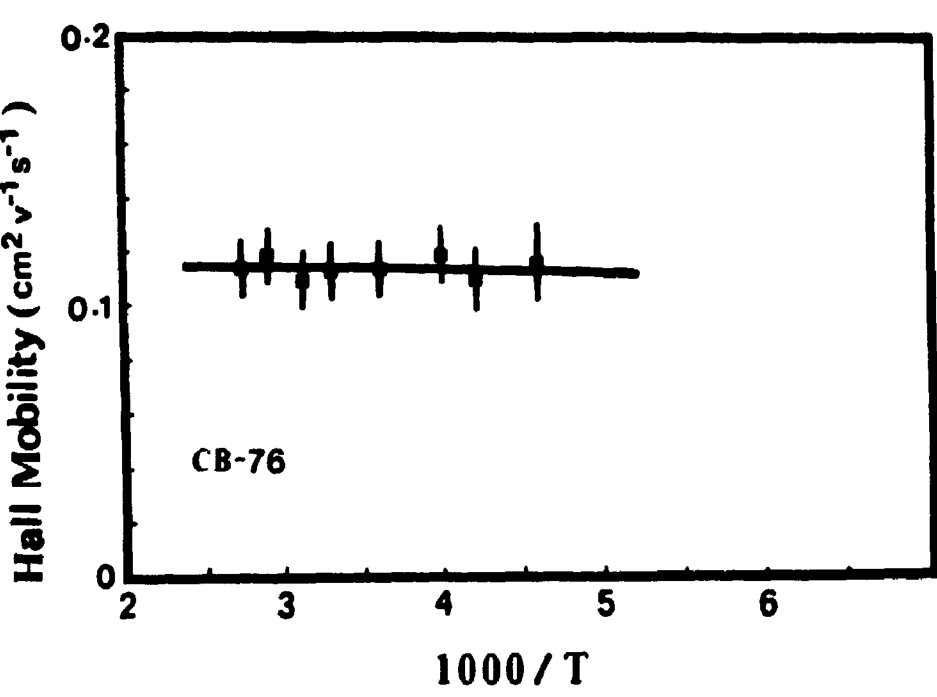

Fig. 5.9. Hall mobility of B doped a-Si CB-76 (Normal Hall sign, $R=1x10^{-3}$, $T_s=500\ ^oC$).

Table 5.1. Deposition parameters of CP145, CP119 and CP118

	CP145	CP119	CP118
Gas ratio R:	4×10^{-3}	1×10^{-3}	1×10^{-3}
Substrate Temperature T_s :	540 °C	560 °C	580 °C
P concentration in film S	4.8 at.%	1.31 at.%	1.7 at.%
Room temperature conductivity σ:	$2\times10^{-2}(\Omega\text{-cm})^{-1}$	$0.3(\Omega\text{-cm})^{-1}$	$102(\Omega\text{-cm})^{-1}$
Hall Mobility μ_H :	$0.04 cm^2/V\ s$	$0.15 cm^2/V\ s$	$3.6 cm^2/V\ s$

extensive structure analysis was carried out. All the available structure analysis techniques confirmed that CP119 was amorphous in structure. Fig. 5.10 shows the Raman scattering results for both CP145 and CP119, taken from the same samples used for Hall measurement. For comparison, the spectra of n-type single crystal Si and LPCVD microcrystalline film are also included in Fig. 5.10. The broad peaks of CP119 and CP145 around 475 $(cm)^{-1}$ are typical amorphous Raman optical mode peaks. X-ray diffraction on CP119 showed no crystallinity (Fig. 5.11). Transmission electron microscopy on CP119 revealed a typical amorphous diffraction pattern which is shown in photo plate 2.

Studies on transport properties also indicate that CP119 belongs to amorphous, not microcrystalline family. For example, the conductivity of μc-Si under the same dopant gas ratio should be at least 2 to 3 orders of magnitude higher than that of CP119. The temperature dependence of the Seebeck coefficient of CP119 was typical of amorphous Si, and different from that of μc material (Fig. 5.12). Conductivity vs. temperature for CP119 (normal amorphous sample) and CP145 (abnormal amorphous sample) are shown in Fig. 5.13.

We associate the normal Hall coefficient and high Hall mobility value of CP119 with a random silicon network structure possessing good short-range order. In Table 5.1, one notices that the solid phase phosphorus concentration in CP119 is substantially less than that of CP145, but the dark conductivity of CP119 at

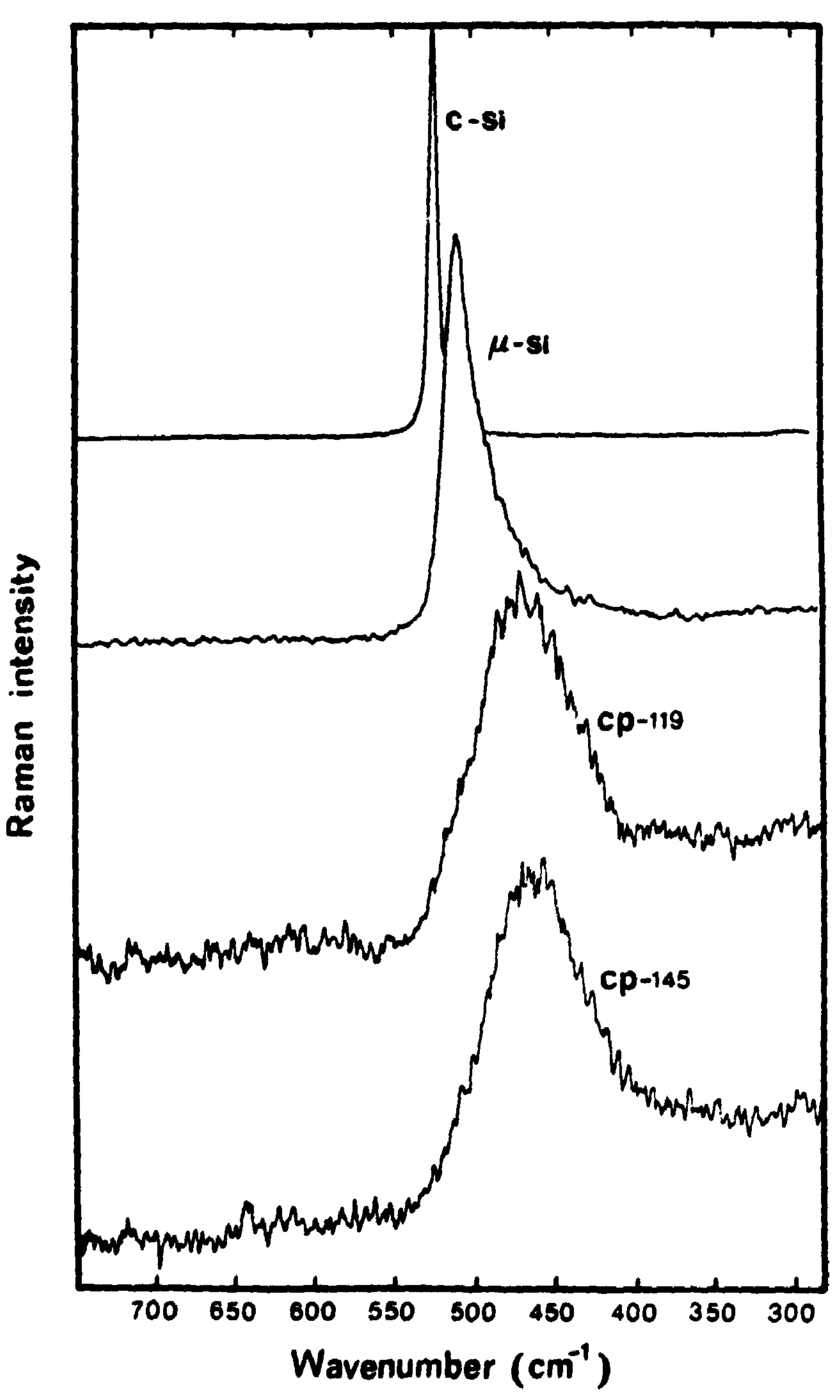

Fig. 5.10. Raman scattering of a-Si CP-119, CP-145 and μc-Si and c-Si.

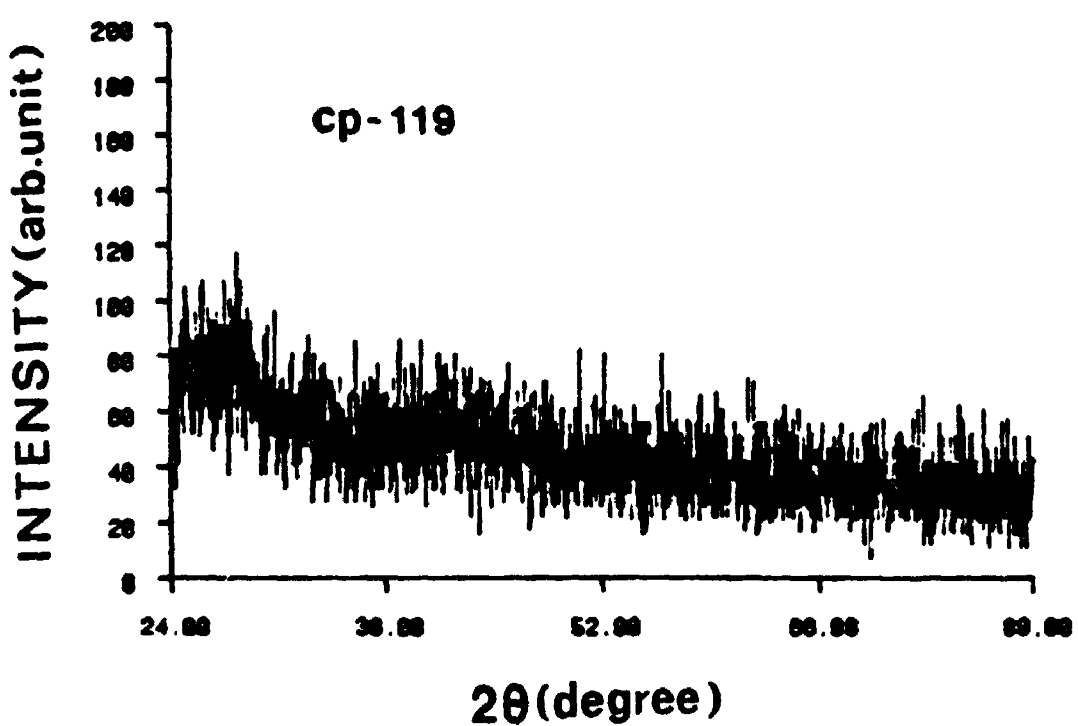

Fig. 5.11. X-ray diffraction of CP-119.

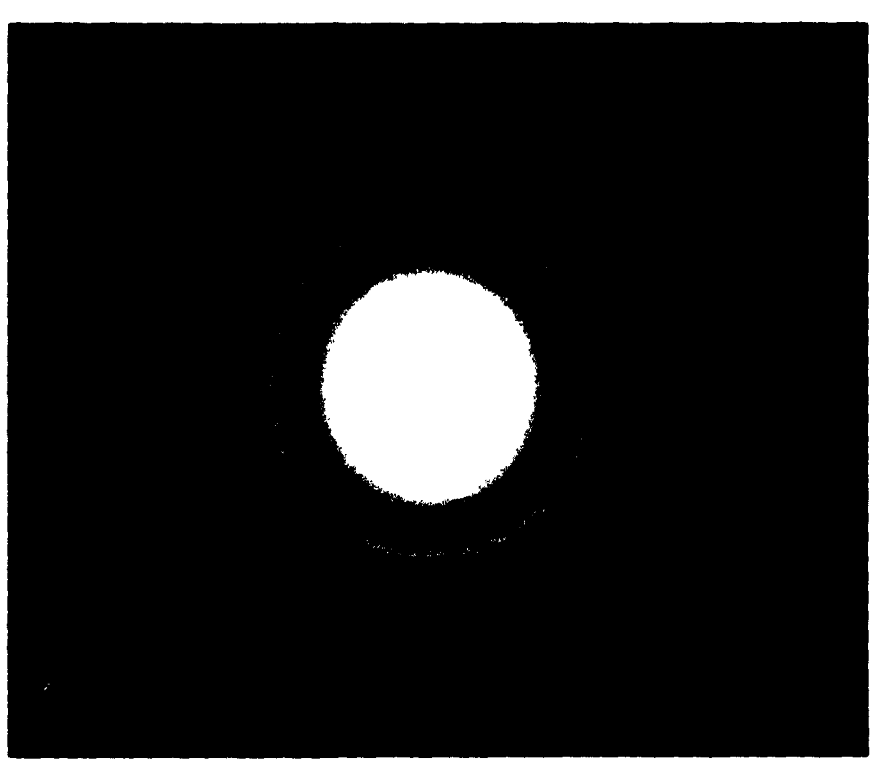

Plate 2. Transmission electron microscopy (TEM) of CP-119.

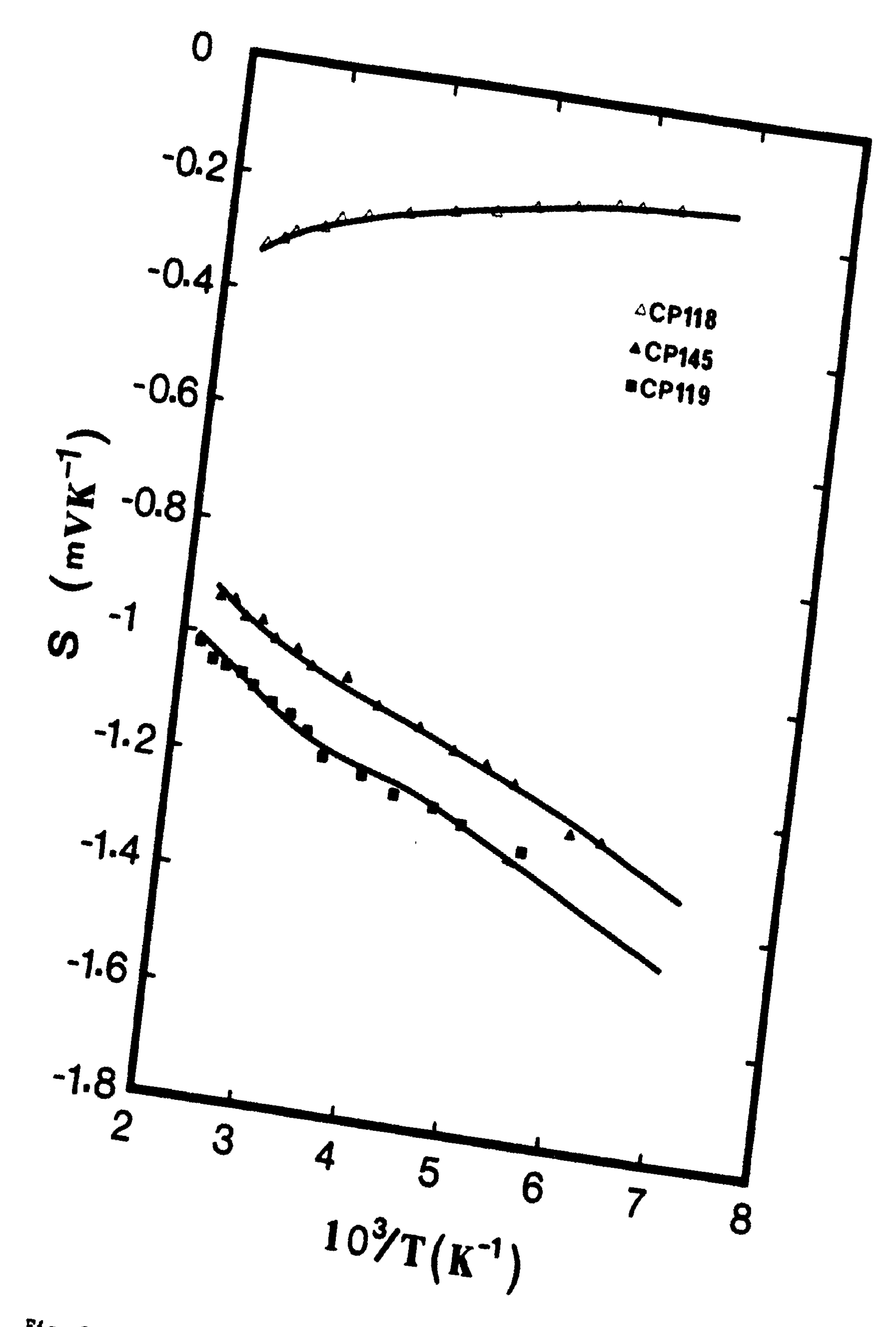

Fig. 5.12. Seebeck coefficient of a-Si (CP-119, CP-145) and μc-Si (CP-118).

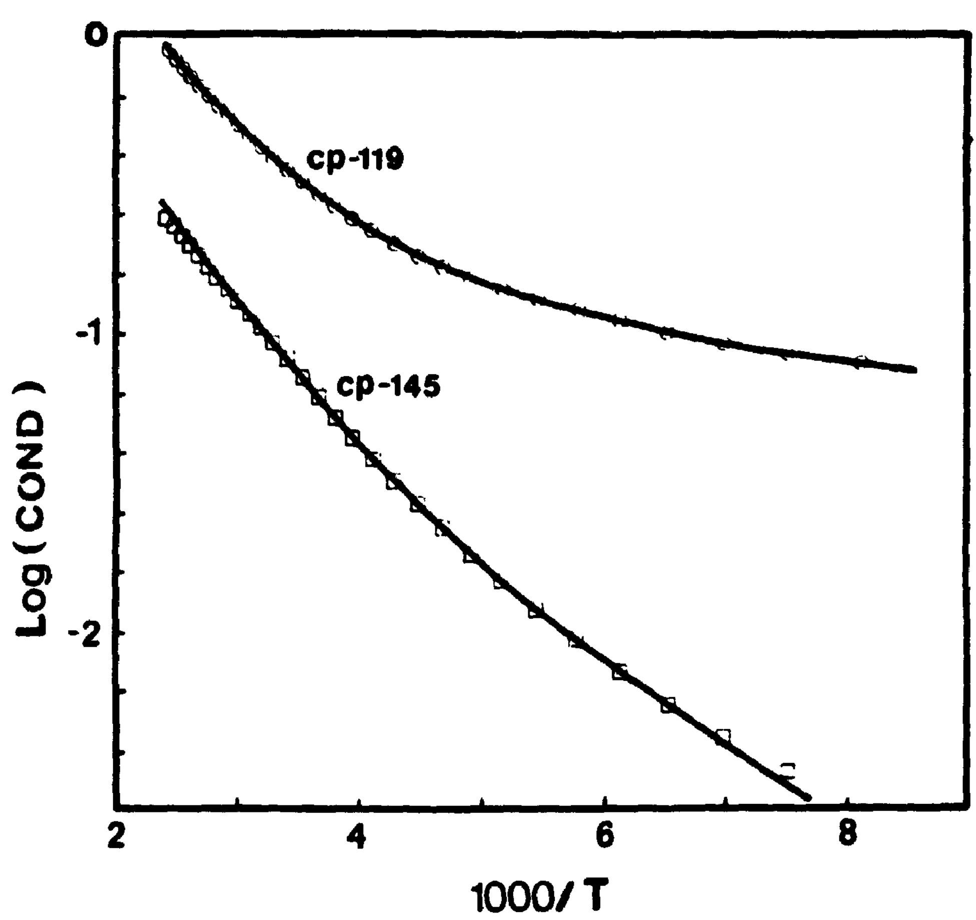

Fig. 5.13. σ vs. 1/T of normal sample CP-119 and abnormal sample CP-145.

room temperature is one order of magnitude higher than that of CP145. The conductivity (0.3 $(\Omega\text{-cm})^{-1}$) of the LPCVD samples, e.g., sample CP119 (normal Hall material), has the highest value reported so far among amorphous Si materials containing the same amount of dopant fabricated by various methods. However, it is still 2 to 3 orders below that of μc-Si. High doping efficiency is an indication of good network structure.

Double reversal of the Hall constant is an ubiquitous feature of glow-discharge amorphous silicon (a-Si:H). Sign anomaly is accounted for by theoretical models (Friedman, 1978, Emin, 1977, Movaghar, 1985) only in the limit of extreme strong localization in which the Ioffe criterion, i.e., localization length less than atomic spacing, is invoked. Even in this limit, the normal sign is not excluded. The sign is dependent on the ring statistics of the silicon network (see chapter 2). If the continuous random network is taken as a model for the ideal amorphous silicon structure, six-member rings prevail* , and thus the sign should be normal according to this theory. It is surprising that the normal Hall effect has not been found in glow-discharge a-Si. The glow-discharge material is deposited in the presence of hydrogen, and the film contains more than 5 at.% of H. Hydrogen relieves

---

* *In the continuous random network models, the statistics of the five-member rings range from 0% in the Connell-Temkin model, to 20% in the Polk model. See discussions in B.Y. Tong and F.C. Choo, Solid State Commun. 20(1976)957; also see R. Grigorovici, in "Amorphous and Liquid Semiconductors, Edited by J. Tauc (Plenum, London, 1974), pp.45-99.*

stiffness in the structure (Knights, 1980), and may have changed the ring statistics significantly. The ring statistics of a network model containing H has not been studied. By contrast, the LPCVD films contain much less H, the maximum amount observed being less than one-tenth of that in the glow-discharge material.

There are two classes of disorder that can cause localization in a-Si: topological structural disorder and random scattering centers such as defects and foreign atoms. If the continuous random network is taken as the ideal model of a-Si without H, the former alone is not likely to bring about the strong localization. Short-range local order in this model is well preserved* . Recent Raman studies on a-Si showed that the short-range order of amorphous material can be improved substantially by optimizing the fabrication conditions (Lannin, Maley and Kshirsagar, 1985). In our quest for amorphous specimen having the normal sign in the Hall coefficient, we aimed at minimizing the latter, including H. We carefully mapped out a wide range of the fabrication parameters of the LPCVD system. As demonstrated in the previous chapters, those parameters are related or can be translated into physical quantities such as crystallinity, concentration of dangling bond, dopant and hydrogen. These parameters are not mutually independent. For example, an increase in dopant concentration ($< 10^{19}$ cm^{-3}) simultaneously reduces the amount of dangling bonds. Amorphous silicon with the normal sign is found only in a small

---

* *In the polk model, the bond length is hardly changed at all, and the bond-angle deviation is about 9%; see Polk, D.E. and Boudreau, D.S., Phys. Rev. Lett. 31(1973)92.*

region in the multidimensional parameter maps shown in Fig. 5.14 and Fig. 5.15. So far, four samples (n-type) in this region showed normal Hall coefficient. They all have the same fabrication conditions, i.e., $R = 1x10^{-3}$ and T_s = 560 °C. One boron doped sample showed normal sign ($R = 1x10^{-3}$, T_s = 500 °C).

One may raise the question of whether these samples are composed of microcrystals too small to be detected by x-ray diffraction, Raman spectroscopy, and TEM. We believe this is not so. In the parameter map, the region of producing the normal sign material lies almost totally within the amorphous realm. Only on the high substrate temperature side does it touch the μc-Si region. If we move from the normal region in the direction of either too much or too little dopant concentration, we end up in the abnormal amorphous region. Furthermore, physical properties of the normal sign material have characteristics distinctively different from those of μc material (for example, the Seebeck coefficient). If the material is a composite of crystals of such small size as to escape detection, the amount of grain -boundary states must be overwhelmingly large.

5.3.2 Hall Effect of Microcrystalline Samples

Hall effect measurement of a-Si cannot provide important information such as carrier type and concentration of the material because: i) sign anomaly of R_H , and ii) the relation between conduction mobility μ_D and Hall mobility μ_H is complex and unknown (see chapter 2). For μc-Si, however, conventional

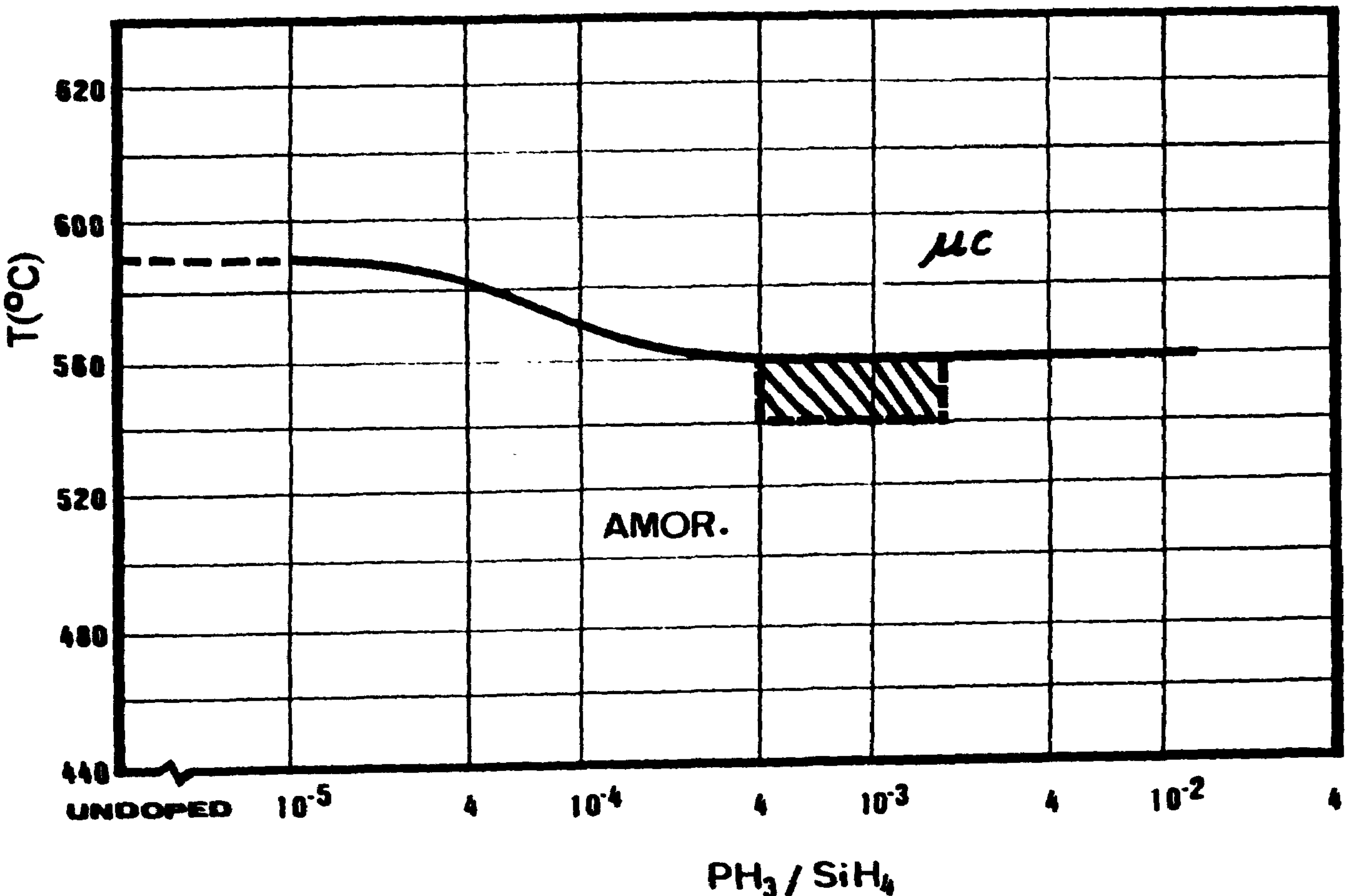

Fig. 5.14. The area (shaded) where normal Hall samples are found (P doped).

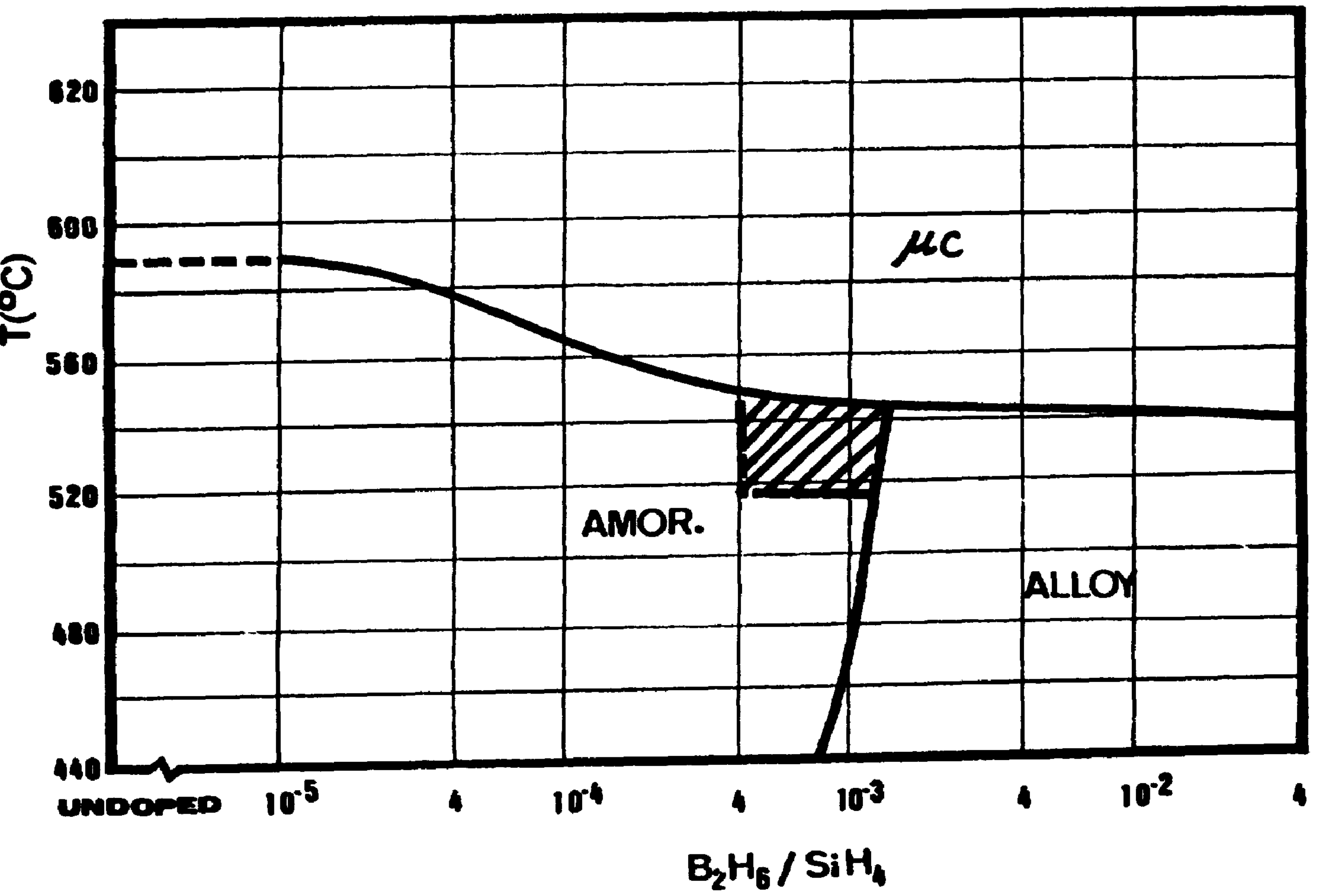

Fig. 5.15. The area (shaded) where normal Hall samples are found (B doped).

semiconductor transport theory are expected to be applicable (Willeke, Spear, Jones and LeComber, 1982), e.g.,

$$\mu_H = r\,\mu_D \tag{5.12}$$

where μ_D is the conduction mobility and r is a factor depending on the scattering mechanisms; in the case of a crystalline semiconductor, it varies between 1.2 and 2, and approaches unity in the limit of degeneracy. In the absence of any detailed knowledge of the scattering mechanisms in the μc-Si specimens and particularly when one's interest is to estimate the carrier concentration where the order of magnitude is important, it appeared reasonable to set $r = 1$. The carrier concentration n in extended state can then be calculated by:

$$R_H = -\frac{1}{n\,|e|} \tag{5.13}$$

Following Eq. (5.13), the n of some phosphorus doped LPCVD μc-Si fabricated at $T_S = 600\ ^{\circ}C$ and gas ratio between 4×10^{-5} and 1×10^{-2} are shown in Fig. 5.16. The n increases with gas ratio up to 4×10^{-3}. After 4×10^{-3}, n begins to decrease, possibly due to higher defect density caused by increasing phosphorus atoms in the Si network.

In chapter 3, we have discussed the correlation between gas phase ratio R and solid phase dopant ratio S of samples fabricated under different conditions. The relation is complicated, depending

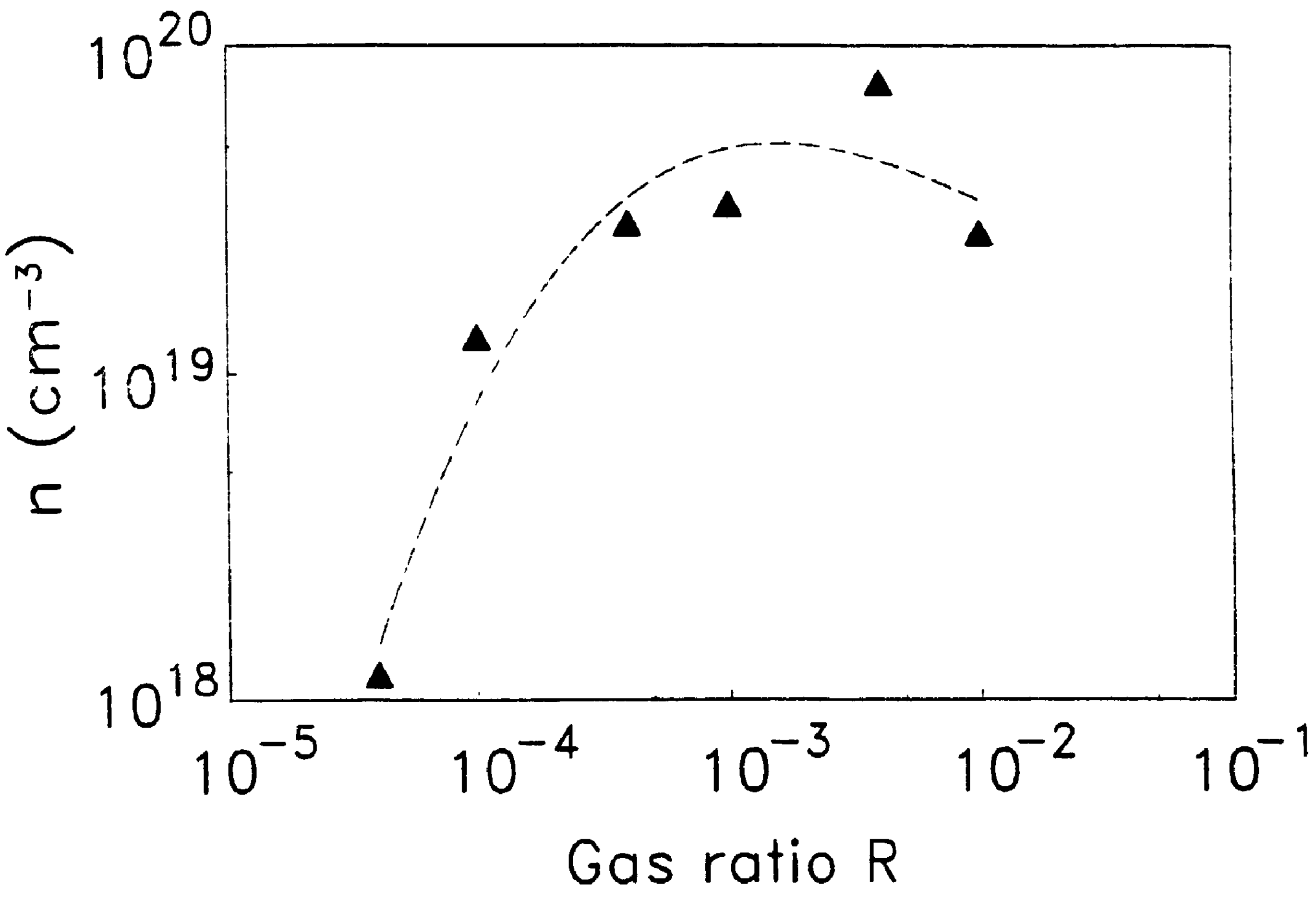

Fig. 5.16. Carrier concentration *n* vs. gas ratio R for P doped μc-Si at T_s = 600 °C.

upon many parameters such as gas composition, substrate temperature, flow rate, etc. In general, the S values are much higher than R values. If we go one step further, an even more interesting and fundamentally important question arises: for a sample with determined solid phase dopant concentration, what percentage of the dopant atoms in the material network are doping active, i.e., what is the doping efficiency of our LPCVD material? For a-Si, this is a rather difficult question because Hall effect cannot provide reliable *n* of a-Si. It is possible, however, to give a fairly accurate estimate for μc-Si based on Eq. 5.13. In Table 5.2, we list the solid phase concentration S (at./cm^3) of P doped samples fabricated at T_s = 600 °C and the corresponding carrier concentration *n* and doping efficiency *n*/S for each sample. S, *n* and *n*/S as function of R are also shown in Fig. 5.17. One can see that the doping efficiency of these samples decreases when the doping level is toc low (low R) or too high (high R). In the middle range of R, the doping efficiency reaches its high value: for the sample discussed here, it is on the order of 10% .

An electrical compensation model can be used to explain the low doping efficiency at low doping levels. This model is presented schematically in Fig. 5.18. In the middle of the band gap, there exists a band of states corresponding to the ncutral dangling bond D^o. These dangling bonds are paramagnetic and have a g value around 2.0055 as obtained from evaporated Si thin films. If an electron is captured by a D^o state, it will convert to a charged, non-paramagnetic D^- state and cannot be detected by

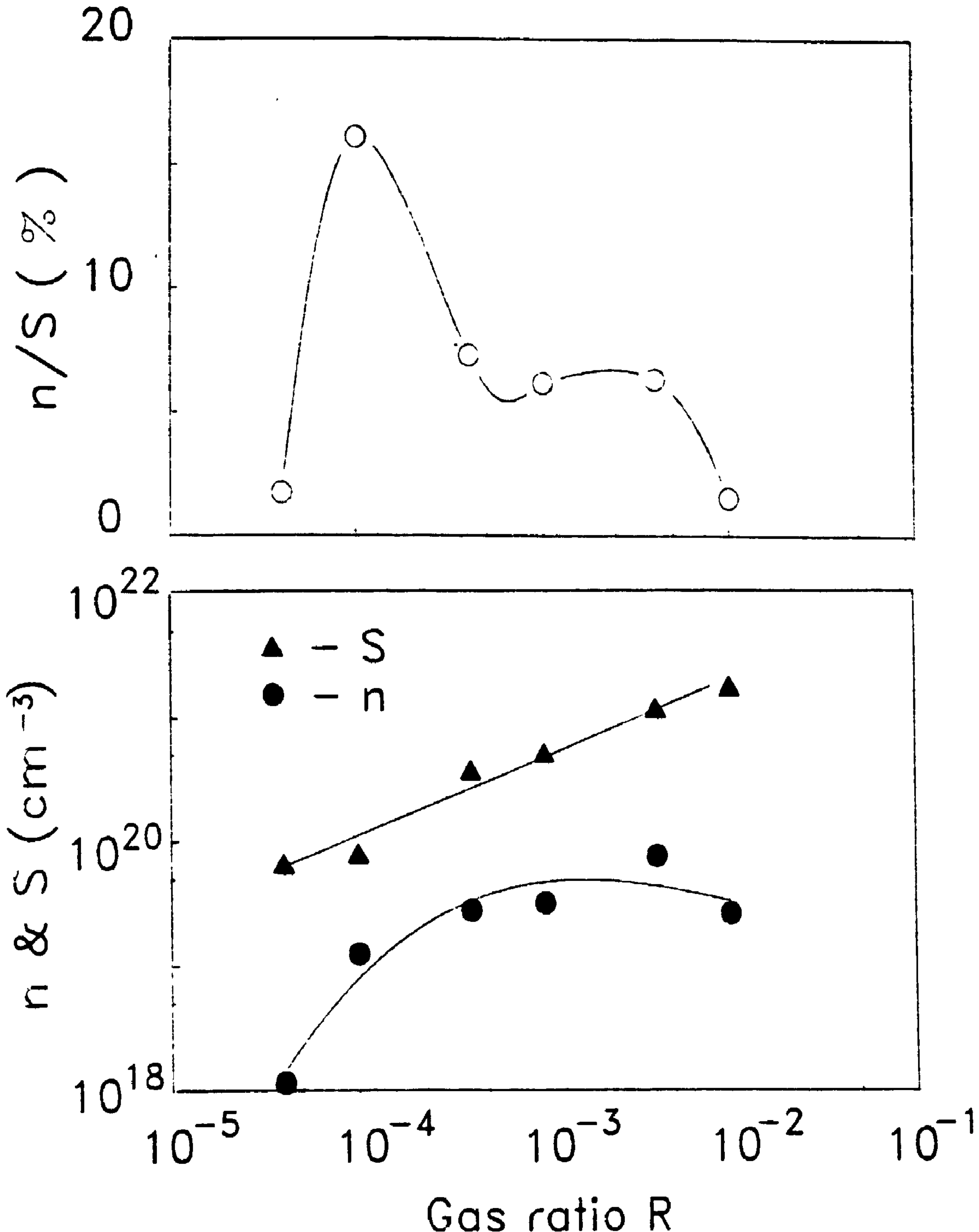

Fig. 5.17. P concentration in film (S), carrier concentration (n) and doping efficiency (n/S) vs. gas ratio R for μc-Si samples at T_s = 600 °C.

electron spin resonance (ESR) measurement. Evidence of the D^- states has been provided by light-induced ESR experiment (Friederich and Kaplan, 1980). Near the mobility edge there also exists tail states induced by disorder. Conduction-band tail states can also capture a electron and become charged and paramagnetic.

Table 5.2. Solid phase concentration S and carrier concentration *n* of μc-Si at T_s = 600 °C.

R	S(at./cm^3)	n(cm^{-3})	n/S (%)
4×10^{-5}	6.9×10^{19}	1.2×10^{18}	1.7%
1×10^{-4}	8.3×10^{19}	1.3×10^{19}	15.6%
4×10^{-4}	3.9×10^{20}	2.9×10^{19}	7.4%
1×10^{-3}	5.3×10^{20}	3.3×10^{19}	6.2%
4×10^{-2}	1.2×10^{21}	7.8×10^{19}	6.3%
1×10^{-2}	1.8×10^{21}	2.7×10^{19}	1.5%

According to the model in Fig. 5.18, when dopant atoms P are introduced into the material network, before electrons can become available in the conduction band, the dangling bonds D^o in the middle of the band gap have to be filled first. The process is:

$$P + D^o \longrightarrow D^- + P^+ \qquad (5.14).$$

It is known that due to the lack of H atom in the material network, the dangling-bond density of undoped LPCVD Si is usually

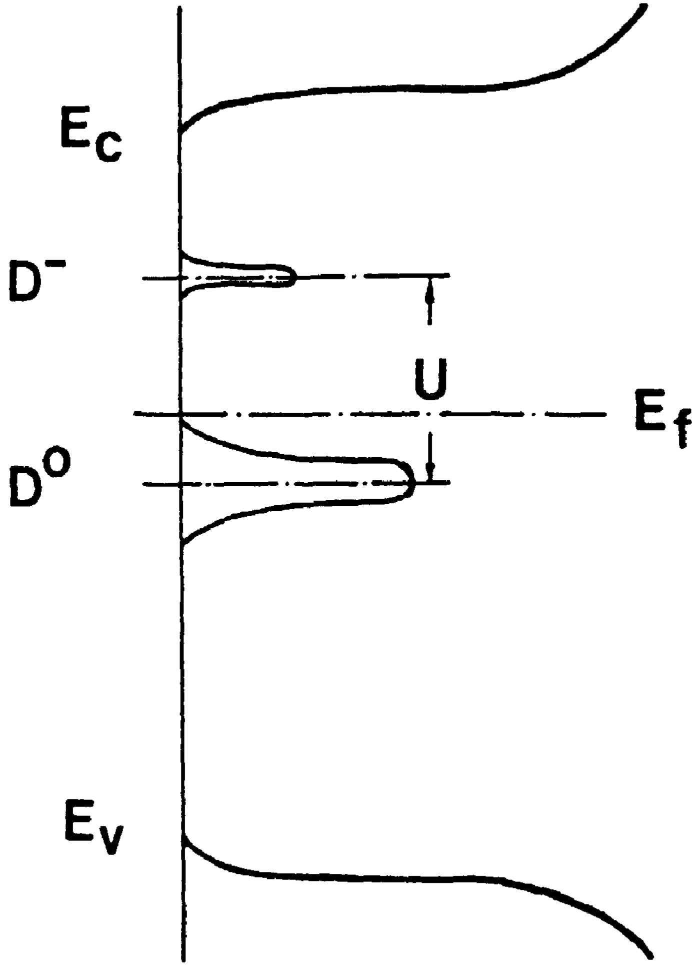

Fig. 5.18. A band diagram for the electrical compensation model.

high. For example, the undoped LPCVD μc-Si sample fabricated at 600 $^{\circ}$C has a dangling-bond density of 7×10^{19} cm^{-3} (from electron spin resonance (ESR) measurement with g = 2.0055. The ESR measurement was carried out in the Dept. of Chemistry of U.W.O.. The apparatus is an X-band spectrometer with a microwave frequency of 9.407 GHz. The magnetic field was set at 3370 Gauss and the scan range was 100 Gauss. The measurement was at room temperature.). For μc-Si, those dangling bonds are most likely located at the grain boundaries. When dopant atoms such as P are introduced into the material, large number of P atoms become doping inactive because electrons are trapped by the dangling-bonds situated in the middle of the band gap. This is the reason of low doping efficiency at very low doping levels. Following this model, one expects to see a rapid increase in carrier concentration n in conduction band after all the dangling bonds are filled by electrons. This is indeed observed and shown in Fig. 5.19. In Fig. 5.19, n increases drastically after solid phase concentration S exceeds 7×10^{19}(at./cm^3). This threshold value of S coincides very well with the dangling-bond density of undoped μc-Si (7×10^{19} cm^{-3}). Further support of this model can be obtained from ESR measurements which is shown in Fig. 5.20. All the samples in Fig. 5.20 are μc-Si fabricated at T_S = 600°C. Starting from undoped sample, the ESR density 7×10^{19} cm^{-3} (open circle in Fig. 5.20) gradually decreases as the dopant gas ratio R is increased (solid circle in Fig. 5.20). The g factor of the resonance signal is around 2.0055, usually attributed to dangling bonds (Magarino, Kaplan and Friederich, 1982). At R = 1×10^{-4},

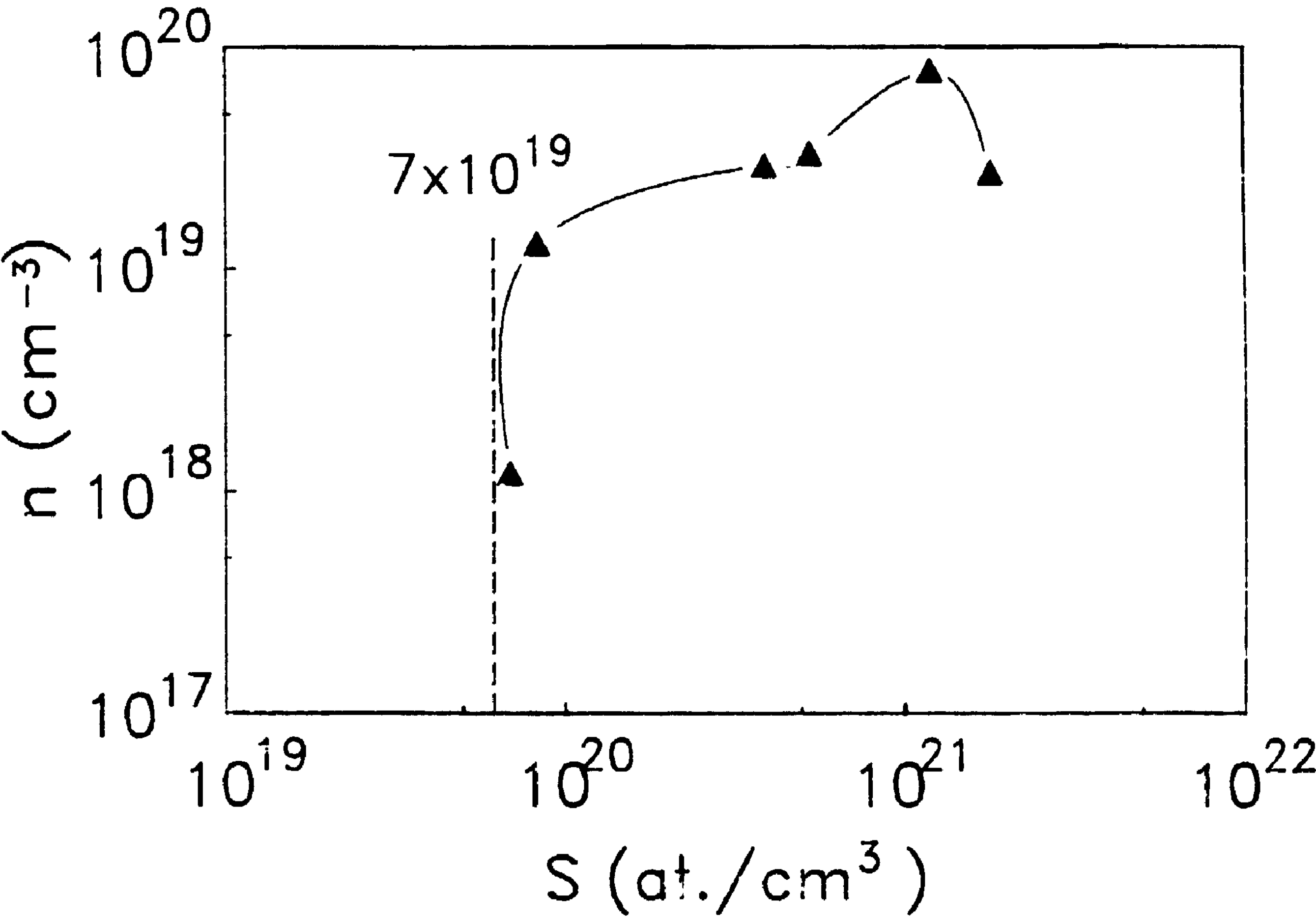

Fig. 5.19. Carrier concentration n vs. solid phase P concentration S of μc-Si samples fabricated at T_s = 600 °C.

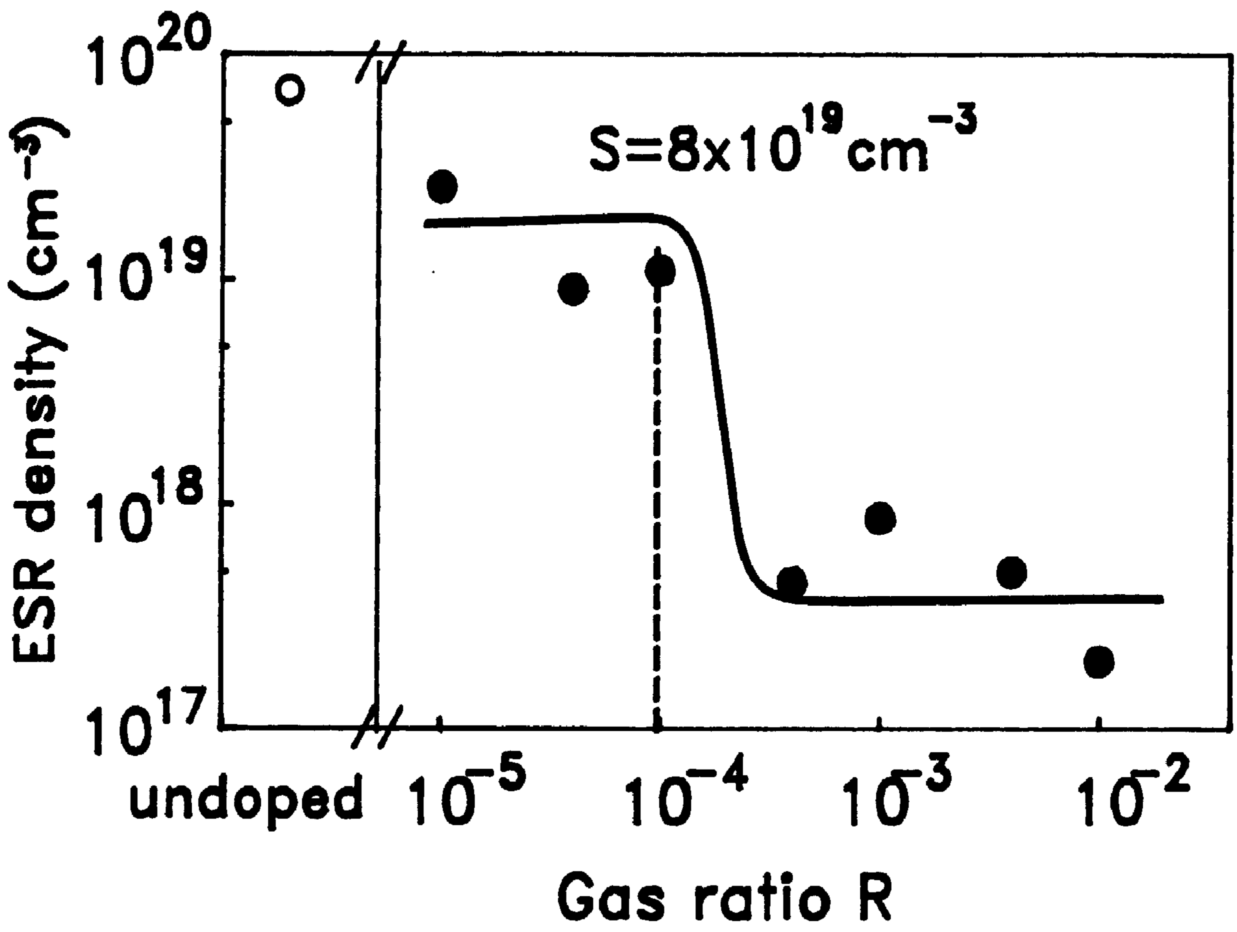

Fig. 5.20. Electron spin resonance (ESR) vs. R of samples at T_s= 600 °C.

the ESR density drops by almost 2 orders of magnitude - clearly an indication that at this doping level, most of the dangling bonds in the material are saturated by electrons. R = 1×10^{-4} corresponds to a solid phase concentration S=8.3×10^{19} (see Table 5.2). This number again agrees well with the ESR density of undoped sample. The highest doping efficiency is obtained at a doping level around this value (Fig. 5.17).

It is no surprise that, when the solid phase concentration is just above the dangling-bond density, one achieves the highest doping efficiency. The doping efficiency remains stable until R exceeds 4×10^{-3} (Fig. 5.17) where it begins to decline again. From Fig. 5.17, carrier concentration n decrease at high R, possibly due to additional density of states caused by too many dopant atoms in the material network. Magarino et al. observed in their P doped CVD a-Si that at gas ratio of 4×10^{-4}, the ESR density of g = 2.0058 reached its minimum by dropping over one order of magnitude from its undoped value. This is due to electron compensation of dangling bonds in the middle of the band gap. Above 4×10^{-4}, another ESR signal with g = 2.0043 begin to increase, reaching its maximum at 1×10^{-3}, and then decreases again (Magarino, Kaplan and Friederich, 1982). They explain that the resonance signal with g = 2.0043 comes from the states near conduction-band edge (also see Street and Biegelsen, 1980). After the dangling bonds in the middle of the bad-gap have been filled, electrons can be captured by the band-tail states. If these states are sufficiently localized so that double occupancy

will not occur, one then will see an increase in ESR with g = 2.0043. Further decrease in ESR (g = 2.0043) can be interpreted by the onset of double occupancy of those band-tail states. This process probably is responsible for the loss of carrier concentration in our sample at high doping levels (Fig. 5.17) because heavy doping increases the disorder of the material network and enhances the band-tail states. Furthermore, when solid phase concentration is high, the clustering or segregation of P atoms may occur, particularly in the grain boundary regions - a factor which could also contribute to the low doping efficiency at high doping levels. However, we do not have direct evidence to support this explanation.

Due to the high doping efficiency, the material fabricated in the middle of the doping level R should have better structure as compared to the ones fabricated at low or high doping levels. In § 5.3.1, we indicated that normal Hall samples are only observed in a narrow region in the fabrication condition maps (see Fig. 5.14 and 5.15). This region is located in the middle of the doping level and close to the μc-Si boundary. We believe that a-Si films fabricated in this small region have better structure as compared to the a-Si in other areas; and normal Hall coefficient is the result of good network structure.

5.3.3. Post-hydrogenation of μc-Si

Another experiment related to the one in § 5.3.2 is the post-hydrogenation of μc-Si samples. It is well known that

hydrogen plays an important role in the electrical properties of hydrogenated amorphous silicon (a-Si:H) fabricated by glow discharge(GD) (LeComber, Jones and Spear, 1977) or plasma assisted (photo-induced) CVD (Konagai, 1986, Knights and Lucovsky, 1980). In these Si-H alloy materials, hydrogen is introduced into the material network during film fabrication and relatively high hydrogen concentration (5-20 at. %) is observed in the film. Attempts have also been made to improve the transport properties of amorphous, microcrystalline and polycrystalline Si material by post-hydrogenation techniques (Zhang et al., 1987, Puppin, 1987, Magarino et al., 1982, Seager et al., 1981). In general, post-hydrogenation will increase the dark-conductivity of lightly doped μc-Si, sometimes by orders of magnitude. The conductivity of a sample is the product of mobility and carrier concentration: $\sigma = e\ n\ \mu_D$. Hall effect measurement of μc-Si, when combined with the post-hydrogenation experiment, will be able to answer the question of which factor, n or μ_D , contributes most to the change of conductivity.

Hydrogenation was carried out in our lab. by an atom gun (FAB11NWF, Ion Tech. Ltd.) with a power supply (B50, Ion Tech.) mounted in a stainless steel vacuum chamber which could be pumped down to a pressure of 10^{-6} Torr. H_2 gas entered the gan through a needle valve. During the operation, H is ionized inside the gun and accelerated by a saddle electric field. Most of the energetic H ions are neutralized before they leave the gun, generating an atomic hydrogen beam of 1mm diameter and a divergent angle of 4°.

The beam contains 90% neutral species. The samples were placed on a flat stainless steel holder 25 cm in front of the gun. The beam energy was around 5 keV and the current 100 μA which is equivalent to a dose of $6x10^{14}/cm^2$ s. The hydrogenation time was between 8 to 10 min. and the substrate temperature was kept at around 400 °C during hydrogenation. Since the temperature is well below the film fabrication temperature, it is therefore unlikely to change the structure of the films. In order to confirm the hydrogenation effect, a similar sample, covered by a mask, was used as a comparison. No change was observed in the unexposed sample. More detailed information regarding post-hydrogenation and hydrogen profiling can be found in Dr. X.W. Wu's work (Ph. D. thesis, U.W.O., 1989).

Fig. 5.21 and 5.22 are the conductivity and Hall mobility value of some microcrystalline phosphorus doped samples (same as those in § 5.3.2) before and after hydrogenation. The samples were fabricated at 600 °C and their doping levels are between $4x10^{-5}$ and $1x10^{-2}$ (gas ratio). The grain sizes of these samples are all around 300 Å as obtained by X-ray diffraction. It is shown in Fig. 5.21 that for the low doping level samples, hydrogenation does have obvious effect on the conductivity while at high doping levels, the effect is not observable at room temperature. For these microcrystalline samples, the Hall sign are normal and the results are shown in Fig. 5.22. The Hall mobility before hydrogenation increases quite rapidly at gas ratios around $1x10^{-4}$. After hydrogenation, however, they remain at a relatively constant

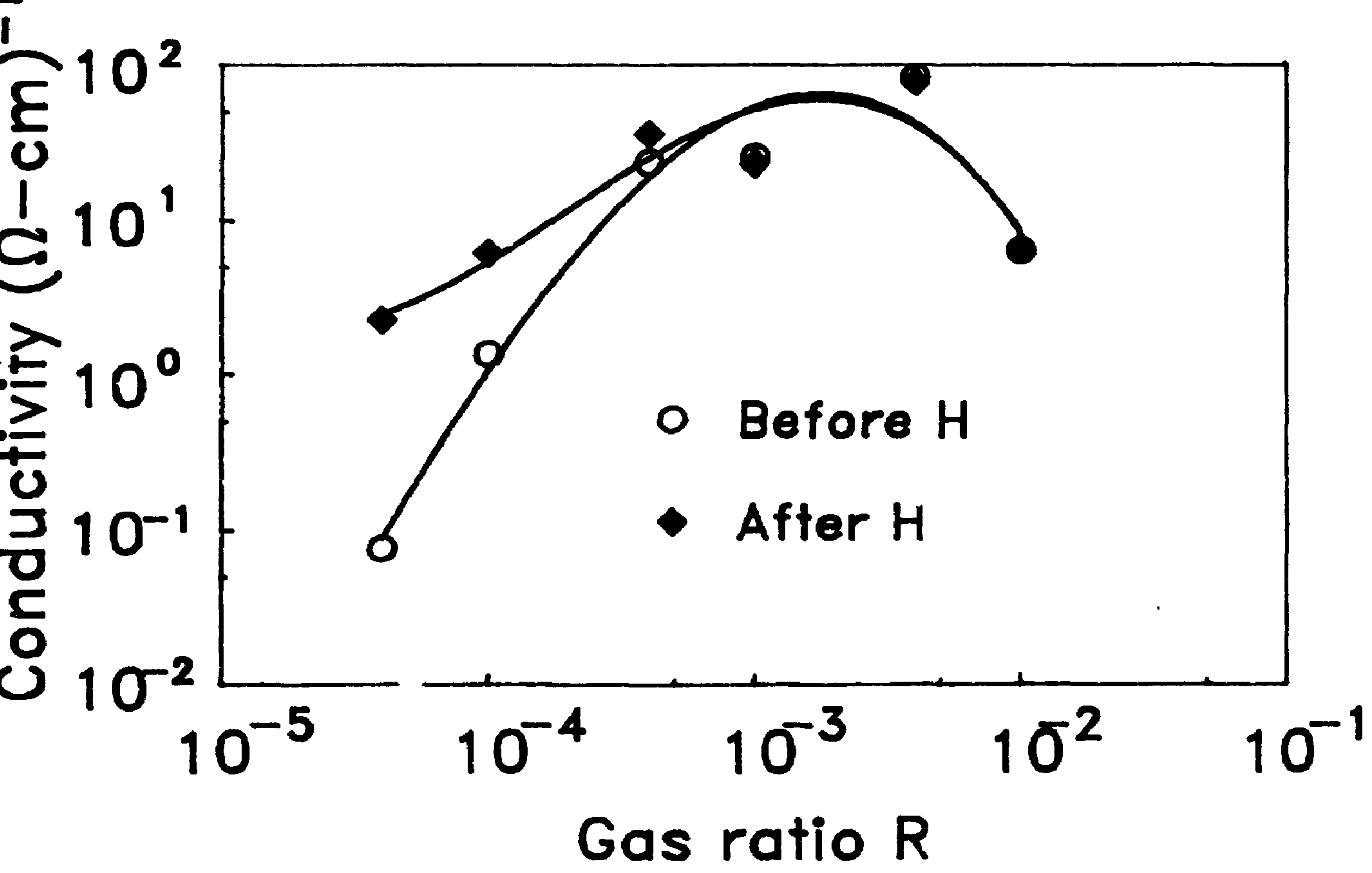

Fig. 5.21. Conductivity σ vs. gas ratio R before and after hydrogenation for μc-Si at T_s = 600 °C.

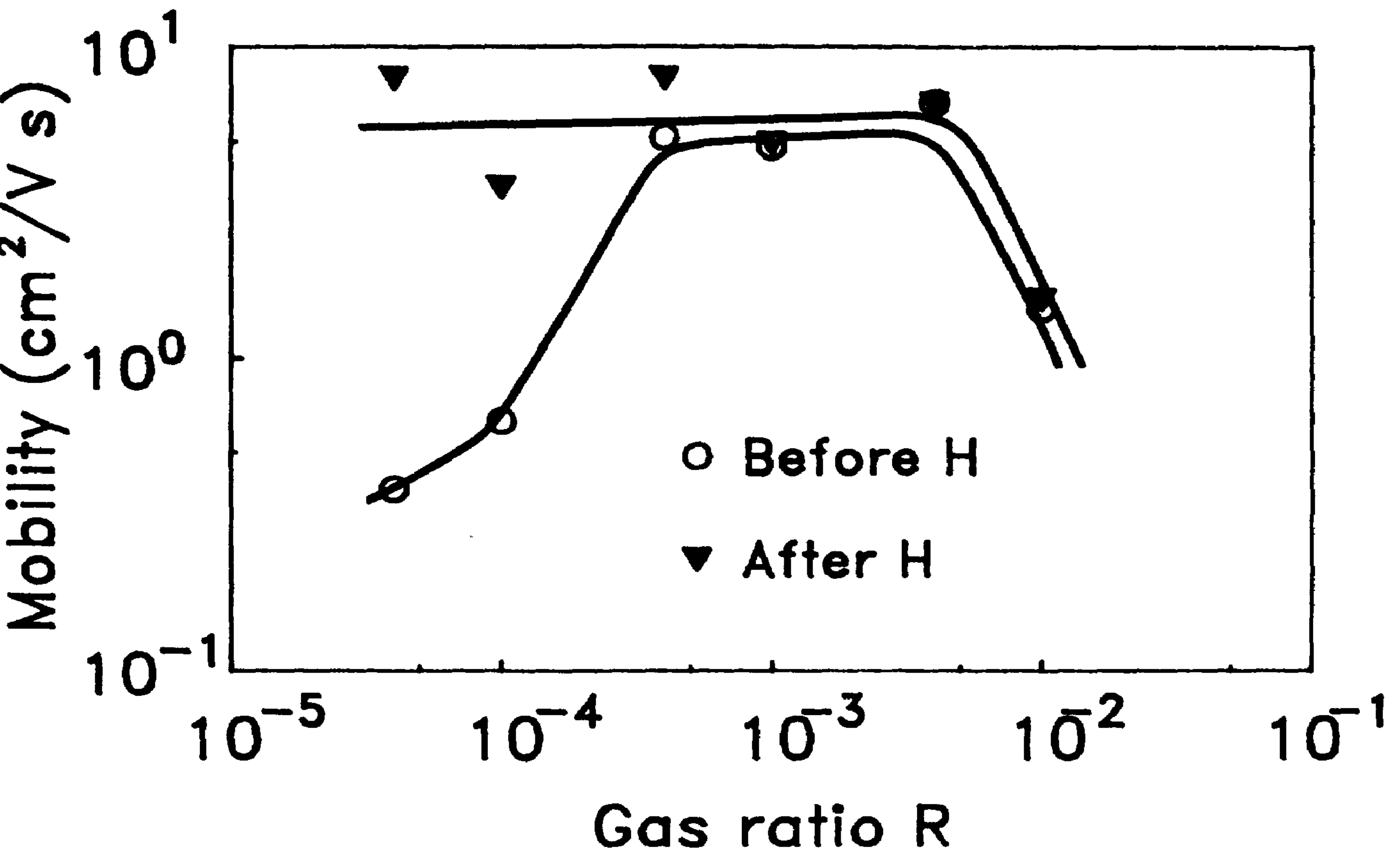

Fig. 5.22. Hall mobility μ_H vs. gas ratio R before and after hydrogenation for μc-Si at T_s = 600 °C.

value until very high doping concentrations. It is interesting to see that post-hydrogenation can increase the Hall mobility by over one order of magnitude. For example, the sample doped at gas ratio $4x10^{-5}$ changed its Hall mobility from 0.38 $cm^2/V.s$ to 7.9 $cm^2/V.s$ upon hydrogenation while its conductivity changed from $8.5x10^{-2}$ $(\Omega\text{-cm})^{-1}$ to 2.5 $(\Omega\text{-cm})^{-1}$. The major contribution to the conductivity in this case was from the change of mobility. If we assume the scattering factor to be unity, then the carrier concentration can be calculated and is shown in Fig. 5.23. Hydrogenation does not change the carrier concentration substantially.

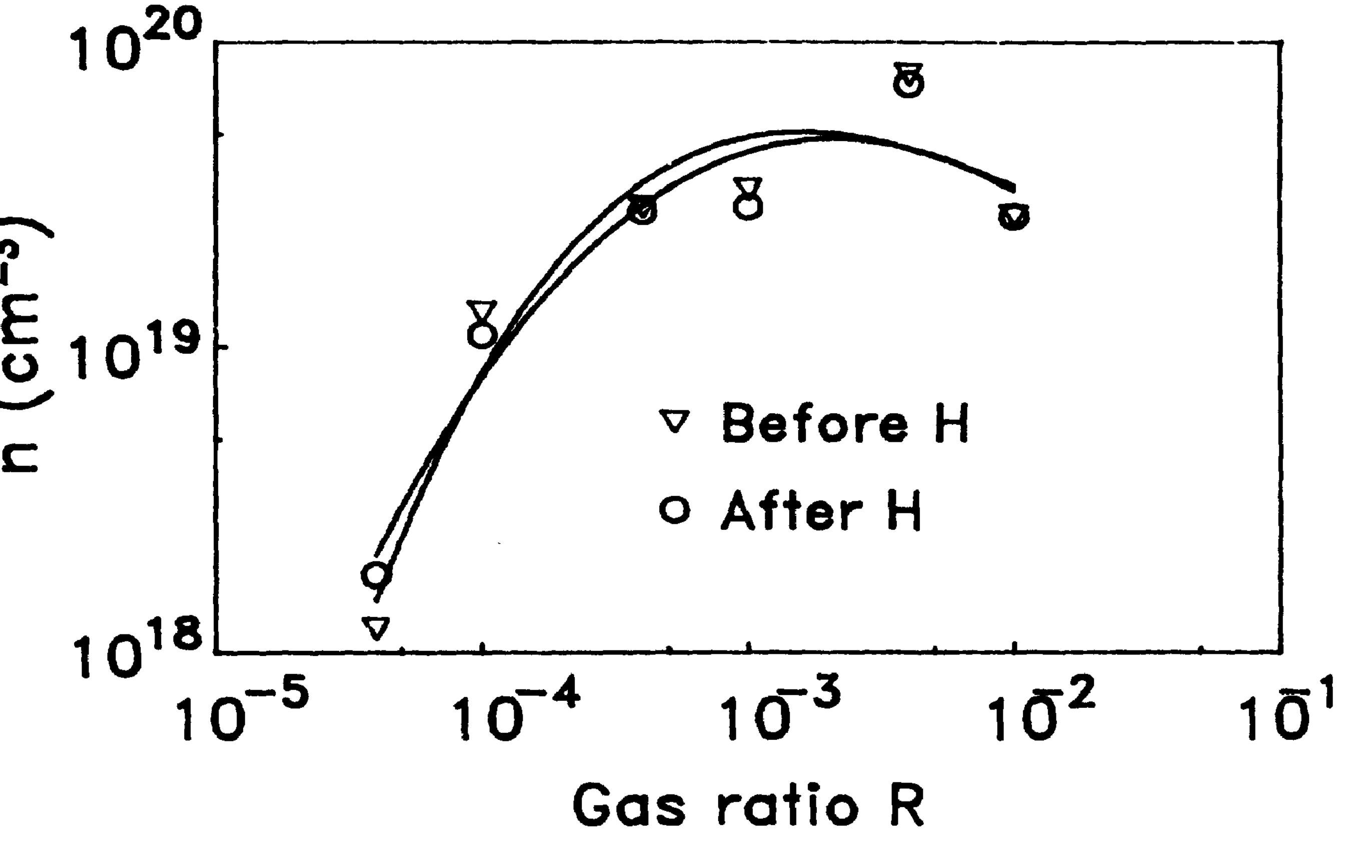

Fig. 5.23. Carrier concentration n vs. gas ratio R before and after hydrogenation for μc-Si at $T_s = 600$ °

Chapter 6 Conclusions

1). Si thin films with good electrical properties have been produced successfully by LPCVD method. By adjusting the fabrication parameters, one can obtain films with different compositions and different structures and hence, different electrical and optical properties. In the fabrication condition range adoptea in our lab., both amorphous (a-Si) and microcrystalline (μc-Si) silicon films are obtained,

2). The conductivity of our thin films can be (by introducing B_2H_6 or PH_3 into the film fabrication process) varied over ten orders of magnitude. Room temperature dark conductivity are higher than those produced by GD method (with the same gas ratio),

3). The transport property of a-Si and μ-Si are different. The heterojunction devices (n type LPCVD thin film on top of p type c-Si wafer) made by a-Si and μ-Si also exhibit different behavior,

4). The combination of transport properties with the results from X-ray diffraction, Raman scattering, transmission electron microscopy show distinctive boundary between a-Si and μ-Si in the fabrication condition map,

5). In a small area of the fabrication condition map, some samples in the amorphous region show normal Hall coefficient.

6). Experiments show that only a small portion of boron or phosphorus in the films is doping-active. For μc-Si, a single electrical compensation model works well.

References

Anderson, P.W., *Phys. Rev.* **109**, 1492 (1958).

Anderson, D.A. and Paul, W., *Philos. Mag.* B, **45**, 1 (1982).

Akhtar, M., Dalal, V.L., Ramaprasad, K.P., Gau, S.C. and Cambridge, A.J., *Appl. Phys. Lett.*, **41**, 1146 (1982).

Beyer, W., Mell, H. and Overhof, H., "*Amorphous and Liquid Semiconductors*" ed. by W.A. Spear (Edinburgh Univ. Press), p328 (1977).

Beyer, W., Fischer, R. and Overhof, H., *Philos. Mag.* B, **39**, 205 (1979).

Bragg, J.K., McCarty, L.V. and Norton, F.J., *J. Am. Chem. Soc.*, **73**, 2134 (1951).

Carlson, D.E., Smith, R.W., Magee, C.W., Zanzucchi, P.J., *Philos. Mag.* B, **45**, 51 (1982).

Chik, K.P., Du, N., John, P.K., Ou, E., Rastogi, A.C., Tam, K.H., Tong, B.Y., Wong, S.K., Wu, X.W., Yao, J., *J. Non-Crys. Solids*, **77&78**, 961 (1985).

Chik, K.P., Chan, P.H., Tam, K.H., Tong, B.Y., Wong, S.K. and John, P.K., *Philos. Mag.* B, **59**, 543 (1989).

Clark, R.P. and Pease, R.N., *J. Am. Chem. Soc.*,**73**, 2132 (1951).

Cohen, M.H., Fritzsch, H., Ovshinsky, S.R., *Phys. Rev. Lett.* **22**, 1065 (1969).

Davis, E.A., Mott, N.F., *Philos.Mag.* **22**, 903 (1970).

Delahoy, A.E., "*Proc. Photo-Opt. Instrum. Eng.*", **407**, 47 (1983).

Deneuville, A. and Brodsky, H., *J. Appl. Phys.* **50**, 1414 (1979).

Dresner, J., *Appl. Phys. Lett.*, 37, 742 (1980).

Dresner, J., "*Semiconductors and Semimetals*", Vol. 21, part C, p199 (1984).

Elliott, S.R., "*Physics of Amorphous Materials*", Longman Group Limited, New York (1984).

Ellis, F.B. Jr., Gordon, R.G., Paul, W. and Yacob, B.G., *J. Appl. Phys.*, 55, 4309 (1984).

Emin, D., *Ann. Phys.* (N. Y.), 64, 336 (1971).

Emin, D., *Philos. Mag.*, 35, 1189 (1977).

Emin, D., "*The Hall Effect and its Applications*", Edited by C.L. Chien and C.R. Westgate, (Johns Hopkins University, 1979), p281.

Friederich, A. and Kaplan, D., *Int. Conf. Semicond.*, 15, 1233 (1980).

Friedman, L. and Holstein, T., *Ann. Phys.* (N. Y.), 21, 494 (1963).

Friedman, L., *J. Non-Cryst. Solids*, 6, 329 (1971).

Friedman, L., *Philos. Mag.* B, 38, 467 (1978).

Fritzsche, H., "*Amorphous and Liquid Semiconductors*", edited by J.Tauc (London: Plenum Press), p.221 (1974).

Ghiassy, F., Jones, D.I. and Stewart, A.D., *Philos. Mag.* B, 52, 139 (1985).

Hirose, M., *J. Crystall Growth*, 45, 126 (1978).

Holstein, T., *Ann. Phys.* (N. Y.), 8, 325, 343 (1959).

Jan, Z.S., Bube, R.H. and Knights, J.C., *J. Electron. Mater.* 8, 47 (1979).

Jones, D.L., Le Comber, P.G. and Spear, W.E., *Philos. Mag.*, 36, 541 (1977).

Kittel, C., *Introduction to Solid State Physics*, 3 ed. 1968.

Knights, J.C., *J. Non-Cryst. Solids*, 35&36, 159 (1980).

Knights, J.C., and Lucovsky, G., *CRC Crit. Rev. Solid State Mater. Sci.* 9, 211 (1980).

Konagai, M., *Mater. Res. Soc. Symp. Proc.* 70, 257 (1986).

Kshirsagar, S.T. and Lannin, J.S., *Phys. Rev.* B, 25, 2916 (1982).

Landau, L., *Phys. Z. Sowjetunion*, 3, 664 (1933).

Lannin, J.S., Maley, N., and Kshirsagar, *Solid State Commun.* 53, 939 (1985).

LeComber, P.G., Jones, D.I. and Spear, W.E., *Philos. Mag.*, 35, 1173 (1977).

Lenahan, P.M. and Schubert, W.K., *Phys. Rev.* B, 30, 1544 (1984).

Madan, A., Czubatyj, W., Yang, J., Shur, M.S. and Shaw, M.P., *Appl. Phys. Lett.*, 40, 234 (1982).

Magarino, J., Kaplan, D. and Friederich, A., *Philos. Mag.* B, 45, 285 (1982).

Marshall, J.M., Owen, A.E., *Philos.Mag.* 24, 1281 (1971).

Matsuura, H., Okuno, T., Okushi, H. and Tanaka, K., *J. Appl. Phys.* 55, 1012 (1984).

Miller, W.A. and Olsen, L.C., *IEEE Trans. Elec. Dev.*, ED-31, 654 (1984).

Mishima, Y., Hirose, M. and Osaka, Y., *Jpn. J. Appl. Phys.* 20, 593 (1981).

Mott, N.F., *Philos. Mag.* 22, 7 (1970).

Mott, N.F., *J. Non-Cryst. Solids* 8, 10 (1972).

Mott, N.F. and Davis, E.A., "*Electronic Processes in Non-Crystalline Materials*", Oxford University Press (1979).

Mott, N.F., Davis, E.A., "*Electronic Processesin Non-Crystalline Materials*", C -endon Press, Oxford, p219

(1979).

Movaghar, "*Physics of Disordered Materials*", edited by D. Adler, H. Fritzsche and S.R. Ovshinsky (Plenum, New York), p399-412 (1985).

Murase, K., Amemiya, Y. and Mizushima, Y., JARECT Vol.6, "*Amorphous Semiconductor Technologies & Devices*". Edited by Y. Hamakawa. OHMSHA LTD and North-Holland Publishing Co. (1983).

Nakano, S et al, *19th IEEE Photovoltaic Specialists Conf.*, 678 (1987).

Nagels, P., "*Amorphous Semiconductors*" ed. by M.H. Brodsky, p131 (1979).

Nishikuni, M, et al, *13th International Conf. on Amorphous and Liquid Semiconductors*, Asheville, North Carolina, Aug. 21-25, (1989).

Overhof, H, *Philos. Mag.* B, **44**, 317 (1981).

Phillips, J.C., *Phys. Rev. Lett.*, **42**, 1151 (1979).

Puppin, E., *J. Vac. Sci. Technol.* B 5(2), 606 (1987).

Purnell, J.H. and Walsh, R., *Proc. Roy. Soc. London*, **A293**, 543 (1966).

Rollos, M., *Philos. Mag.* B, **38**, 477 (1978).

Seager, C.H. and Ginley, D.S., *J. Appl. Phys.*, 52(2), 1050 (1981).

Smith, R.A., "*Semiconductors*", Cambrigde University Press (1978).

Spear, W.E. and LeComb, P.G., *Solid, St. Commun.*, 17, 1193 (1975).

Spear, W.E., Le Comber, P.G., Kinmond, S. and Brodsky, M.H., *Appl. Phys. Lett.*, **28**, 105 (1976).

Staebler, D.L. and Wronski, C.R., *Appl. Phys. Lett.*, **31**, 292 (1977).

Street, R.A. and Biegelsen, D.K., *J. Non-Cryst. Solids,* **35&36**, 651 (1980).

Sze, S.M., "*Physics of Semiconductor Devices*" (Wiley, New York), Chapter 2, 4 (1981).

Thomas, P.A. and Flachet, J.C., *Philos. Mag. B*, **51**, 55 (1985).

Tong, B.Y., John, P.K., Wong, S.K. and Chik, K.P., *Appl. Phys. Lett.* **38**, 786 (1981).

Tsai, C.C., Fritzche, H., Tanielian, M.H., Gaczi, P.J., Persans, P.D. and Vesaghi, M.A., *Proc. 7th Intern. Conf. on Amorphous and Liq. Semiconductor*, Edinburgh, ed. by W.E. Spear, Univ. of Edinburgh, p339 (1977).

Tsou, Y.S., Smith, E.B. and Deb, S.K., *Appl. Phys. Lett.*, **51**, 1436 (1987).

Ueda, K., Nakato, Y., Sakai, Y., Matsumura, M. and Tsubomura, H., *J. Appl.Phys.* **64**, 1513 (1988).

Wiles, D.M. and Winklen, C.A., *J. Phys. Chem.*, **61**, 620 (1957).

Willeke, G., Spear, W.E., Jones, D.I. and LeComber, P.G., *Philos. Mag.* B, **46**, 177 (1982).

Wu, X.W. and Tong, B.Y., *3rd International Photovoltaic Science and Engineering Conference*, Tokyo, p305 (1987).

Wu, X.W. and Tong, B.Y., " *Bulletin of the American Phys. Soc.*" **32**, 840 (1987).

Yu, L.S. and Wang, C.D., *IEEE Trans. Elec. Dev.*, **ED-30**, 326 (1983).

Zhang, P.X., Wu, X.W., Yao, J., Wong, S.K., John, P.K. and Tong, B.Y., *Phys. Rev.* B, **36**, 9168 (1987).

Zimmer, S.J., Bube, R.H., Knights, J.C., *J. Appl. Phys.*, **51**, 3278 (1980).